

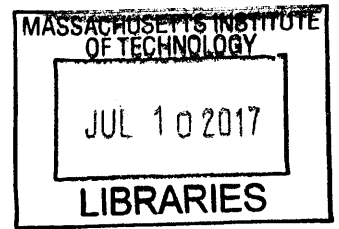
**Biomechanics of the cerebrum at finite strain: a
tissue and cell level study**

by

Thibault Philippe Prévost

S.M., Materials Science and Engineering
Massachusetts Institute of Technology, 2006

Ingénieur de l'Ecole Polytechnique
Ecole Polytechnique, 2004



ARCHIVES

Submitted to the Department of Materials Science and Engineering
in partial fulfillment of the requirements for the degree of

Doctor of Philosophy

at the

MASSACHUSETTS INSTITUTE OF TECHNOLOGY

September 2010

© 2010 Massachusetts Institute of Technology
All rights reserved

Signature of Author **Signature redacted**
Department of Materials Science and Engineering
11 August 2010

Certified by **Signature redacted**
Simona Socrate
Principal Research Scientist

Certified by **Signature redacted**
Thesis Supervisor
Subra Suresh
Vannevar Bush Professor of Engineering

Accepted by **Signature redacted**
Thesis Supervisor
Christopher Schuh
Chair, Departmental Committee on Graduate Students

Biomechanics of the cerebrum at finite strain: a tissue and cell level study

by

Thibault Philippe Prévost

Submitted to the Department of Materials Science and Engineering
on 11 August 2010, in partial fulfillment of the
requirements for the degree of
Doctor of Philosophy

Abstract

The present study addresses the large strain nonlinear mechanical response of the cerebral cortex at the macroscopic tissue level and at the microscopic cell level. Unconfined uniaxial compression tests were conducted *in vitro* on cortical samples of porcine brains. The tests consisted of load-unload and relaxation segments to 50% nominal deformation at 0.01 to 10 s⁻¹ strain rates. The tissue exhibited moderate volumetric compressibility, marked hysteretic features, and substantial nonlinearities. Indentation tests – with displacement histories mirroring those imposed in compression – were performed on the cortex of porcine brains *in vivo*, *in situ* and *in vitro*, in order to assess and contrast the mechanical properties of the live and dead tissue. The tissue response shared similar qualitative nonlinear viscoelastic features under all testing conditions, although, quantitatively, the response was found to be significantly stiffer *in situ* than *in vivo*. Test protocols were also developed at the neuronal cell level using atomic force microscopy. The response of individual somata to cyclic load-unload and relaxation test sequences was found to be nonlinear with time dependencies and hysteretic patterns similar to those measured at the tissue level. A large strain kinematics nonlinear continuum model was proposed to capture the features of the tissue and cell responses. The model was numerically implemented into a three-dimensional finite-element framework. The continuum formulation was found to successfully account for the main experimental observations gathered *in vitro* at the tissue and cell levels.

The present study provides novel insights into the tissue rheology *in vivo*, *in situ* and *in vitro*, at large strains, in the quasi-static and dynamic strain rate regime and reports the first body of observations on the large strain nonlinear viscoelastic properties of brain tissue *in vivo*. These observations could be directly compared to those pertaining to the tissue response *in situ* and *in vitro*, thereby providing a unique quantitative basis for further refinements of existing biomechanical models relying only on *in vitro/situ* measurements. The consistent set of mechanical data collected, and the constitutive

framework proposed at the tissue and cell levels might support the development of multiscale numerical models to study traumatic brain injury.

Thesis Supervisor: Simona Socrate
Title: Principal Research Scientist

Thesis Supervisor: Subra Suresh
Title: Vannevar Bush Professor of Engineering

Contents

Acknowledgments	7
1 Constitutive response of brain tissue <i>in vitro</i>	8
1.1 Overview	8
1.2 Preliminary remarks	9
1.3 Experiments	10
1.3.1 Literature review	10
1.3.2 Test protocol – unconfined uniaxial compression <i>in vitro</i>	12
1.3.3 Results	16
1.4 Constitutive model	20
1.4.1 Literature review	20
1.4.2 Constitutive laws	22
1.4.3 Model fit	29
1.4.4 Model predictions	30
1.5 Discussion	32
1.6 Conclusions	37
2 Brain tissue dynamics <i>in vivo</i>, <i>in situ</i> and <i>in vitro</i>	38
2.1 Overview	38
2.2 Rationale and background	39
2.3 Materials and Methods	41

2.3.1	Test apparatus	41
2.3.2	Surgical procedures	43
2.3.3	Indentation tests	45
2.3.4	Tissue contact – tapping protocol	46
2.4	Results	48
2.4.1	Preliminary observations – effect of <i>dura mater</i> on cortical tissue response	48
2.4.2	Tissue recovery after indentation	49
2.4.3	Test repeatability and rate order indifference	50
2.4.4	Location dependence	51
2.4.5	Post-mortem time differences	54
2.4.6	Representative response <i>in vivo</i>	54
2.4.7	Comparison with literature data	54
2.4.8	Properties <i>in vivo</i> compared to properties <i>in situ</i>	57
2.4.9	Properties <i>in situ</i> compared to properties <i>in vitro</i>	58
2.4.10	Nonlinear rate dependencies	58
2.4.11	Conditioning effects	58
2.5	Discussion and conclusions	61
3	Large strain behavior of single cortical neurons	65
3.1	Overview	65
3.2	Background	66
3.3	Materials and methods	69
3.3.1	Cell Culture	69
3.3.2	Atomic Force Microscopy	70
3.3.3	Modeling: Finite Element Simulations	74
3.4	Results	80
3.5	Discussion	83

4	Concluding remarks	86
A	Brain tissue response: notes on numerical implementation of constitutive model	88
B	Brain tissue response: determination of material parameters	93
B.1	Preliminary parameter estimate	93
B.2	Automated Parameter Search Algorithm	94
B.3	Parameter estimates for “outlying” cases	96
C	Summary of results obtained on hemorrhaged animals	99
C.1	Effect of <i>dura mater</i> on tissue response	99
C.2	Properties <i>in vivo</i> compared to properties <i>in situ</i>	99
C.3	Properties <i>in vivo</i> , <i>in situ</i> and <i>in vitro</i> compared between the hemorrhaged and non hemorrhaged cases	102
D	Preliminary assessment of tissue volumetric compliance in indentation <i>in vitro</i>	105
	Bibliography	109

Acknowledgments

My deepest gratitude goes to Dr. Simona Socrate – a great heart and a great mind – without whom my research experience at MIT would have lacked much of its substance. I am also truly indebted to Professor Subra Suresh, whose support was critical to the successful completion of this work.

Special thanks to Dr. Hasan Alam, Dr. Marc de Moya and Dr. Guang Jin from the Massachusetts General Hospital who made the *in vivo* tests possible. I am especially grateful to Dr. Guang Jin for his patience and his support during the many hours of testing spent at the hospital.

I would also like to extend my gratitude to Dr. Asha Balakrishnan for contributing greatly to the early stages of this project, and to Kristin Bernick for conducting the tests *in vitro* on single neuronal cells.

My warmest thanks go finally to Peter Morley from the MIT Machine Shop, whose help in the design of the mechanical apparatus was essential.

This work was supported by the US Army Research Office and Joint Improvised Explosive Devices Defeat Organization, under contract number W911NF-07-1-0035; the MIT Institute for Soldier Nanotechnologies, under contract number W911NF-07-D-0004; École Nationale des Ponts et Chaussées (Université Paris-Est, France); the Computational Systems Biology Programme of the Singapore-MIT Alliance; and the Interdisciplinary Research Group on Infectious Diseases at the Singapore-MIT Alliance for Research and Technology; and by the US Army Medical Research Material Command GRANTT00521959 (to HBA).

Chapter 1

Constitutive response of brain tissue *in vitro*

1.1 Overview

The dynamic behavior of porcine brain tissue, obtained from a series of *in vitro* observations and experiments, is analyzed and described here with the aid of a large-strain, nonlinear, viscoelastic constitutive model. Mixed gray and white matter samples excised from the superior cortex were tested in unconfined uniaxial compression within 15 h *post mortem*. The test sequence consisted of three successive load–unload segments at strain rates of 1 s^{-1} , 0.1 s^{-1} and 0.01 s^{-1} followed by stress relaxation ($N = 25$). The volumetric compliance of the tissue was assessed for a subset of specimens ($N = 7$) using video extensometry techniques. The tissue response exhibited moderate compressibility, substantial nonlinearity, hysteresis, conditioning and rate dependence. A large-strain kinematics nonlinear viscoelastic model was developed to account for the essential features of the tissue response over the entire deformation history. The corresponding material parameters were obtained by fitting the model to the measured conditioned response (axial and volumetric) via a numerical optimization scheme. The model successfully captures the observed complexities of the material response in loading, unloading, and relaxation

over the entire range of strain rates. The accuracy of the model was further verified by comparing model predictions with the tissue response in unconfined compression at higher strain rate (10 s^{-1}) and with literature data in uniaxial tension. The proposed constitutive framework was also found to be adequate to model the loading response of brain tissue in uniaxial compression over a wider range of strain rates (0.01 s^{-1} to 3000 s^{-1}), thereby providing a valuable tool for simulations of dynamic transients (impact, blast/shock wave propagation) leading to traumatic brain injury.

1.2 Preliminary remarks

The study of the mechanical properties of brain matter – at the tissue–continuum level – has been the focus of numerous investigations in the past four decades (see *e.g.* Refs [1-7]). Many investigators have concentrated their effort on characterizing the coupled time and strain/stress dependencies inherent in the response of the tissue to externally applied mechanical transients – *e.g.* frontal or lateral impact of the head by rigid mass [8-10], linear or angular acceleration pulses applied to the skull [11, 12], indentation of the cortex surface [13]. Understanding how these loading/kinematic conditions applied to the organ boundary translate into local stress–strain states within the tissue continuum is challenging because the brain is, from a biomechanical perspective, a highly complex organ housing multiple “substructures” – *e.g.* brainstem, cerebellum, thalamus, cerebral cortex, corpus callosum – associated with somewhat distinct mechanical properties [14-16]. Most biomechanical studies have been conducted *in vitro* although a few measurements have also been reported *in vivo* [17-21]. The results of different studies are at times difficult to reconcile due to the wide range of variation in experimental protocols, including the species/age of the subjects (human, porcine, bovine, murine), loading configurations (compression, shear, tension, indentation), loading histories (cyclic, stress relaxation, creep), and testing regimes (small/large strains or low/high strain rates). The collected data have facilitated the development of a large variety of constitutive models,

some of which have been shown to account for essential features of the tissue response [22-24] under selected testing conditions. Nonetheless, the integration of all the characteristic features of the large strain tissue response – hysteretic behavior, rate-dependence, nonlinearities, shear and volumetric behavior – into one single constitutive framework has not been achieved thus far.

This study is a component of a multidisciplinary effort aimed at elucidating some key effects of primary blast on the central nervous system [25], and represents a first step towards the development of a predictive model for the response of brain tissue over an extensive range of strains and strain rates. A parallel effort is underway to assess differences between tissue properties in the *in-vivo* and *in-vitro* conditions, where the proposed constitutive formulation is employed to analyze results of indentation tests performed with a dynamic custom tool [26]. The first part of this chapter describes the experimental component of the study (test protocols and main results gathered on porcine cortical samples) while the second part addresses the modeling effort (constitutive laws, numerical implementation, model validation and predictions). Both are preceded by a brief literature review. Some of the limitations inherent in the current model formulation are discussed in the last section, guiding the effort for future model refinements. This work constitutes a preliminary step in the development of a comprehensive experimental data base and enhanced computational tools to be employed in support of a variety of clinical applications, as well as to elucidate mechanically mediated pathways leading to traumatic brain injury.

1.3 Experiments

1.3.1 Literature review

Mechanical tests on brain samples have been conducted mainly in the linear regime via small oscillatory deformations imposed on the tissue, in pure shear or in torsion, over a wide spectrum of frequencies [27-30]. In assessing the time/frequency dependence of the

linear viscoelastic properties of the tissue (*i.e.* storage and loss moduli), these studies have uncovered some important aspects of the tissue dynamics. The thrust of the results reported, nonetheless, suffer from a few limitations. First, most of the data so gathered lack consistency in that the magnitude of the measured scalar moduli varied at times by more than 10-fold in relative terms from one study to another [31]. This lack of consistency may be attributed to multiple factors including: inter-species/intra-species variations (*e.g.* animal breed, age, sex, inherent biological variability); differences in (1) post mortem testing time, (2) tissue storage and hydration conditions, (3) tissue preparation/excision methods, (4) specimen neuroanatomical orientation, (5) temperature conditions, (6) interfacial testing conditions (degree of tissue friction/adherence/slipping on testing fixtures), (7) pre-conditioning effects prior to actual testing. Further, the scope of these investigations is limited *per se* to small deformations as the tissue has been shown to deviate from linearity at strains greater than 1% [32, 33]. More recently, the nonlinear features of the tissue response have been partly characterized in compression [34, 35], tension [36], and shear [23, 37]. While some of these studies measured the tissue response over more than two orders of strain rate magnitude, they were mostly focused on a limited set of test histories (*e.g.* single load-ramp and stress relaxation tests or sinusoidal load-unload cyclic tests at low to medium strains), excluding any direct assessment of the tissue volumetric behavior. Some attempts have been made to retrieve quantitative information on the tissue volumetric compliance [38, 39] but these attempts remain scarce and limited in scope, most investigators relying on incompressibility assumptions or speculative arguments [34, 40, 41]. The experimental part of this doctoral work carried out *in vitro* aims to address some of the limitations noted in previous investigations via the systematic collection of experimental data on porcine cortical specimens in unconfined uniaxial compression comprising the following measurements: (1) nonlinear strain and strain-rate dependencies in load and unload over three orders of strain rate magnitude ($0.01\text{-}1\text{ s}^{-1}$), in the large deformation regime (up to 50% nominal strain), (2) long-term time dependencies in relaxation, (3) lateral tissue deformation to assess volumetric com-

pliance. A porcine model was preferred to other animal models because its gyrencephalic brain – architecturally close to the human brain – has been proven to share with the latter some similarities in terms of pre- and postnatal cerebral development relative to tissue growth, myelination and composition [42-46]. Swine models constitute, moreover, an affordable alternative to more costly, ethically sensitive primate models.

1.3.2 Test protocol – unconfined uniaxial compression *in vitro*

Specimen preparation

Sixteen 6- to 18-month-old¹ swine brains (female, Yorkshire breed) were obtained from a local vendor (Research 87 Inc., Boylston, Massachusetts), following a protocol approved by the Committee on Animal Care at the Massachusetts Institute of Technology. The brains were sectioned along the mid-sagittal plane and transferred on ice to the laboratory within three hours post mortem. Each hemisphere was rinsed upon delivery in phosphate-buffered saline (PBS, 10 mM phosphate buffer) and kept refrigerated in solution to limit tissue degradation. Shortly before testing, mixed gray and white matter samples were excised from the superior cortical region (frontal and parietal lobes²) and maintained hydrated in PBS during all subsequent steps. Preliminary investigations of the optimal sample size for uniaxial compression tests [48] showed that large samples – lying in the cubic centimeter range – yielded the most consistent results. All the data collected for this study were therefore obtained from samples that were, approximately, 25.4 mm x 25.4 mm in cross section and 9 mm in thickness (Figure 1-1A). The mechanical properties obtained shall be viewed as “homogenized” properties of the superior cortex (gray and white matter combined) although the samples tested were composed predominantly of

¹Pigs having reached at least six months of age may be considered cerebrally mature [42], and were therefore selected to minimize age-related variability. Neonatal pigs have been shown to have significantly softer brains [31].

²No notable differences were observed in mechanical properties between the two cortical regions. This observation complements findings previously reported by Coats and Margulies [47] on local cortical gray matter homogeneities at the subcentimetric/millimetric tissue level.

gray matter – accounting typically for $\sim 70\%$ of the sample mass. The experimental protocols were primarily designed so as to reduce the sources of experimental variability arising from tissue handling – which are many, given the delicate nature of the brain parenchyma. Separating intermingled gray and white matters of the superior cortex was found ill-suited for this study because the separation/cutting process implied further alterations of the tissue virgin state (via shearing or stretching) which were deemed too costly relative to the potential benefits.

Axial and lateral measurements

The samples ($N = 25$ from $n = 16$ Yorkshire sows) were tested in unconfined uniaxial compression on commercial testing machines equipped with 20 N load cells – ElectroForce 3200, Bose Corporation, Minnesota, USA ($N = 11$); Zwick Z2.5/TS1S, Ulm, Germany ($N = 14$). Prior to testing, the platens were humidified with PBS to minimize friction at the tissue-platen interface. All tests were conducted at room temperature ($T = 21^\circ\text{C}$) within 15 h *post mortem*.³ A preload of 0.02 N (corresponding to a compressive stress of ~ 30 Pa) was imposed on each sample prior to testing in order to accurately determine the sample thickness. Each sample was subjected to a sequence of three loading segments, at 1 s^{-1} , 0.1 s^{-1} and 0.01 s^{-1} nominal strain rates respectively – each comprising five load-unload cycles to 50% nominal strain – followed by a ramp-relaxation segment to 50% nominal strain held for 300 seconds with a ramp rate of 1 s^{-1} . Figure 1-1 illustrates the imposed strain history (Figure 1-1C) and the resulting stress history (Figure 1-1D) for one representative tissue specimen. The transverse displacements were captured by a Qimaging Retiga 1300 CCD camera equipped with a 200 mm f/4 Nikon lens (Figure 1-1B). Lateral stretch measurements were deemed sufficiently accurate only for a subset of specimens ($N = 7$) because most samples had somewhat irregular edges. Axial data

³Samples were tested between 4 and 15 hours post mortem. No significant variations in tissue response were noted in relation to post mortem test time differences. The responses measured were also found comparable to those reported by Tamura et al. [35] who conducted similar tests within a shorter time frame post mortem (see results section thereafter).

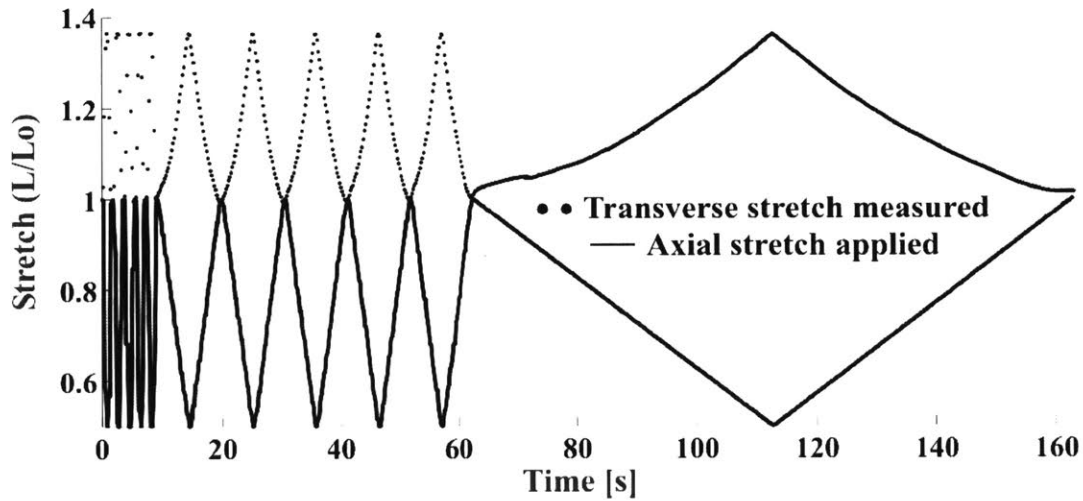
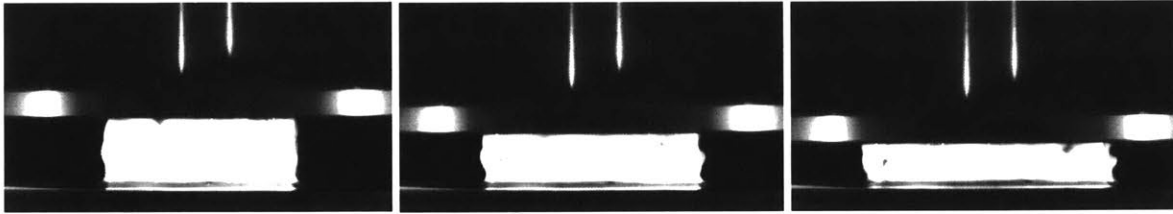


Figure 1-2: Images of the tissue sample at increasing levels of axial deformation. The lateral stretch measurements are obtained by visual extensometry.

(force and displacement) and lateral deformation images were acquired synchronously via software Vic-Snap (Version 3.0D, Correlated Solutions, Inc). The lateral stretches were subsequently assessed using a MATLAB image-analysis custom routine. The processed data are shown for one representative specimen in Figure 1-2. Note that the nominal axial strain values reported in Figures 1-1 and 1-2 were based on the platens' axial displacement history. In practice, most of the specimens did not entirely recover their initial configuration upon unloading: as the platens traveled back to their initial position at the beginning of each loading cycle, the degree of adhesion between the platens and the specimens was often insufficient to enforce complete recovery of the original specimen

height. Full contact was re-established at the end of each load-unload cycle (with a rise in the recorded load), and was lost at the end of the unloading ramps (as the load became negative, tracking the weak tensile adhesive forces between the top surface of the specimens and the platen).

1.3.3 Results

Stress-strain diagrams have been extracted from the representative data in Figure 1-1 for the three load-unload segments (at 1 s^{-1} , 0.1 s^{-1} and 0.01 s^{-1}) and are plotted in Figure 1-3 together with the subsequent relaxation response. As shown in Figure 1-3, the tissue behavior in unconfined compression was intrinsically nonlinear at finite deformation – both in the strain and strain rate domains. The tissue response exhibited marked hysteretic features over the range of strain rates considered for this study. Another notable feature was the substantial degree of “conditioning” associated with the first loading ramp, *i.e.* the dramatic increase in tissue compliance between the initial loading cycle and the subsequent cycles. Differences associated with softening effects between sequential (“conditioned”) cycles at the same loading rate were much less dramatic. Conditioning effects reflected changes in tissue “state” occurring during the first cycle of loading through which the tissue might lose part of its interstitial fluid and/or undergo “irrecoverable” microstructural reorganization/reconfiguration (damage). To ascertain if conditioning was associated with a permanent change in tissue properties, a study was performed on a subset ($N = 6$) of tissue samples which were submitted to two series of five load-unload cycles (uniaxial compression to 50% nominal strain at 1 s^{-1}) separated by a two-hour recovery period in PBS. To a large extent, the re-hydrated samples recovered their original response, with conditioning patterns highly similar to those measured on the virgin tissue, as illustrated in Figure 1-4 for one representative tissue sample. This observation substantiates the hypothesis that interstitial fluid diffusion plays a crucial role in the conditioning process, and that the tissue does not undergo substantial permanent damage in the first loading cycle. The essential features of the tissue response to the

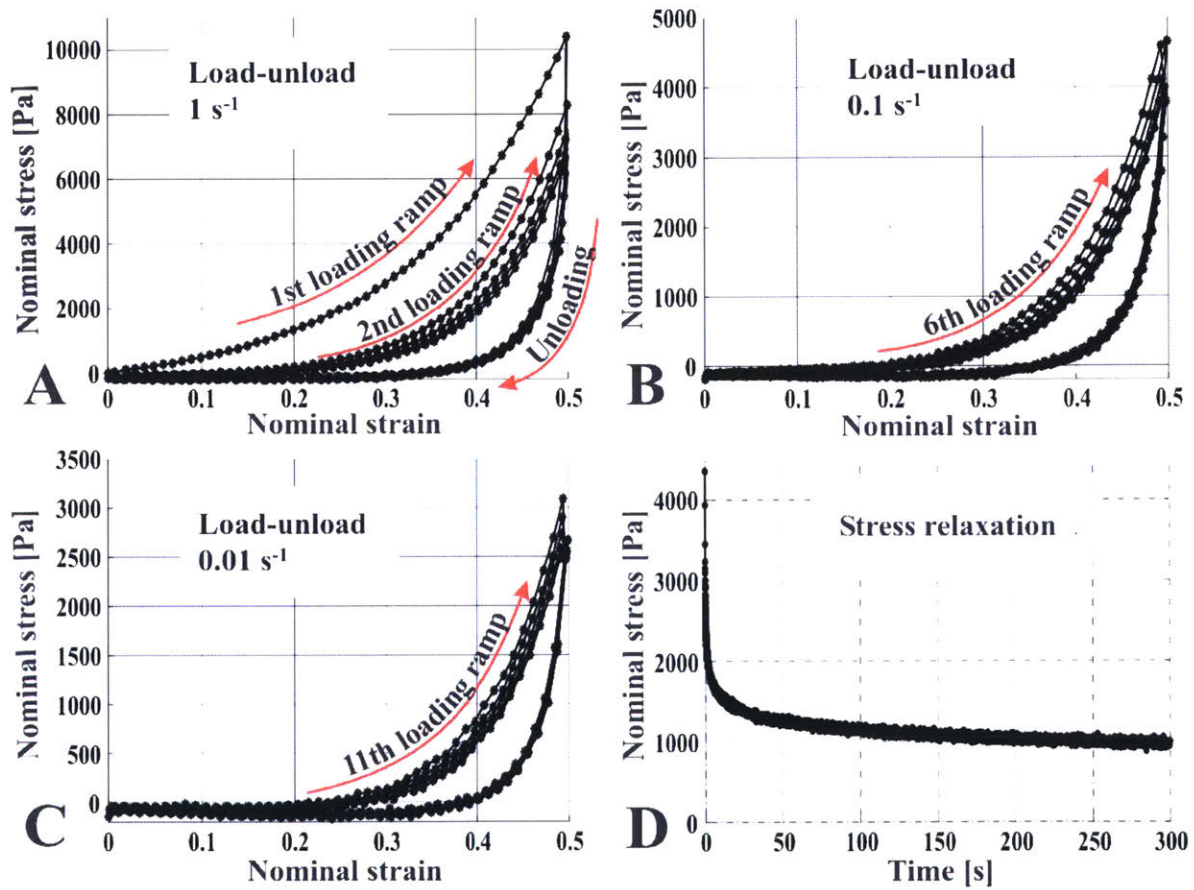


Figure 1-3: Representative cortical tissue response in unconfined compression. Data in panels A, B, C, D are obtained sequentially on the same tissue sample (see corresponding strain/stress-time histories for this representative sample in Figures 1-1C/1-1D).

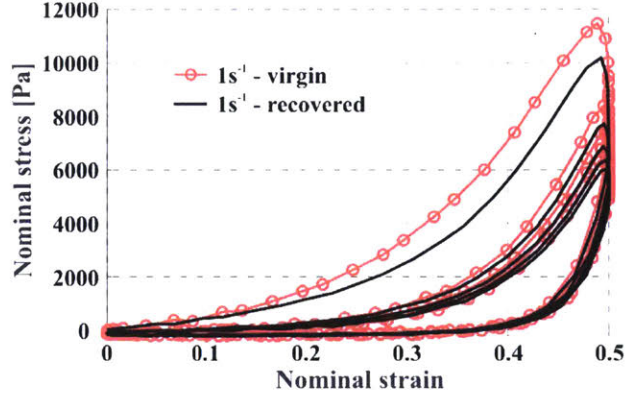


Figure 1-4: Representative cortical tissue response in unconfined compression. The sample was submitted to two series of five load-unload cycles at 1 s^{-1} strain rate separated by a two-hour recovery phase in PBS.

uniaxial compression loading protocol in Figure 1-1 were found to be consistent for all tested samples. The average response and standard deviation are shown in Figures 1-5A and 1-5B (nominal axial stress) and in Figure 1-5D (transverse stretch). For clarity purposes, the stress-strain plots only display the first (virgin) loading ramp at 1 s^{-1} , the subsequent (conditioned) loading ramp at 1 s^{-1} and the first (conditioned) loading ramps at 0.1 s^{-1} and 0.01 s^{-1} . The tissue response exhibited substantial volumetric compliance, with an average 12% volume reduction at an axial stretch of 0.5: $\frac{\Delta V}{V_0} = -12\% [\pm 5.5]$, ($N = 7$ samples, $n = 7 \times 6$ volumetric measurements taken from the sequences of load-unload cycles at 0.1 s^{-1} [X5] and 0.01 s^{-1} [X1] strain rates). Data previously published by Tamura et al. [35] for similar mixed gray/white matter samples from swine cortices are also shown in Figure 1-5A. The (virgin) loading response measured in the Tamura study for a strain rate of 1 s^{-1} was found to be in good agreement with the results of the current study. Miller and Chinzei [34] also investigated the quasi-static response of similar tissue samples for the same animal model. The response of virgin specimens measured by Miller and Chinzei at a strain rate of $0.64 \times 10^{-2} \text{ s}^{-1}$ is gathered in Figure 1-5C and it was found to be significantly stiffer than the average (conditioned) response measured at a comparable strain rate (10^{-2} s^{-1}) in the present study. An exploratory

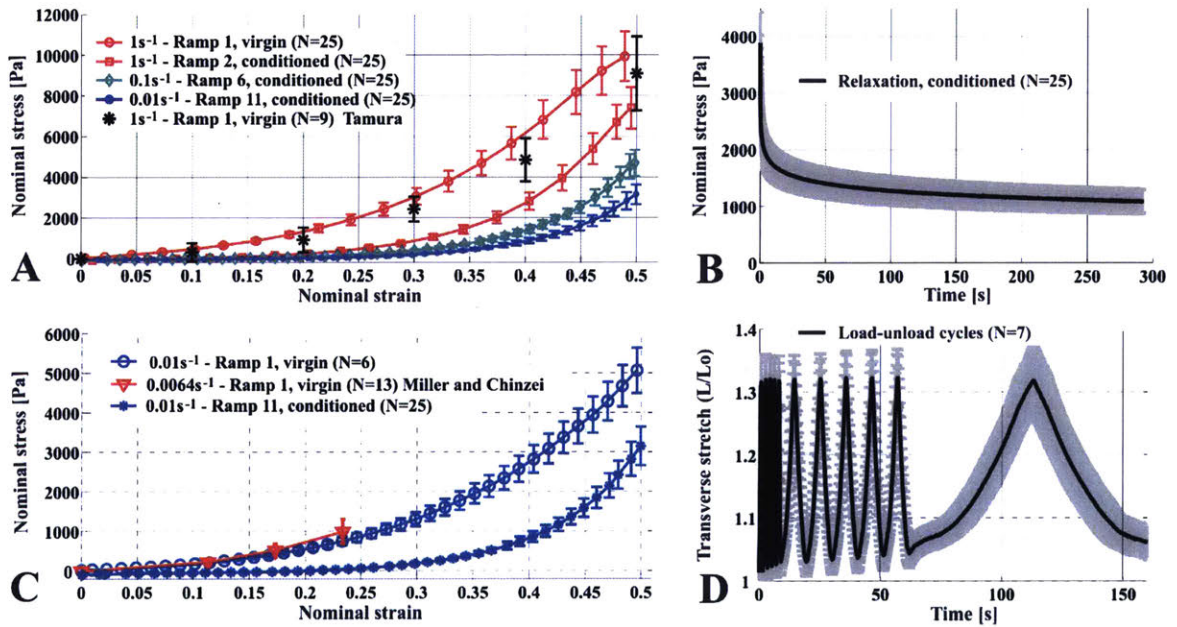


Figure 1-5: Average tissue response and standard deviations. (A) Loading ramps at 1 s^{-1} , 0.1 s^{-1} and 0.01 s^{-1} . (B) Relaxation. (C) Conditioning effects for the loading ramps at 0.01 s^{-1} . (D) Transverse stretch history for the load-unload cycles.

set of measurements was performed to confirm that this discrepancy might be primarily attributed to conditioning effects. Virgin tissue samples ($N = 6$) were subjected to five load-unload cycles at a strain rate of 10^{-2} s^{-1} . The corresponding average first (virgin) loading response, shown in Figure 1-5C, was found to be comparable to that reported by Miller and Chinzei.

1.4 Constitutive model

1.4.1 Literature review

Whether the brain should be considered – for continuum modeling purposes – as a single-phase viscous solid or as a dual-phase fluid-saturated solid is still the subject of differing viewpoints. The traditional dual phase approach follows the theory of consolidation (poroelasticity) originally formalized by Biot in the context of soil mechanics [49]. Although interstitial fluid diffusion and related transport mechanisms have long been recognized to play a crucial role in brain function [50], the poroelastic approach has received only marginal attention in the brain tissue biomechanics community [22, 51]. In the single phase approach, dissipation mechanisms and time dependencies in the tissue response are addressed in the framework of viscoelasticity. Most of the models following this approach are adaptations or combinations of three model subcategories: (1) linear viscoelastic models, based on cyclic loading, in which the tissue response is described by a set of two parameters, the storage and loss moduli [13, 28-30]; (2) small strain formulations for rheological models based on linear or nonlinear spring–dashpot combinations [52, 53]; (3) large strain kinematics quasilinear or nonlinear viscoelastic models for which the tissue response is decomposed into a hyperelastic component – Neo-hookean, Mooney–Rivlin or Ogden formulations are most common – and a dissipative component – *e.g.* multi-mode Prony series [5, 22-24, 54-56]. The linear and quasilinear models – mostly relevant in the small strain regime – are unable to fully capture the complexities of the tissue response at finite strains. In contrast, some of the large strain kinematics models –

integrating nonlinearities within their formulation – have been able to successfully reproduce some specific features of the tissue deformation over fairly complex loading histories. Hrapko et al. [23] employed a multi-mode Mooney–Rivlin viscoelastic network in parallel with a nonlinear hyperelastic resistance to capture the simple shear response of white matter in load, unload and relaxation at strain rates of 1 s^{-1} to 1.5 s^{-1} up to 50% strain, using 16 material parameters. More recently, El Sayed et al. [24] developed a nonlinear elastic viscoplastic formulation to capture some of the hysteretic and dissipative characteristics of the tissue response in uniaxial tension and compression up to 50% nominal strain. The generalized framework proposed by El Sayed et al., in which an arbitrary number of viscoelastic networks are considered in parallel with a viscoplastic network, allowed the authors to fit a number of experimental findings with different configurations and numbers of constitutive elements. In most instances, the phenomenological models proposed in the literature rely on a fairly large number of material parameters validated over a limited range of loading regimes/histories.

The nonlinear visco-hyperelastic model developed here is also phenomenological in nature; it espouses the modeling “philosophy” pursued by previous investigators; and it idealizes the tissue as a single, homogeneous, isotropic phase. The proposed formulation combines the following advantages within a single framework: (1) it accounts for all the observed complexities inherent in the tissue response at low-to-medium strains and strain rates (*i.e.* nonlinearities, hysteresis, time-dependencies, volumetric behavior), (2) it is accurate and predictive over an extended range of strains and strain rates while requiring a relatively small number of material parameters, and (3) it relies on physically motivated arguments, where different constitutive elements of the model, and their corresponding parameters, can be conceptually associated with specific underlying mechanisms of deformation. This empirical interpretation of modeling elements provides some guidance in the fitting process, as discussed in Appendix B.

1.4.2 Constitutive laws

A schematic (rheological) representation of the proposed model for the tissue response is shown in Figure 1-6 with the corresponding 3D large kinematics deformation map. For the most part the notation used hereafter is that prevailing in modern continuum mechanics:

\mathbf{F}_*	deformation gradient
$\mathbf{V}_* \equiv (\mathbf{F}_* \cdot \mathbf{F}_*^T)^{1/2}$	left stretch tensor from polar decomposition of \mathbf{F}_*
$V^0(V)$	tissue volume at time 0 (time t)
$V_1^0 = f_1 V^0$	incompressible tissue volume fraction at time 0
$V_2^0 = f_2 V^0 = V^0 - V_1^0$	compressible tissue volume fraction at time 0
$J \equiv \det(\mathbf{F}) = \frac{V}{V^0}$	volumetric macroscopic jacobian
$J_2 = \frac{V_2}{V_2^0}$	volumetric jacobian for compressible tissue fraction
$\bar{\mathbf{B}}_* = J^{-2/3} \mathbf{F}_* \cdot \mathbf{F}_*^T$	isochoric component of left Cauchy-Green strain tensor
$\mathbf{E}_* = \ln(\mathbf{V}_*) = \ln((\mathbf{F}_* \cdot \mathbf{F}_*^T)^{1/2})$	Hencky strain tensor
$\mathbf{L}_* = \dot{\mathbf{F}}_* \cdot \mathbf{F}_*^{-1}$	velocity gradient
$\mathbf{D}_* = \text{sym}(\mathbf{L}_*) = \frac{1}{2}(\mathbf{L}_* + \mathbf{L}_*^T)$	stretching tensor
$\mathbf{W}_* = \text{skw}(\mathbf{L}_*) = \frac{1}{2}(\mathbf{L}_* - \mathbf{L}_*^T)$	spin tensor
\mathbf{T}_A	Cauchy stress
$\mathbf{T}_h = \frac{1}{3} \text{tr}(\mathbf{T}_A) \mathbf{1}$	hydrostatic component of Cauchy stress
$\mathbf{T}_d = \mathbf{T}_A - \frac{1}{3} \text{tr}(\mathbf{T}_A) \mathbf{1}$	deviatoric component of Cauchy stress
$\mathbf{T}'_* = \mathbf{T}_* - \frac{1}{3} \text{tr}(\mathbf{T}_*) \mathbf{1}$	stress deviator
$\mathbf{N}_* = \frac{\mathbf{T}_*}{\sqrt{\text{tr}(\mathbf{T}_*^2)}}$	unit tensor in the direction of stress

The model comprises an elastic network (A) representing the instantaneous response of the tissue and a viscoelastic network (elements (B), (C), (D) and (E)) incorporating the dissipative contributions. Following Lee's decomposition [57], the total deformation gradient, \mathbf{F} , applied to the tissue may be decomposed as:

$$\mathbf{F} = \mathbf{F}_A \cdot \mathbf{F}_B$$

where \mathbf{F}_A and \mathbf{F}_B represent, respectively, the elastic (instantaneous) and viscoelastic components of the tissue deformation. The viscous flow is assumed to be isochoric, hence the total volumetric Jacobian J may be expressed as: $J \equiv \det(\mathbf{F}) = \det(\mathbf{F}_A) \cdot \det(\mathbf{F}_B) = \det(\mathbf{F}_A)$. The viscoelastic response of the tissue is captured by the combination of a nonlinear short-term viscous element (B) and a linear viscoelastic backstress network (CDE). With regard to the backstress network, the viscoelastic deformation gradient \mathbf{F}_B is further decomposed as:

$$\mathbf{F}_B = \mathbf{F}_C \cdot \mathbf{F}_D$$

where the linear viscous element (D) models the long-term relaxation of the backstress contribution. Both \mathbf{F}_C and \mathbf{F}_D are taken to be isochoric.

The total Cauchy stress \mathbf{T}_A in the tissue is decomposed into its hydrostatic and deviatoric components:

$$\mathbf{T}_A = \mathbf{T}_h + \mathbf{T}_d$$

where the hydrostatic component \mathbf{T}_h and the deviatoric \mathbf{T}_d component are physically associated with the deformation mechanisms prevailing in bulk and in shear, i.e. governing the volume-mediated and shear-mediated portions of the tissue response respectively.

Bulk-mediated response

Brain tissue is highly hydrated. Although interstitial fluid diffusion is not explicitly included in the current model, a simplified qualitative understanding of the role of hydrating fluid in determining the apparent volumetric tissue behavior is the foundation of the proposed formulation for the bulk response. Briefly, the undeformed tissue volume, V^0 , is partitioned into an incompressible fraction, $f_1 V^0 = V_1^0$, and a compressible fraction, $f_2 V^0 = V_2^0$, where $f_1 + f_2 = 1$. The corresponding components of the deformed tissue volume, V , are V_1 and V_2 . This partition mirrors a separation of the hydrating fluid in

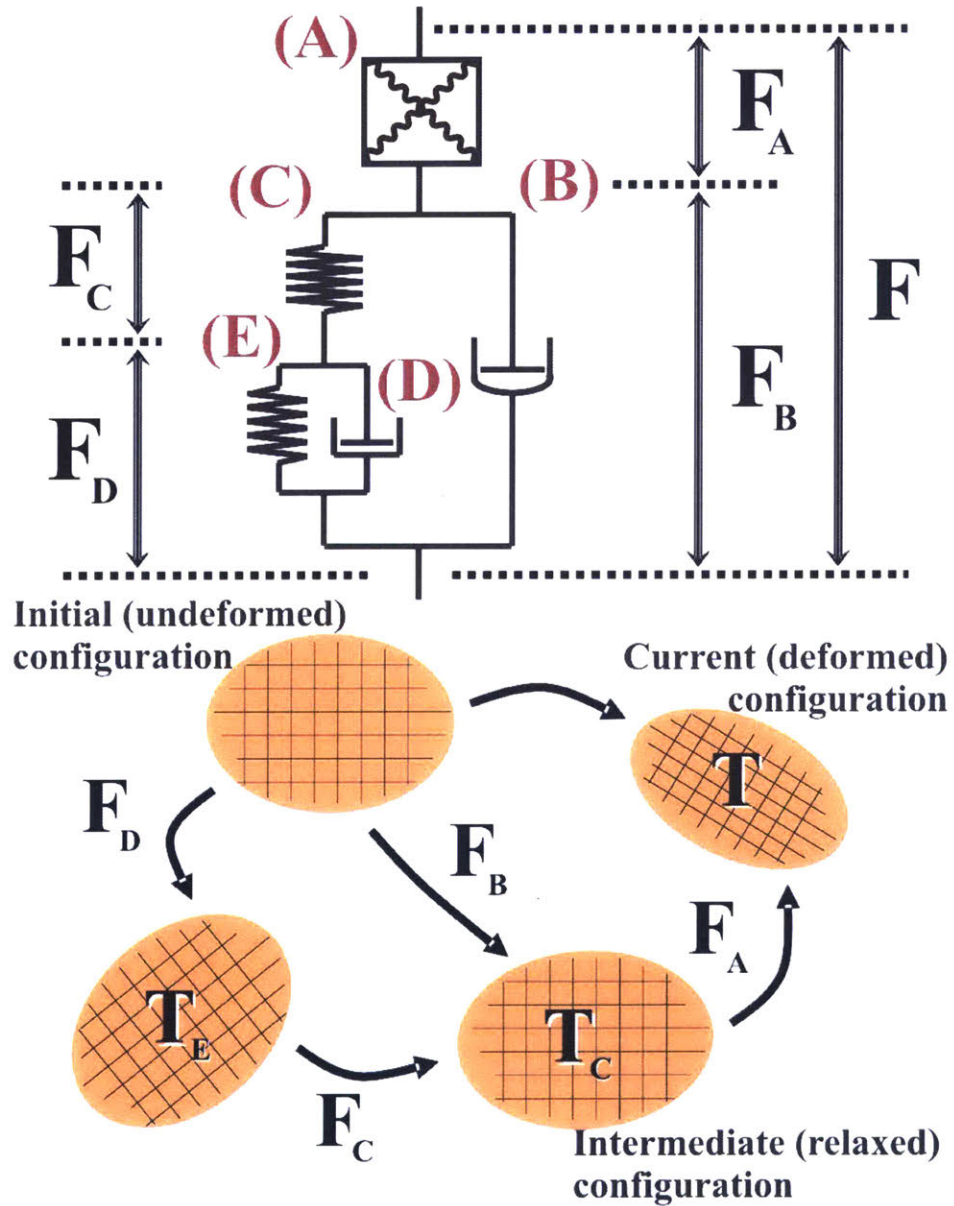


Figure 1-6: Schematic of rheological model (top) and corresponding large kinematics deformation map (bottom).

a “bound” component, which does not diffuse freely under loading, and an “interstitial” component, which diffuses in response to hydrostatic loading, accommodating volumetric tissue deformation. The incompressible fraction of the volume, V_1 , is conserved, so that the corresponding volumetric Jacobian $J_1 = \frac{V_1}{V_1^0}$ remains constant ($J_1 \equiv 1$) throughout the deformation history. The hydrostatic stress \mathbf{T}_h developed in the tissue is then assumed to be driven by the volumetric Jacobian of the compressible fraction, $J_2 = \frac{V_2}{V_2^0}$ as:

$$\mathbf{T}_h = K \cdot \ln(J_2) \cdot \mathbf{1}$$

where the hydrostatic stress is characterized by a logarithmic dependence on the volumetric Jacobian, and K is the small-strain bulk modulus of the compressible fraction. As a consequence of the incompressibility constraint enforced for V_1 , the macroscopic tissue volumetric Jacobian $J = \frac{V}{V^0}$ can be expressed as:

$$J = f_1 + (1 - f_1)J_2$$

so that the hydrostatic stress may be restated in terms of the total volumetric Jacobian J :

$$\mathbf{T}_h = K \cdot \ln\left(\frac{J - f_1}{1 - f_1}\right) \cdot \mathbf{1}$$

Estimates of typical hydration levels for brain tissue indicate that fluid accounts for approximately 80% of the brain mass [58]. Although the incompressible tissue fraction is effectively a material property, a fixed value $f_1 \approx 0.8$ is selected for the proposed model. This latter assumption is based on the notion that interstitial cerebrospinal fluid, which is free to diffuse throughout the tissue, only accounts for a small portion of the total water content. Phenomenologically, the proposed constitutive framework captures the highly nonlinear resistance to volumetric deformation exhibited by the brain parenchyma. Also, note that in setting the incompressible fraction to 80% the current formulation

implicitly assumes that the volumetric response of the tissue becomes infinitely stiff as the volumetric Jacobian approaches 0.8.

Shear-mediated response

The deviatoric component of the stress response, \mathbf{T}_d , is adapted from the freely-jointed 8-chain model developed for macromolecular elastic networks [59]:

$$\mathbf{T}_d = \frac{\mu_0}{J} \cdot \frac{\lambda_L}{\lambda} \cdot \mathcal{L}^{-1} \left(\frac{\lambda}{\lambda_L} \right) \cdot (\bar{\mathbf{B}}_A - \lambda^2 \mathbf{1}),$$

where

$$J \equiv \det(\mathbf{F}) = \det(\mathbf{F}_A)$$

$$\bar{\mathbf{B}}_A = J^{-2/3} \mathbf{F}_A \cdot \mathbf{F}_A^T$$

$$\lambda^2 = \frac{1}{3} \text{tr}(\bar{\mathbf{B}}_A)$$

$$\mathcal{L}(\beta) = \coth(\beta) - \frac{1}{\beta}$$

and μ_0 and λ_L are model parameters which scale with the initial shear modulus and the limiting extensibility (locking stretch) of the network. \mathcal{L} denotes the Langevin function. The 8-chain model, originally developed for elastomeric materials, is based on statistical mechanics arguments. It assumes a weakly bonded network of randomly oriented chains for which the source of resistance to deformation, *i.e.* the change in Helmholtz free energy, is mainly governed by changes in configurational entropy of the reorienting chains. The adaptation of this model to brain tissue is motivated by the following considerations.

- The cortex is primarily composed of cells (neurons and glia) whose main constitutive elements are actin filaments, neurofilaments and microtubules [58]; these latter components may be viewed – in a highly simplified representation at the mesoscale

level – as a loose “assembly” of randomly oriented “chains” sharing some similarities with the idealized statistical mechanics network envisioned for the 8-chain model.

- Preliminary force-displacement measurements performed on individual actin filaments [60] suggest that the use of Langevin statistics may be suitable to account for the non-linear force-extension curves of these structural components.
- The tissue response – as measured experimentally – exhibits nonlinearities which are well captured by the inverse Langevin function. Further, some empirical evidence collected at the cell level [61] suggests that single neurons share similar nonlinear characteristics.

The time-dependent portion of the tissue deformation is defined via the evolution of the velocity gradient, \mathbf{L} , imposed on the tissue:

$$\mathbf{L} = \dot{\mathbf{F}} \cdot \mathbf{F}^{-1} = \dot{\mathbf{F}}_A \cdot \mathbf{F}_A^{-1} + \mathbf{F}_A \cdot \dot{\mathbf{F}}_B \cdot \mathbf{F}_B^{-1} \cdot \mathbf{F}_A^{-1} = \dot{\mathbf{F}}_A \cdot \mathbf{F}_A^{-1} + \mathbf{F}_A \cdot \mathbf{L}_B \cdot \mathbf{F}_A^{-1} = \mathbf{L}_A + \tilde{\mathbf{L}}_B$$

where $\mathbf{L}_B = \dot{\mathbf{F}}_B \cdot \mathbf{F}_B^{-1}$ denotes the viscoelastic velocity gradient in the relaxed (unloaded) configuration and $\tilde{\mathbf{L}}_B = \mathbf{F}_A \cdot \mathbf{L}_B \cdot \mathbf{F}_A^{-1}$ may be interpreted as the “push-forward velocity gradient”, *i.e.* the velocity gradient convected to the current (loaded) configuration (see kinematic map provided in Figure 1-6 and chapter 2 of Holzapfel [62] for more details on push-forward tensor operations). The velocity gradient $\tilde{\mathbf{L}}_B$ may be further decomposed into its symmetric and skew-symmetric parts, $\tilde{\mathbf{L}}_B = \tilde{\mathbf{D}}_B + \tilde{\mathbf{W}}_B$, where $\tilde{\mathbf{D}}_B$ and $\tilde{\mathbf{W}}_B$ denote the rate of viscous stretch and the viscous spin respectively. Following [63], the unloaded (relaxed) configuration may be made unique by specifying $\tilde{\mathbf{W}}_B \equiv 0$, and thus the evolution of the viscoelastic component of the deformation gradient, \mathbf{F}_B , reduces to: $\dot{\mathbf{F}}_B = \mathbf{F}_A^{-1} \cdot \tilde{\mathbf{D}}_B \cdot \mathbf{F}$. The viscous stretching tensor $\tilde{\mathbf{D}}_B$ is constitutively prescribed to follow the direction of the deviator \mathbf{T}'_B of the driving stress \mathbf{T}_B according to a nonlinear reptation-based scaling law, adapted from [64]:

$$\begin{aligned}\tilde{\mathbf{D}}_{\text{B}} &= \dot{\gamma}_{\text{B}} \cdot \mathbf{N}_{\text{B}} = \dot{\gamma}_{\text{B}} \cdot \frac{\mathbf{T}'_{\text{B}}}{\sqrt{\text{tr}(\mathbf{T}'_{\text{B}})}} = \dot{\gamma}_0 \cdot f_{\text{R}} \cdot \left(\frac{\sqrt{\mathbf{T}'_{\text{B}} : \mathbf{T}'_{\text{B}}}}{\sqrt{2}\sigma_0} \right)^n \cdot \frac{\mathbf{T}'_{\text{B}}}{\sqrt{\text{tr}(\mathbf{T}'_{\text{B}})}}; \\ f_{\text{R}} &= \frac{\alpha^2}{\left(\alpha + \sqrt{\text{tr}(\mathbf{F}_{\text{B}} \cdot \mathbf{F}_{\text{B}}^{\text{T}})} / 3 - 1 \right)^2}\end{aligned}$$

where $\dot{\gamma}_0$ is a dimensional scaling constant ($\dot{\gamma}_0 = 10^{-4} \text{ s}^{-1}$). The reptation factor, f_{R} , accounts for the increasing resistance to viscous flow observed in macromolecular networks for increasing levels of accumulated viscous deformation. The factor α is a small constant introduced to eliminate the singularity at $\mathbf{F}_{\text{B}} = 1$ [64], and is set to $\alpha = 0.005$. The rate sensitivity exponent, n , and the strength parameter, σ_0 , are material properties.

The driving stress \mathbf{T}_{B} for the (short-term) nonlinear viscous element (B) is obtained as the difference between the Cauchy stress in the tissue, \mathbf{T}_{A} , and the backstress from the linear viscoelastic network (CDE) convected to the current configuration:

$$\mathbf{T}_{\text{B}} = \mathbf{T}_{\text{A}} - \mathbf{T}_{\text{C}} = \mathbf{T}_{\text{A}} - \frac{1}{J} \cdot \mathbf{F}_{\text{A}} \cdot \mathbf{S}_{\text{C}} \cdot \mathbf{F}_{\text{A}}^{\text{T}}$$

The 2nd Piola-Kirchhoff stress, \mathbf{S}_{C} , in the elastic element (C) of the backstress network is taken to scale linearly with the Hencky strain⁴ of the corresponding deformation gradient \mathbf{F}_{C} :

$$\mathbf{S}_{\text{C}} = 2G_0 \mathbf{E}_{\text{C}} = 2G_0 \ln(\mathbf{V}_{\text{C}}) = 2G_0 \ln \left[\left(\mathbf{F}_{\text{C}} \cdot \mathbf{F}_{\text{C}}^{\text{T}} \right)^{1/2} \right]$$

where \mathbf{E}_{C} is deviatoric, due to the isochoric nature of \mathbf{F}_{C} [66], and G_0 is a material parameter representing the short-term shear modulus of the viscoelastic backstress network.

A parallel constitutive framework is followed to evaluate the driving stress for the

⁴For a discussion on the adequacy of the Hencky strain measure at finite strains, the reader is referred to [65].

long-term linear viscous element (D), as the difference between the stress \mathbf{S}_C in the elastic element (C) and the long-term backstress \mathbf{S}_E in the elastic element (E):

$$\mathbf{S}_D = \mathbf{S}_C - \mathbf{F}_C \cdot \mathbf{S}_E \cdot \mathbf{F}_C^T$$

where

$$\mathbf{S}_E = 2G_\infty \mathbf{E}_D = 2G_\infty \ln(\mathbf{V}_D) = 2G_\infty \ln \left[\left(\mathbf{F}_D \cdot \mathbf{F}_D^T \right)^{1/2} \right]$$

and G_∞ is a material parameter related to the long-term (equilibrium) shear response of the viscoelastic backstress network. The flow-driven deformation mechanisms unfolding in the tissue at long times are controlled via the linear viscous element (D). The corresponding velocity gradient $\tilde{\mathbf{L}}_D$ in the elastically unloaded configuration is constitutively prescribed by setting $\tilde{\mathbf{W}}_D \equiv 0$, and obtaining the stretching tensor, $\tilde{\mathbf{D}}_D = \mathbf{F}_C \cdot \dot{\mathbf{F}}_D \cdot \mathbf{F}_B^{-1}$, as

$$\tilde{\mathbf{D}}_D = \frac{1}{\sqrt{2}\eta} \cdot \mathbf{S}_D$$

where the viscosity η is a material parameter.

In summary, the proposed large strain kinematics model comprises eight material parameters: K , μ_0 , λ_L , n , σ_0 , G_0 , G_∞ , η . Values of these parameters appropriate to capture the (conditioned) response of brain tissue are determined in the following sections by fitting the proposed model to the measured response in unconfined compression.

1.4.3 Model fit

The constitutive model was implemented as a Fortran user-defined material subroutine in ABAQUS/Standard (Simulia, Providence, RI). Time-integration of the constitutive model is accomplished through an explicit scheme where the viscous stretching tensors are taken to be constant over each time increment. The model was fit to the conditioned tissue response using the representative set of axial data – *i.e.* axial data lying about the

average – as reported in Figures 1-1 and 1-3 along with the average lateral data shown in Figure 1-5D. The fit was initiated using the Nelder-Mead simplex method [67, 68] and subsequently optimized manually. The optimized material parameters were found to be: $K = 800 \text{ Pa}$, $\mu_0 = 20 \text{ Pa}$, $\lambda_L = 1.09$, $n = 3$, $\sigma_0 = 25 \text{ Pa}$, $G_0 = 4,500 \text{ Pa}$, $G_\infty = 600 \text{ Pa}$, $\eta = 600,000 \text{ Pa}\cdot\text{s}$. For a discussion on the material parameter determination and the automated search algorithm, the reader is referred to Appendix B. The optimized simulation results are summarized in Figure 1-7. The proposed material formulation successfully captures the main features of the tissue response – volumetric compliance, hysteresis, long-time relaxation behavior and nonlinear strain/strain-rate dependencies spanning three orders of strain rate magnitude. Note that the load-unload response at different strain rates and the relaxation response were experimentally obtained (and numerically simulated) over a single sequential loading history. Some discrepancies in material response were encountered between model and experiment in the low strain rate, low strain regime (Figures 1-7C and 1-7D). These differences stemmed mainly from the fact that perfect adhesion was assumed in the numerical model between sample and upper platen at all times whereas, experimentally, contact between the sample and platen was lost at low strains, low rates in the final/initial portion of the unloading/reloading segments. Some artifacts could have been added to the simulation procedure in order to account for these loss of contact effects. However, given the high compliance of the tissue at low strains and low rates, the simpler “perfect adhesion” assumption was deemed sufficient for the purpose of this study.

1.4.4 Model predictions

To further assess the applicability/relevance of the proposed formulation, the predictions of the proposed model were compared with two sets of data collected respectively by Miller and Chinzei [36] in uniaxial tension at quasistatic strain rates⁵ and by the authors

⁵Testing conditions and animal model used in the Miller and Chinzei study are nearly identical to the protocols followed in this study, allowing a direct comparison.

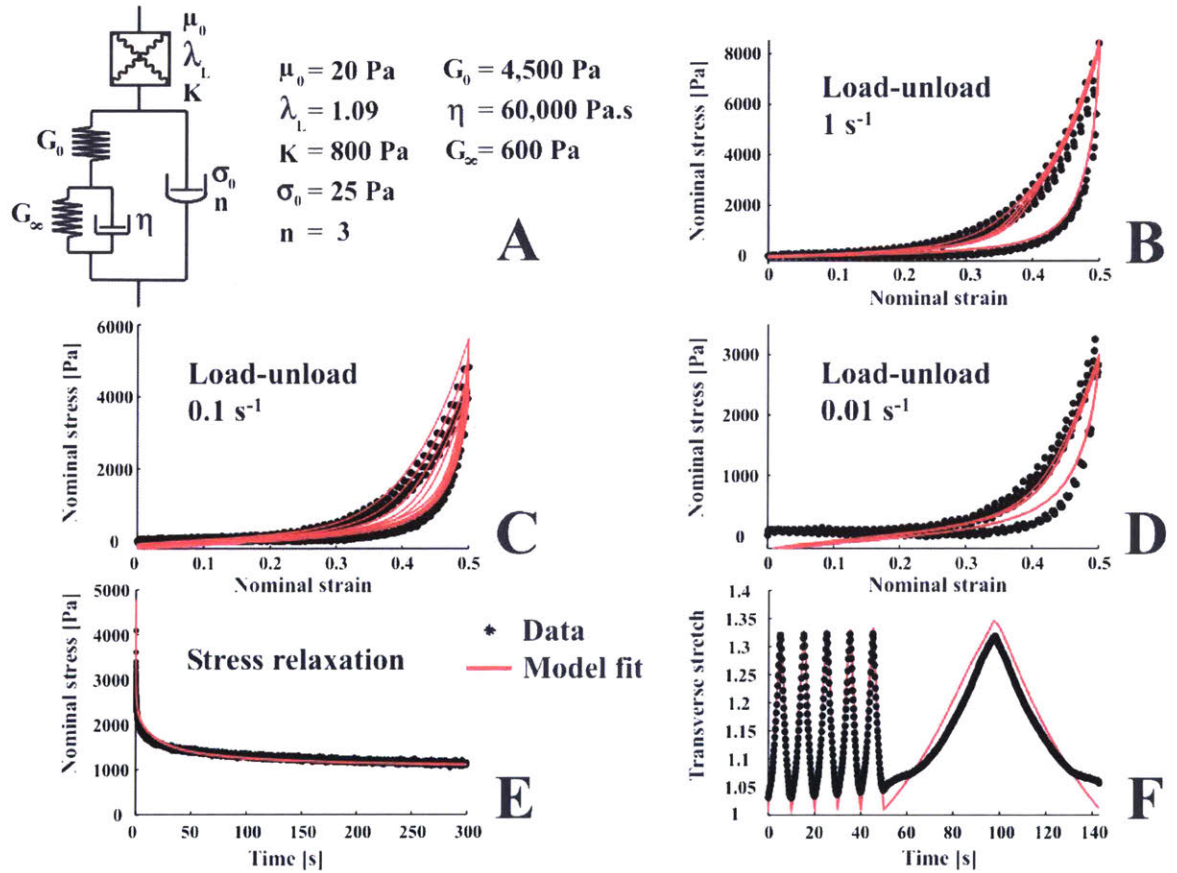


Figure 1-7: Model fit to representative data set in unconfined uniaxial compression. (A) Optimized material parameters. (B), (C), (D) and (E) Axial tissue response (measured and simulated) over entire loading history. (F) Associated lateral deformation (measured and simulated) over the five load-unload cycles at 0.1 s^{-1} strain rate and the first cycle at 0.01 s^{-1} strain rate. Weighted mean-squared error between simulated and measured responses (see appendix for details) was found to be $3.5 \cdot 10^{-3}$.

in unconfined uniaxial compression at 10 s^{-1} strain rate⁶. The results are reported in Figure 1-8. The loading and unloading response predicted by the model in uniaxial compression at 10 s^{-1} strain rate is in good agreement with the experimental data. The responses predicted by the model in tension at low and medium strain rates are also in good agreement with those reported by Miller and Chinzei in the low-to-medium strain range. At larger strains however, the tissue response predicted by the model stiffened, as reported previously for other similar biological tissues [69, 70], while the response measured by Miller and Chinzei softened. It may be postulated that the softening behavior observed by Miller and Chinzei at large tensile strains reflected the unfolding of failure mechanisms – which, given the delicate nature of brain tissue, are likely to occur within the tissue and/or at the platen interface for high levels of tensile deformation.⁷

1.5 Discussion

The experimental protocols developed in this study enabled the collection of a large, consistent pool of mechanical data gathered *in vitro* on macroscopic brain samples at finite strains (0–50%) in the low-to-medium strain rate regime ($0.01\text{--}1 \text{ s}^{-1}$). Of particular interest are some quantitative features of the tissue response – *e.g.* volumetric compliance, large strain viscoelastic behavior upon unloading and reloading, combined nonlinearities in the strain and strain rate domains – which were not available from previous studies but which are highly relevant to guide the development of accurate rheological models. In particular, the experimental measurement of the unloading portion of the tissue response proved crucial in the identification of the relative contributions of elastic and viscoelastic mechanisms to the overall tissue resistance to deformation. The determination of these contributions in the modeling phase enabled the resulting model to predict tissue behavior

⁶The compression test protocol employed at 10 s^{-1} strain rate followed that detailed in the preceding section for the lower rates of deformation.

⁷Unfortunately the Miller and Chinzei data do not include unloading and reloading segments, which could have provided a more conclusive interpretation of the tissue response.

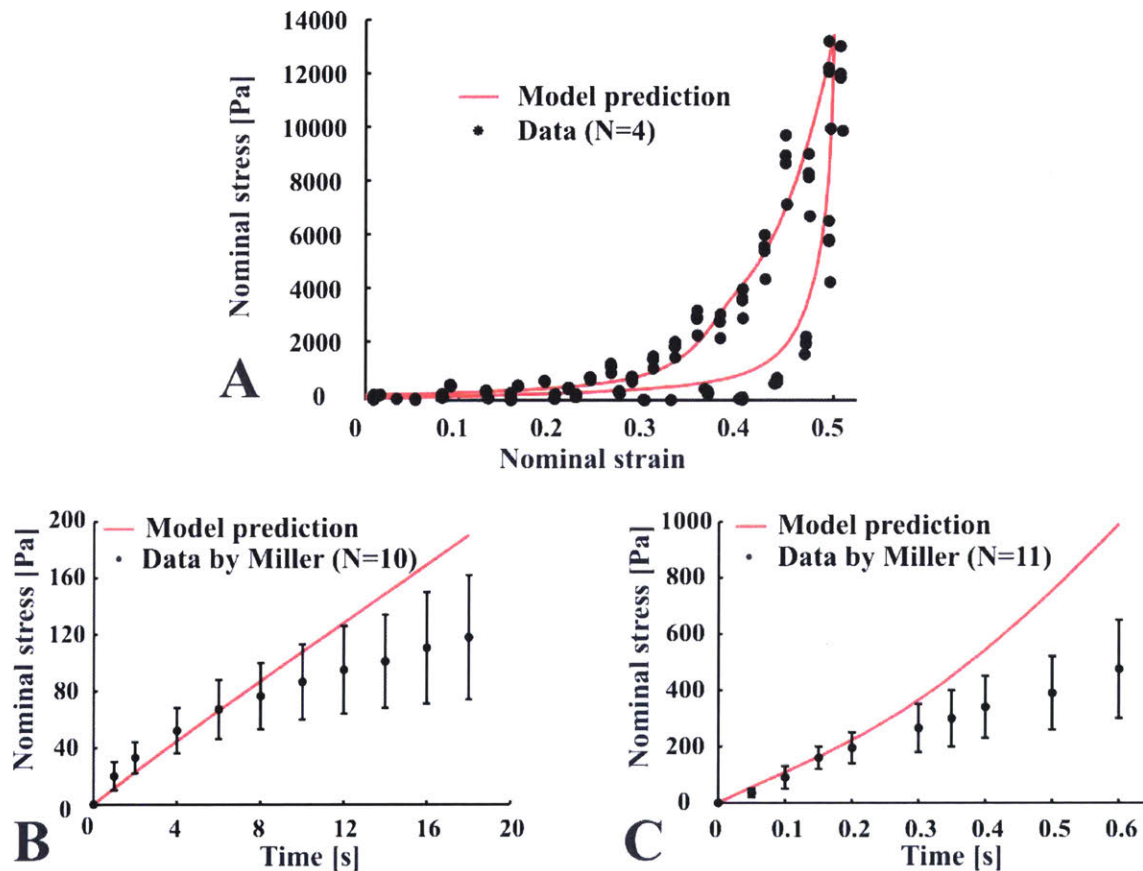


Figure 1-8: Model predictions compared with measured responses in unconfined uniaxial compression (A) and uniaxial tension (B and C). (A) Tissue response measured by the authors in compression to 50% nominal strain at 10 s^{-1} strain rate. (B) Average tissue response measured by Miller and Chinzei [36] in tension on 10 mm high specimens to 15% nominal strain at $5 \text{ mm}\cdot\text{min}^{-1}$ ($\sim 0.0083 \text{ s}^{-1}$ nominal strain rate). (C) Average tissue response measured by Miller and Chinzei [36] in tension on 10 mm high specimens to 50% nominal strain at $500 \text{ mm}\cdot\text{min}^{-1}$ ($\sim 0.83 \text{ s}^{-1}$ nominal strain rate).

at a strain rate (10 s^{-1}) lying outside the original range on which the fit was performed. The current study is only a first step towards the development of a model able to provide accurate predictions for the tissue behavior over arbitrary strain histories. Among the limitations of the study, it could be noted that: (1) the tissue behavior was only characterized in one mode of deformation (unconfined uniaxial compression) over a range of strain rates not exceeding 10 s^{-1} ; (2) lateral stretch measurements could be accurately obtained only in the lower rate regime (0.01 to 0.1 s^{-1}) due to the limited capabilities of the image acquisition system; (3) homogenized measurements may have been affected by partial local discontinuities in the deformation field, as sulci were included,⁸ (4) partial adhesion/decohesion of the specimens from the platens might have affected/alterd the measured tissue response at the end of the unloading ramps; (5) the tissue did not reach full equilibrium at the end of the five minute relaxation period selected for this study, suggesting that relaxation tests where the deformation is held over the course of 20–30 minutes – *i.e.* within a time window for which tissue degradation may still be neglected – are needed to measure equilibrium tissue response. Also note that the conditioned response of the tissue was investigated and characterized according to a decreasing order of deformation rates. Preliminary results (unpublished) seem to indicate that once a sample is deformed at a given rate it is “conditioned” for deformation at that rate and at lower rates but it will still exhibit additional conditioning if tested subsequently at higher rates. Altering the order of the loading segments in future studies may therefore provide useful validation data for a model accounting for conditioning effects.

The proposed constitutive model successfully captures the main features of the large strain tissue response, as measured in uniaxial compression and tension. While the selected set of material parameters was optimized specifically for the conditioned tissue response in the low to medium strain rate regime, the current formulation remains general in nature and might be applied to model tissue response over more extensive ranges

⁸Care was taken to exclude results from any samples showing manifest opening/sliding at the sulci and/or inhomogeneous deformation (as attested by the images collected via the visual extensometer system).

of strain rates.⁹ To demonstrate this versatility, a preliminary fit of the model to the unconditioned (first loading ramp) tissue response measured at low to high rates of deformation (0.01 to 3000 s⁻¹) was conducted. The main results are reported in Figure 1-9.

The set of material parameters found to capture the tissue response upon loading at high rates was: $K = 10$ MPa, $\mu_0 = 10$ kPa, $\lambda_L = 1.03$, $n = 0.3$, $\sigma_0 = 2$ kPa, $G_0 = 6$ kPa, $G_\infty = 2$ kPa, $\eta = 1$ kPa.s. Note that to capture the high-rate regime response the material parameters needed to be altered. This is to be expected as additional mechanisms of resistance to deformation might be operative at these rates. This observation mirrors findings in polymeric materials [71] where additional constitutive elements are required to account for the increased resistance to molecular motions in the high frequency regime. The bulk response of biological materials is also found to be substantially stiffer at high rates of deformation [72] as diffusion of interstitial fluid is drastically reduced. The proposed model, with the modified material parameters reported in Figure 1-9, efficiently captures the essential features of the unconditioned loading response of brain tissue over a range of strain rates from 0.01 to 3000 s⁻¹. While some of the fine details of the tissue response in the very low rate regime are unavoidably lost with this alternative set of parameters, the extensive range of strains and strain rates over which the tissue response is adequately captured highlights the potential value of this model for finite element simulations of loading transients leading to traumatic brain injury. Typical deformation histories of brain tissue under blunt impact or blast loading conditions present a very wide spectrum of strains and strain rates, with inhomogeneous fields characterized by steep spatial and temporal gradients. The availability of an accurate constitutive law to model the brain tissue response is a crucial requirement to assess local levels of strain, stress and strain rate associated with potential injury mechanisms. The proposed model represents a first step towards the attainment of this goal. Further model refinements are needed to address the time-dependence of the volumetric response associated with

⁹The proposed formulation was also found to be appropriate to model the response of rat neurons as measured via Atomic Force Microscope (AFM) indentation [61].

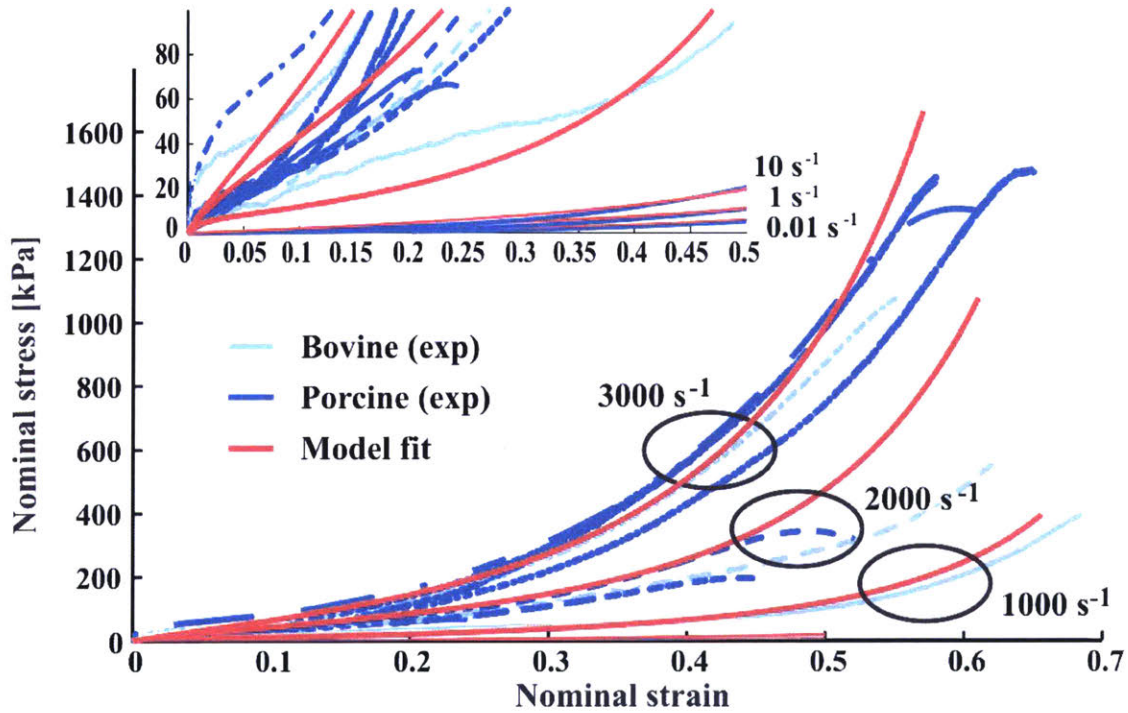


Figure 1-9: Model fit to the tissue response measured upon loading in unconfined uniaxial compression at nominal strain rates spanning six orders of magnitude (0.001 s^{-1} to 3000 s^{-1}). The sets of bovine and porcine data reported at high rates (1000 s^{-1} to 3000 s^{-1}) have been obtained by the Chen group at Purdue University via Kolsky bar measurements [7]; the porcine data shown for the low to medium strain rates (0.001 s^{-1} to 10 s^{-1}) are those collected by the authors. The optimized model parameters for the fit are: $K = 10 \text{ MPa}$, $\mu_0 = 10 \text{ kPa}$, $\lambda_L = 1.03$, $n = 0.3$, $\sigma_0 = 2 \text{ kPa}$, $G_0 = 6 \text{ kPa}$, $G_\infty = 2 \text{ kPa}$, $\eta = 1 \text{ kPa}\cdot\text{s}$. The dimensional factor was set to 1000 s^{-1} , and the reptation factor f_R to 1.

the biphasic nature of the tissue in the high to intermediate strain rate regime.

1.6 Conclusions

This study presents a significant pool of *in vitro* experimental results collected on porcine cortical brain tissue in unconfined compression up to 50% nominal strain over three orders of strain rate magnitude ($0.01-1 \text{ s}^{-1}$) – both in load and unload – with quantitative assessments of the tissue lateral deformation. The constitutive model presented here successfully captures the complex features inherent in the tissue response – hysteresis, nonlinearities, volumetric compliance, short- and long-time behaviors – over four orders of strain rate magnitude ($0.01-10 \text{ s}^{-1}$), up to 50% nominal strain with a relatively low number of material parameters. The model is also able to predict the tissue behavior in tension at quasistatic rates ($\sim 0.83 \cdot 10^{-2} \text{ s}^{-1}$ to 0.83 s^{-1}) up to $\sim 20\%$ strain. Further testing of the model ability to predict the material response under different modes of deformation is a necessary future step. While the results of previous studies on the shear behavior of the tissue are available in the literature [15, 23, 37] variations in experimental protocols (post mortem time, age and species of the animal model, sample size, orientation, composition, tissue conditioning etc) lead to large relative discrepancies. In order to circumvent these difficulties, an experimental investigation of the shear response of comparable tissue samples under testing conditions identical to those of the current study would be needed to assess the ability of the current version of the model to capture the material response in simple shear. Furthermore, an experimental and computational investigation of the tissue response to dynamic indentation is being conducted to better characterize the accuracy of the model for inhomogeneous deformations and complex boundary conditions. Finally, the current formulation does not account for the observed conditioning effects, where the first loading ramp is associated with a substantially stiffer tissue response. Interstitial fluid diffusion may play a significant role in this conditioning process and future model refinements would need to account for these poro-elastic effects.

Chapter 2

Brain tissue dynamics *in vivo*, *in situ* and *in vitro*

2.1 Overview

The mechanical properties of brain tissue have been mostly characterized *in vitro*. Understanding how these properties may differ quantitatively from those encountered *in vivo* is a critical step towards the development of biofidelic brain models. The present study provides novel insights into the tissue rheology *in vivo*, *in situ* and *in vitro*, at large strains, in the quasi-static and dynamic strain rate regime (up to $\sim 10 \text{ s}^{-1}$). The nonlinear dynamic response of the cerebral cortex was measured in indentation (with a 12.65 mm hemispherical indenter, to 6 mm depth) on the exposed frontal and parietal lobes of anesthetized porcine subjects ($n = 5$). Load-unload cycles were applied to the tissue surface at sinusoidal frequencies of 10 Hz, 1 Hz, 0.1 Hz and 0.01 Hz. Ramp-relaxation tests were also conducted to assess the tissue viscoelastic behavior at longer times. After euthanasia was induced, the indentation test sequences were repeated *in situ* on the exposed cortex maintained in its native configuration within the cranium. Mixed gray and white matter samples were subsequently excised from the superior cortex to be subjected to identical indentation test segments *in vitro* within six to seven hours *post mortem*. The

main response features – *e.g.* nonlinearities, rate dependencies, hysteresis, conditioning – were measured and contrasted *in vivo*, *in situ* and *in vitro*. The tissue behavior was found to be significantly stiffer *in situ* than *in vivo*. The consistent, quantitative set of mechanical measurements thereby collected provides a solid, preliminary experimental database to support the development of constitutive models for brain response to be used in simulations of traumatic brain injury.

2.2 Rationale and background

Traumatic brain injury (TBI) is a leading cause of death and morbidity in the developed world [73-78]. Understanding the precise mechanisms through which an external mechanical insult to the head translates into a local pattern of Central Nervous System (CNS) tissue/cell injury is acutely challenging. The challenge is daunting because the intricate combination of events suspected to result in TBI occurs at multiple levels: the macroscopic organ level, mesoscopic tissue level, microscopic cell level and nanoscopic molecular level. The multiplicity of scales mirrors the diversity of the physical processes involved. This diversity spans the traditional fields of science and engineering – from biophysics to medicine, mechanical engineering to biochemistry, computer science to molecular biology. It may be hypothesized that TBI unfolds at the cell level, mainly as a consequence of the stress/strain constraints imposed on the CNS cells. Because the cell is a component of an organized tissue structure lying in a complex multi-organ system, how the loading transients imposed on the brain boundaries translate quantitatively into local traumatic tissue/cell strain-stress maps remains unclear. Quantifying the local mechanical impact of these transients on neural cell “assemblies” at the mesoscopic tissue level in ways that are both biologically relevant and mechanistically predictive substantiates the need for accurate biofidelic brain models to be developed – *i.e.* mechanical models able to capture the complexities of the tissue behavior *in vivo*. While the tissue response has been extensively characterized *in vitro* under various modes of deformation (*e.g.* shear [23, 28,

29, 33, 37], compression [6, 22, 34, 35, 79, 80] and tension [16, 22, 36, 81]), the availability of mechanical data on the living tissues remains limited. Three main experimental techniques have been employed to quantify brain tissue properties *in vivo*: MRI elastography [21, 82-86], surface suction [87] and indentation [17, 19, 20, 88, 89]. The first technique is non-invasive and may provide useful estimates of the tissue viscoelasticity in the linear range at small levels of deformation. It relies, however, on calibration procedures and theoretical assumptions whose pertinence and accuracy are at times difficult to verify. The last two techniques are invasive but may provide direct measurements of tissue compliance. Indentation techniques especially have been widely used to characterize the mechanical response of biological tissues in their native state [13, 90-94]. A few indentation studies have been conducted on the exposed cortex of porcine brains *in vitro* [20, 95], *in situ* [13, 17, 20] and *in vivo* [17, 19, 20, 88, 89]. Gefen and Margulies [20], in particular, led the largest scale *in vivo* study to date by measuring and comparing the relaxation response of one-month old swine cortices *in vivo* and *in situ* via a 2 mm diameter indenter tip actuated to 4 mm depth on the exposed cortical surface at velocities of 1 mm/s and 3 mm/s. The complex features of the living brain large strain response – nonlinearities, hysteresis, rate dependencies – have not been, however, characterized thus far. The present study provides the first extensive set of experimental measurements carried out *in vivo*, *in situ* and *in vitro* on the superior cortex of 3 month-old porcine brains in an effort to assess and contrast the nonlinear dynamic properties of the tissue in its three physical states. The experiments detailed hereafter comprise measurements performed in indentation (cyclic load-unload and relaxation) on the frontal and parietal lobes of living and dead porcine brains with a 12.65 mm hemispherical indenter, to 6 mm depth (~25-50% nominal deformation) over a range of deformation rates spanning four orders of magnitude (0.01-10 Hz frequency or 0.12-120 mm/s velocity). The tests were conducted with a large-range dynamic indenter able to impose (in closed-loop motion control mode) sinusoidal displacements on the cortical surface to a penetration depth of 6 mm over a broad range of speeds.

2.3 Materials and Methods

2.3.1 Test apparatus

The indenting tool assembly consisted of a voice coil linear actuator with a built-in LVDT displacement transducer (H2W Technologies, Valencia, CA) connected to a closed-loop motion control board (Galil Motion Control, Rocklin, CA). The voice coil shaft had an excursion amplitude of 38 mm and could operate in displacement-control mode at velocities up to ~ 120 mm/s (i.e. 10 Hz frequency for sinusoidal displacements of 6 mm). A 20 N load cell (Honeywell, Golden Valley, MN) was affixed to the voice coil shaft head in series with a 12.65 mm diameter hemispherical tip (Figures 2-1B and 2-1C). The voice coil indenting assembly was mounted on a testing frame designed to accommodate large porcine animals in a setting mimicking conditions of an intensive care environment (Figure 2-1A). The frame, characterized by six degrees of freedom in adjustable motion (i.e. 3 degrees in translation and 3 degrees in rotation), enabled the user to accurately position the indenter tip to the desired testing location and to align it normal to the measurement surface, as described elsewhere [48]. Briefly, its T-slotted aluminum structure (MiniTec Framing Systems, Victor, NY) comprised two sets of linear rails allowing for manual positioning adjustments in the horizontal plane along the x and y directions respectively. Motion along the vertical z-axis was controlled via a manual BiSlide with counter (Velmex, Bloomfield, NY) providing 250 mm of adjustable linear motion with $250 \mu\text{m}$ precision. A three-axis rotary stage connecting the portable indenter to the frame was attached to the BiSlide z-axis, providing $\pm 25^\circ$ of tilt from the vertical axis and 360° of rotation (Newport Corporation, Irvine, CA).

Mechanical data sets (indenter force and displacement) were continuously acquired using two parallel acquisition systems: a low rate (10 Hz) acquisition system integrated to the motion controller (Galil Motion Control, Rocklin, CA) and a higher rate (5,000 Hz) acquisition system for laptop-based measurements (DAQCard-6036E, LabVIEW 8.2, National Instruments, Austin, TX).

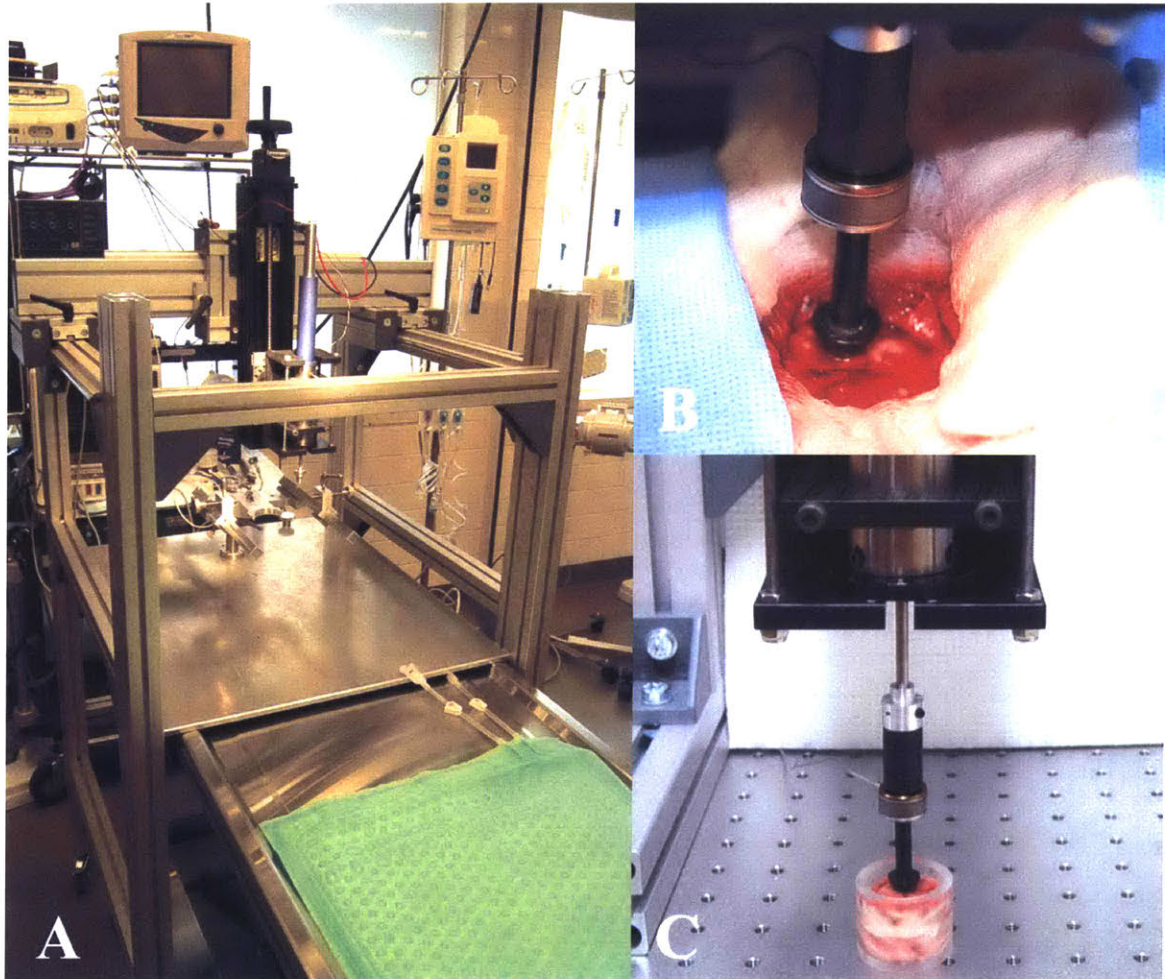


Figure 2-1: Experimental setup. (A) Operating room configuration for the mechanical tests conducted *in vivo* and *in situ*. The stereotactic frame and the testing frame are shown along with the mechanical indenter and the BiSlide positioner. (B) Cranial window *in vivo*. The indenter tip affixed in series with the 20 N load cell is actuated on the exposed cortical lobes. (C) Testing configuration *in vitro*. The mechanical indenter is operated on the confined tissue bilayer excised from the superior part of the frontal and parietal lobes and maintained hydrated in PBS.

2.3.2 Surgical procedures

Five three-month old Yorkshire pigs (42-45 Kg) were used in this study, which comprised two distinct phases: an exploratory test phase on donor hemorrhaged animals ($n = 2$, male) during which the test protocols were developed, optimized and preliminary data were collected; and a full-scale test phase on non-hemorrhaged animals ($n = 3$, female) in which the optimized test protocols were implemented. All procedures were approved by the relevant institutional committees at the Massachusetts General Hospital where the *in vivo* and *in situ* tests were carried out, and at the Massachusetts Institute of Technology where the *in vitro* tests were conducted. The protocols were also approved by the animal care and use committee of the funding agency (US Department of Defense).

The animals were housed in the animal care facility for at least 4 days before experiment and allowed free access to food and water until 12 hours before induction of anesthesia. Anesthesia was induced via intra-muscular injection of 4.4 mg/Kg of Telazol (tiletamine hydrochloride + zolazepam hydrochloride, Fort Dodge Animal Health, Fort Dodge, Iowa). The animals were intubated via an endotracheal tube connected to a ventilator with isoflurane general anesthesia and controlled mechanical ventilation. After intubation, anesthesia was maintained with 1.5-2% isoflurane. Body temperature was maintained using a heating pad pre-set at 37 ± 0.5 °C. Physiological saline solution was administered intravenously at a maintenance infusion rate of 5 mL/Kg/hr throughout the test procedure. Prior to surgery, the head of the pig was secured in a stereotactic frame adapted from previous design developments [96] with skull pegs affixed to the zygoma to prevent movement of the cranium (Figure 2-1). Hemorrhaged animals were fully resuscitated with saline solution (0.9% NaCl: three times the volume of shed blood) to replace the blood loss. The scalp was reflected off the cranium via a midline scalp incision, and craniotomy was performed with a hand-held drill, exposing the superior part of both cortical hemispheres through a cranial window that was approximately 4.5 cm x 4.5 cm in size (Figure 2-2A).

The dura mater was carefully reflected to allow for direct mechanical measurements

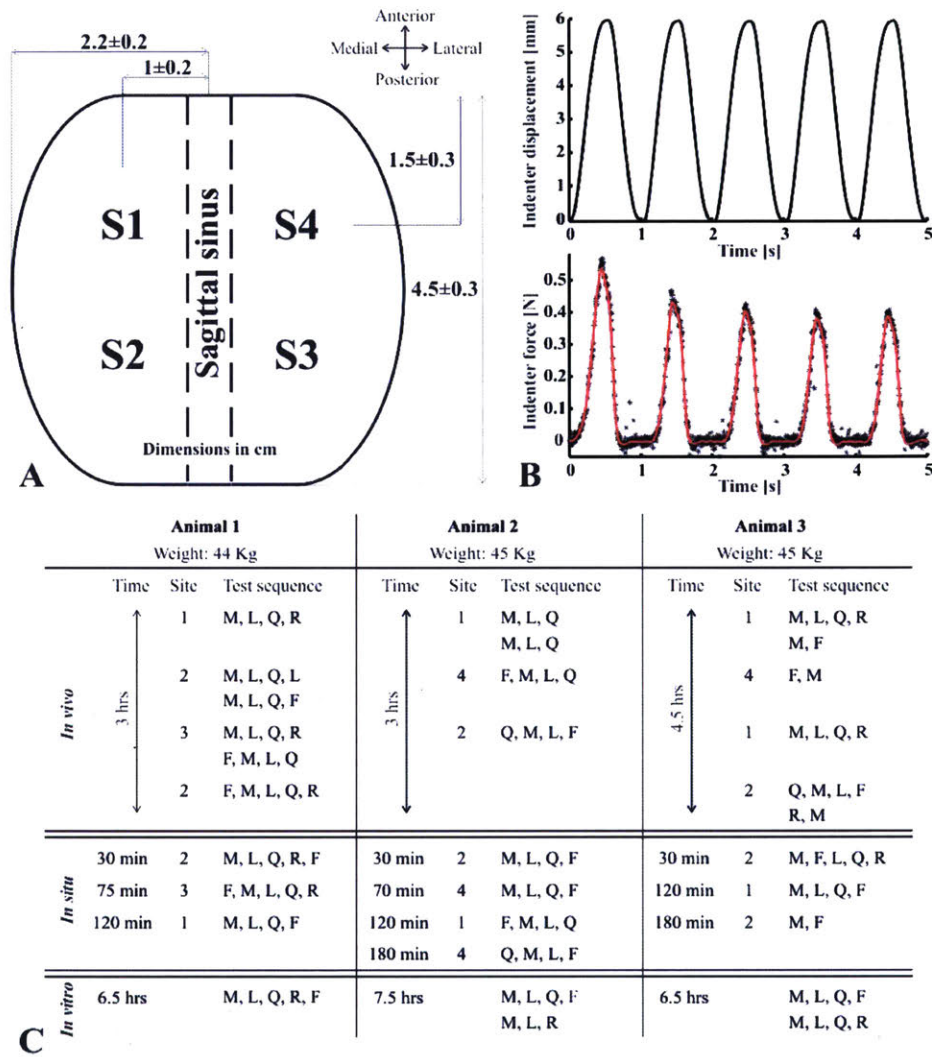


Figure 2-2: Overview of indentation test protocols *in vivo*, *in situ* and *in vitro*. (A) Schematic of cranial window with localization of indentation sites S1, S2, S3, S4. (B) Imposed indenter displacement history and resulting force histories obtained for a representative set of measurements *in vivo* at a sinusoidal frequency of 1 Hz. The raw force profile (black dots) is shown superposed to the processed, smoothed profile (red solid line). (C) Summary of indentation tests conducted *in vivo*, *in situ* and *in vitro* on three non-hemorrhaged animals (3-month old, Yorkshire, female). Cyclic test sequences to 6 mm depth are labeled as “F” (fast / 10 Hz / 120 mm.s⁻¹), “M” (medium / 1 Hz / 12 mm.s⁻¹), “L” (low / 0.1 Hz / 1.2 mm.s⁻¹), and “Q” (quasistatic / 0.01 Hz / 0.12 mm.s⁻¹). 3 min relaxation tests with a ramp rate of 12 mm.s⁻¹ are labeled as “R”. All cyclic tests corresponded to 5 load-unload sinusoidal segments and they were repeated at least twice except for the slowest cyclic tests (Q) which consisted of 2-3 load-unload segments performed only once. Times *in situ* and *in vitro* refer to *post mortem* times.

Parameter	Mean \pm standard deviation
Heart rate (bpm)	101 \pm 16
Respiratory rate (vpm)	10
Arterial pressure (mmHg)	97 \pm 11 (systole) / 43 \pm 7 (diastole)
SpO₂ (%)	97.5 \pm 0.5
Et-CO₂ (mmHg)	45.5 \pm 3
Temperature (°C)	35.3 \pm 0.6

Figure 2-3: Physiological parameters monitored at 5 min intervals during the *in vivo* tests. Average values and standard deviations are provided for the non-hemorrhaged cases ($n = 3$).

on the cortical surface. Physiological/hemodynamic parameters (heart rate, respiratory rate, blood pressure, end-tidal carbon dioxide, hemoglobin saturation level, body temperature) were monitored every five minutes for the entire duration of the test procedure, which lasted about five hours (from sedation to euthanasia). Average values for these physiological parameters are listed in Figure 2-3. After completion of the *in vivo* tests, the subjects were euthanized with an intravenous injection of Ethasol (0.25 mL/Kg).

2.3.3 Indentation tests

The indenter was equipped with a 12.65 mm diameter hemispherical tip. Indentation tests were conducted *in vivo* on the frontal and parietal lobes of both hemispheres at 4 distinct sites located \sim 1.5 cm from the craniotomy edges (Figure 2-2A). Test sequences consisted of 2 to 5 load-unload cycles to 6 mm indentation depth at sinusoidal frequencies of 10, 1, 0.1 or 0.01 Hz corresponding to average displacement rates of 120, 12, 1.2 or 0.12 mm.s⁻¹ respectively (see *e.g.* Figure 2-2B). Tests were also performed to measure the tissue relaxation response, with loading ramps at 12 mm/s to a target indentation depth of 6mm, and holding times of 180 s. The tissue was allowed to recover for two minutes between consecutive sequences of load-unload or relaxation segments. Tests at

a given site at a given frequency/speed were repeated at least twice, except for those corresponding to the slowest (0.01 Hz) load-unload cycles and the relaxation segments that were performed only once. After euthanasia was induced, indentation tests were repeated *in situ* at the same sites 30-180 minutes *post mortem*. The brain was kept in its native configuration within the braincase throughout the *in situ* phase of the tests, and physiological saline solution was regularly added to the exposed surface to minimize tissue dehydration. The brain was subsequently removed from the cranium and transferred on ice to the laboratory for further testing *in vitro*. For the *in vitro* indentation tests, tissue specimens were placed in a 3 cm diameter and 2.8 cm height rigid cylindrical container (Figure 2-1C). The tissue specimens consisted of ~2.5 cm thick tissue bilayers. The specimens were prepared by coring cylindrical samples measuring about 3 cm in diameter and 1.2 cm in height from the surface of the frontal and parietal lobes and layering them so as to bring both inferior faces into contact. This expedient was intended to minimize friction between the tissue specimens and the container, as the inferior surfaces of the cored samples were found to exhibit a higher proportion of (more adherent) white matter. The tissue was hydrated with refrigerated phosphate buffered solution (1X PBS) to minimize friction with the walls of the container and to limit tissue degradation. Load-unload and relaxation sequences – identical to those conducted *in vivo* and *in situ* – were conducted in indentation on the confined tissue bilayer 6 to 7 hours *post mortem*. All tests *in vitro* were performed at room temperature ($T \sim 21^\circ\text{C}$). A summary of the optimized tests conducted *in vivo*, *in situ* and *in vitro* on the three non-hemorrhaged animals is provided in Figure 2-2C.

2.3.4 Tissue contact – tapping protocol

Identifying contact between indenter tip and tissue in a reliable and reproducible manner is of critical importance in indentation tests, especially when using a spherical indenter tip, and when measuring a tissue response that is nonlinear. Visual estimation of contact conditions was found to be imprecise and unreliable due to the presence of cerebrospinal

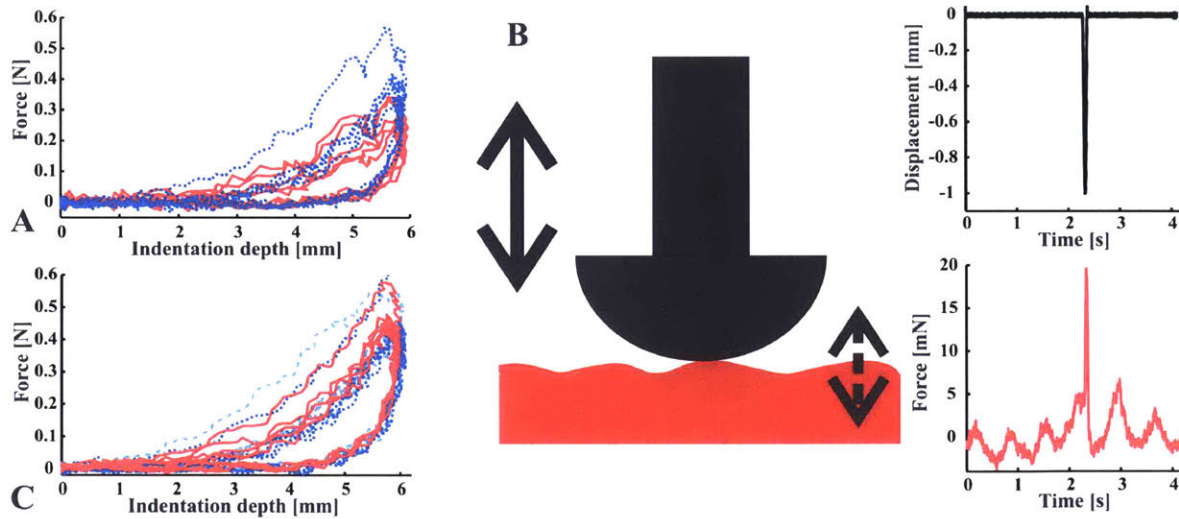


Figure 2-4: Tissue contact/tapping protocol. (A) When contact was determined only by visual inspection, substantial variations in indenter force were observed between successive measurements. (B) Schematic of indenter tip position relative to oscillating tissue surface during contact determination procedure *in vivo* (left). Imposed tip displacement history and resulting force history measured for one representative case satisfying contact condition requirements (right). Note that the periodic force oscillations measured by the contacting tip correspond to the brain surface movements associated with the ~ 100 bpm heart rate. (C) The proposed tapping protocol resulted in reduction in response variability as shown for three successive measurements.

fluid and blood surrounding the indentation sites. The contact determination procedure was further complicated *in vivo* by the brain surface oscillations stemming from respiratory perturbations and rhythmic blood pressure variations. For the initial tests carried out on hemorrhaged animals, contact between indenter tip and tissue was established by visual inspection. With this visual inspection approach, substantial variability in the measured tissue response was noted, as shown for one representative set of measurements in Figure 2-4A. This variability was assumed to arise mainly from uncertainties in the tissue contact determination procedure and therefore a more systematic determination method was developed. The latter consisted in gently “tapping” the tissue surface down to 1 mm depth over a 100 millisecond period. The resulting contact force was measured

and full contact was deemed established when the force differential associated with the 1 mm tapping test reached an amplitude of $\sim 15\text{-}20$ mN (Figure 2-4B). The tapping method was found to drastically reduce the variability in the measured tissue response (Figure 3C) and it was therefore systematically implemented for the subsequent tests conducted on non-hemorrhaged animals *in vivo*, *in situ* and *in vitro*. The vertical z-position of the indenter – as measured through the counter of the vertical BiSlide – was adjusted via the tapping method at the beginning of each indentation sequence. The adjusted position was carefully noted to assess any residual tissue deformation. When tests were performed on a previously indented site, a recovery period of at least two minutes was observed before the tapping procedure.

2.4 Results

All statistical analyses reported hereafter were based on one-way Analysis Of Variance (ANOVA). Results were considered statistically significant for $P < 0.05$.

2.4.1 Preliminary observations – effect of *dura mater* on cortical tissue response

As part of the preliminary test phase involving the hemorrhaged animals, a small number of indentation experiments were carried out on the exposed cortex while leaving the *dura mater* intact. The tests were subsequently repeated at the same sites after the *dura* had been removed. The results are reported in Figure 2-5 for one representative set of measurements. The response of the *dura*-free tissue was found to be significantly more compliant than that of the intact tissue. These observations remain qualitative in nature, as adhesion conditions of the *dura* membrane to the skull – which might be inferred to play a significant role in the indenter response – could not be accurately quantitated. The observed trends were, however, consistent with expectations since the *dura mater* had been shown to be a fairly stiff protective membrane with pseudo elastic moduli measured

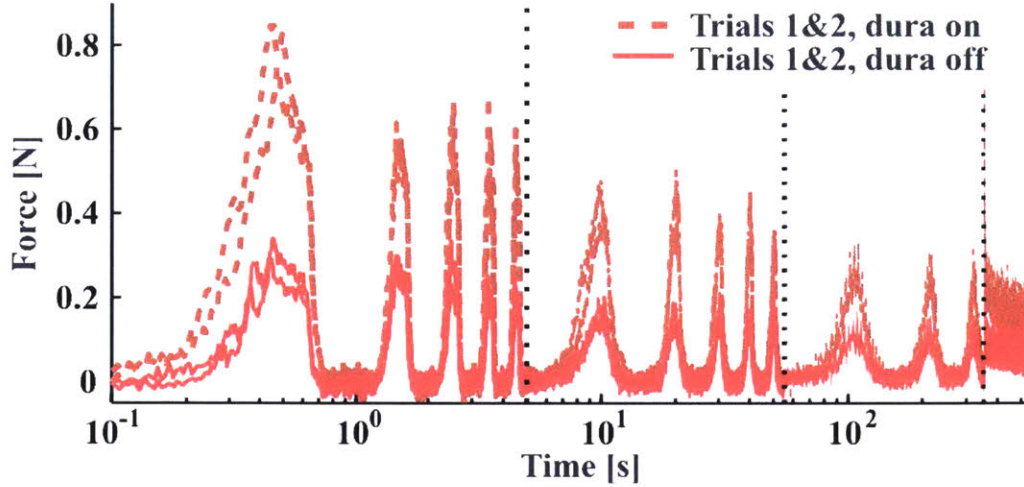


Figure 2-5: Indenter force response shown for two representative sets of measurements performed while *dura mater* was left intact ($N = 2$) and subsequently removed ($N = 2$). Cyclic loading tests at 1 Hz, 0.1 Hz and 0.01 Hz and relaxation tests are shown sequentially on the same time axis while they were actually conducted as distinct test sequences separated by 2 min recovery phases.

in tension to be on the order of 60-100 MPa [97-99].

2.4.2 Tissue recovery after indentation

The amount of residual tissue deformation observed after the two-minute recovery phase following each indentation sequence was measured *in vivo*, *in situ* and *in vitro* – via the z-counter of the vertical BiSlide – as the height differential applied to the indenter tip when readjusted to contact with the tissue surface through the tapping protocol. A summary of the residual deformation results is provided in Figure 2-6. The tissue was found to fully recover *in vivo* in most cases. After induction of euthanasia, the exposed cortical surface was measured to shift downwards by 1.5 ± 0.1 mm over the thirty-minute period preceding initiation of the indentation tests *in situ*. The tissue *in situ* never entirely recovered after a given indentation sequence; the amount of residual deformation measured between consecutive tests was on the order of 0.2-0.4 mm. Interestingly, the

Residual tissue deformation (mean \pm SD) following cyclic loading test
Dimensions in mm

	10 Hz	1 Hz	0.1 Hz	0.01 Hz
<i>In vivo</i>	0.08 \pm 0.1 (N = 8)	0.1 \pm 0.2 (N = 22)	0.1 \pm 0.2 (N = 12)	0.1 \pm 0.1 (N = 11)
<i>In situ</i>	0.2 \pm 0.2 (N = 12)	0.3 \pm 0.3 (N = 12)	0.2 \pm 0.15 (N = 9)	0.3 \pm 0.2 (N = 13)
<i>In vitro</i>	0.05 \pm 0.3 (N = 6)	0 \pm 0.2 (N = 7)	0.15 \pm 0.3 (N = 4)	0.15 \pm 0.2 (N = 3)

Figure 2-6: Residual tissue deformation measured after 2 min recovery phase following indentation tests at 10 Hz, 1 Hz, 0.1Hz, and 0.01 Hz, *in vivo*, *in situ* and *in vitro*. Average values are provided with standard deviations for all tests performed on the three non-hemorrhaged animals.

amount of residual deformation measured *in vitro* was substantially less than *in situ*.

2.4.3 Test repeatability and rate order indifference

Representative responses measured during repeated tests conducted *in vivo*, *in situ* and *in vitro* at the same indentation sites to 6 mm depth at a displacement rate of 12 mm/s (1 Hz frequency) are shown in Figures 2-7A to 2-7C. The responses to repeated indentation were found to be consistent and reproducible *in vivo*, as well as *in situ* and *in vitro*. To further assess the degree of repeatability in the mechanical measurements performed on a more quantitative basis, we compared the tissue responses to 1 Hz cyclic indentation in terms of peak force levels reached at the end of the first loading ramp for each sequence of load-unload segments applied to the tissue. These peak forces were compared within and across indentation sites according to four conditions: (I) indentation site was previously untested, (II) indentation site was previously subjected to a minimum of one sequence of five load-unload segments at 1 Hz, (III) indentation site was previously subjected to

a minimum of one sequence of two-to-five load-unload segments at a lower indentation rate (*i.e.* 0.01 Hz and/or 0.1 Hz) with no prior submission to higher rate (*i.e.* 10 Hz) indentation sequences, (IV) indentation site was previously subjected to at least one sequence of five load-unload segments at higher indentation rate (*i.e.* 10 Hz) with no prior submission to lower rate (*i.e.* 0.01 Hz and/or 0.1 Hz) indentation sequences. The results are gathered in Figure 2-7D. Although the responses measured on virgin (previously untested) sites in the *in vivo*, *in situ* and *in vitro* states were found somewhat stiffer than those obtained on previously tested sites, these differences did not reach statistical significance ($P > 0.05$ for all cases compared individually to the virgin case), thereby suggesting that pre-compressing the tissue or altering the rate order *in vivo*, *in situ* or *in vitro* does not significantly influence subsequent measurements (provided that the tissue is allowed to recover for at least two minutes between tests, tissue hydration conditions are maintained and proper contact is secured at the beginning of each test sequence). All measurements reported hereafter for a given displacement rate were therefore averaged regardless of indentation sequence order.

2.4.4 Location dependence

Repeated measurements performed *in vivo* at 1 Hz were compared quantitatively across indentation sites in terms of peak force levels reached at the end of the first (unconditioned) loading ramp and the second (conditioned) loading ramp. The results are reported in Figure 2-8. The response of the tissue was found to be weakly dependent on indentation site. Although obtained from a fairly small pool of measurements, these results suggest that the frontal and parietal lobes of the superior cortex share similar mechanical properties at the macroscopic level. All measurements reported hereafter were therefore averaged across indentation sites.

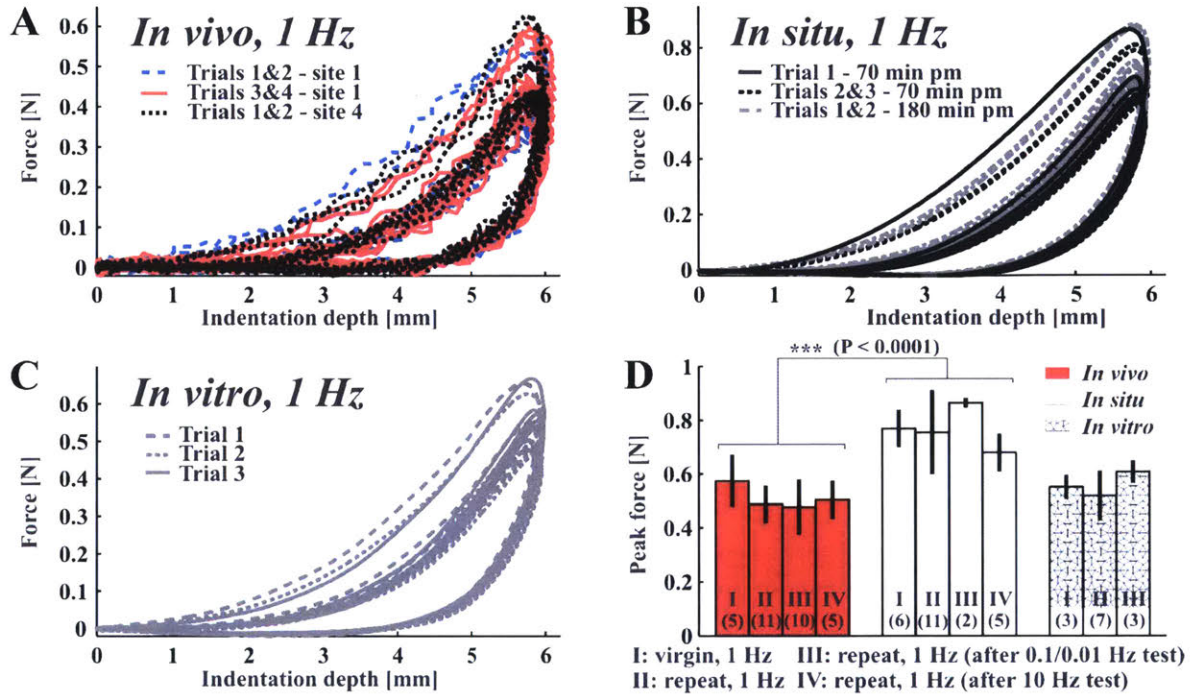


Figure 2-7: Test repeatability *in vivo*, *in situ* and *in vitro*. (A) Representative tissue responses measured *in vivo* during repeated indentation at 1Hz. (B) Representative tissue responses measured *in situ* on the same site during repeated indentation trials at various times *post mortem*. (C) Representative tissue responses measured *in vitro* for three successive trials. (D) Peak forces reached at the end of the first loading ramp *in vivo*, *in situ* and *in vitro* across four conditions. Responses measured *in vitro* under condition III corresponded to 1 Hz tests repeated after lower rate (0.01 Hz / 0.1 Hz) and faster rate (10 Hz) tests had been conducted. Numbers in parentheses correspond to numbers of measurements performed under each condition for a total of three non-hemorrhaged animals. The response *in situ* was found to be significantly stiffer than *in vivo* ($P < 10^{-4}$).

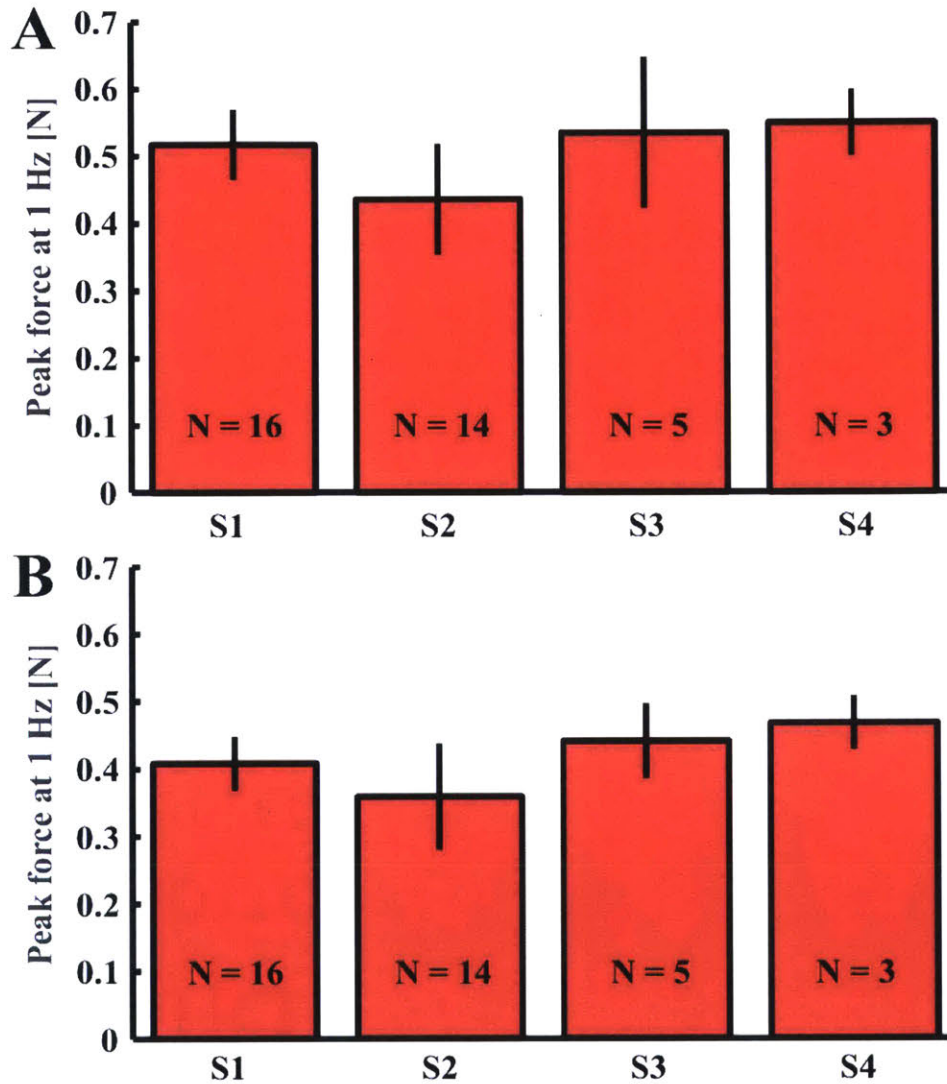


Figure 2-8: Test location dependence. Peak forces measured at the end of the first loading ramp – unconditioned response (A) – and at the end of the second loading ramp – conditioned response (B) – for the four indentation sites submitted to 1 Hz load-unload cycles *in vivo*. N refers to the number of independent measurements performed on the three non-hemorrhaged animals.

2.4.5 Post-mortem time differences

The effects of *post-mortem* test time on tissue properties were also investigated *in situ* as shown in Figure 2-7B and in Figure 2-9. No statistically significant material property changes in relation to *post-mortem* time differences (as measured via the peak forces reached at 6 mm depth upon first loading) could be found up to about three hours *post mortem* – for both the conditioned and unconditioned responses. Therefore, all measurements reported hereafter *in situ* were averaged across *post-mortem* test times.

2.4.6 Representative response *in vivo*

A representative set of indentation measurements conducted at 10 Hz, 1 Hz, 0.1 Hz and 0.01 Hz to 6 mm depth *in vivo* is shown in Figure 2-10. The tissue behavior was found highly nonlinear both in the strain and strain rate domains with marked hysteretic features. Among other notable characteristics exhibited by the tissue *in vivo* was the substantial degree of “conditioning”, meaning that the tissue response upon first loading, namely the “virgin” or “unconditioned” response, was measured to be significantly stiffer than that observed subsequently upon immediate cyclic reloading. These observations mirror those previously reported *in vitro* on cortical samples tested in uniaxial compression [80]. Note that the tissue recovered its “virgin” or “unconditioned” response when allowed to re-equilibrate for at least 2 minutes between tests.

2.4.7 Comparison with literature data

Measurements *in vivo* and *in situ* were reported previously by Gefen and Margulies in the small strain-strain rate regime [20]. When differences in indenter tip size between protocols were accounted for, it was found that the data obtained in the present study were comparable with those reported by Gefen and Margulies, both for the unconditioned and conditioned responses (Figure 2-11). Note, however, that the definition for “conditioned response” somewhat differed between the two protocols: “conditioned response” in the

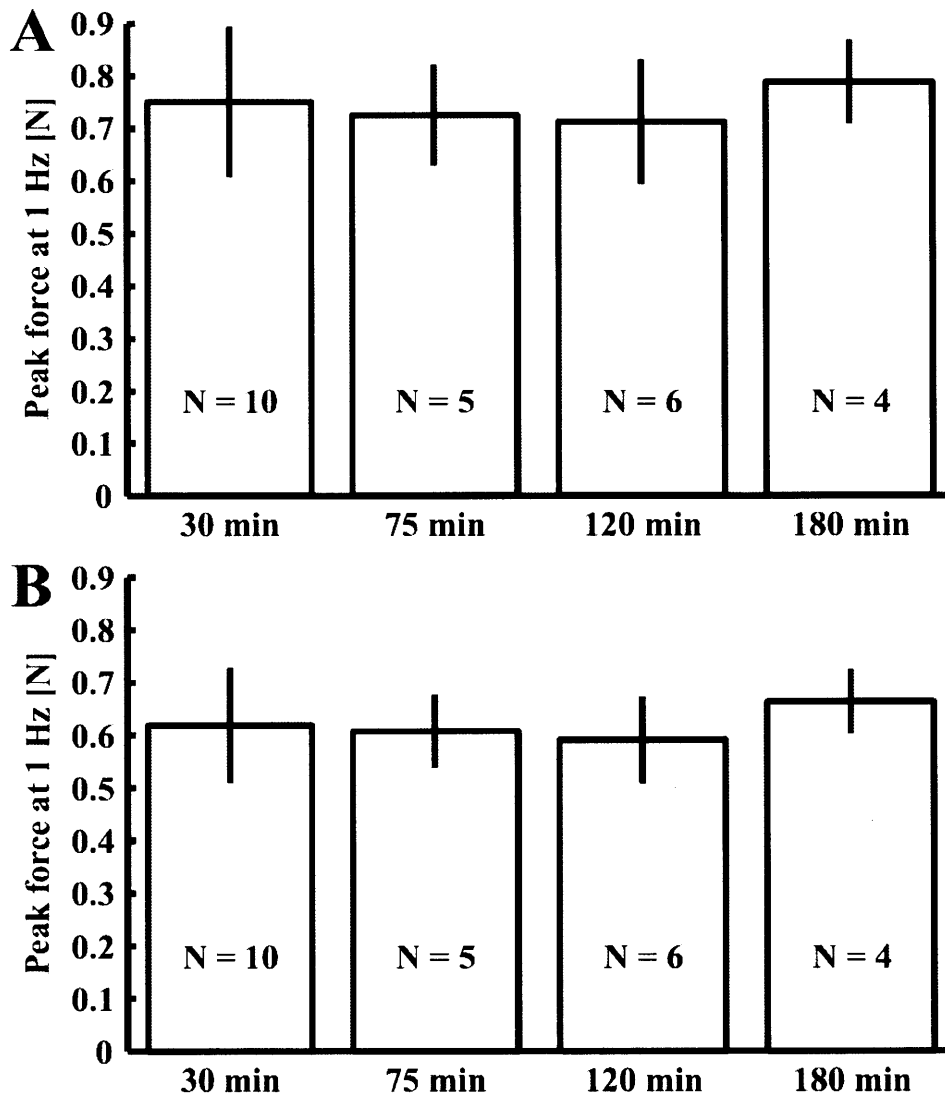


Figure 2-9: *Post mortem* time variations in situ. Peak forces measured at the end of the first loading ramp – unconditioned response (A) – and at the end of the second loading ramp – conditioned response (B) – at various times *post mortem*. N refers to number of independent measurements performed on the three non-hemorrhaged animals.

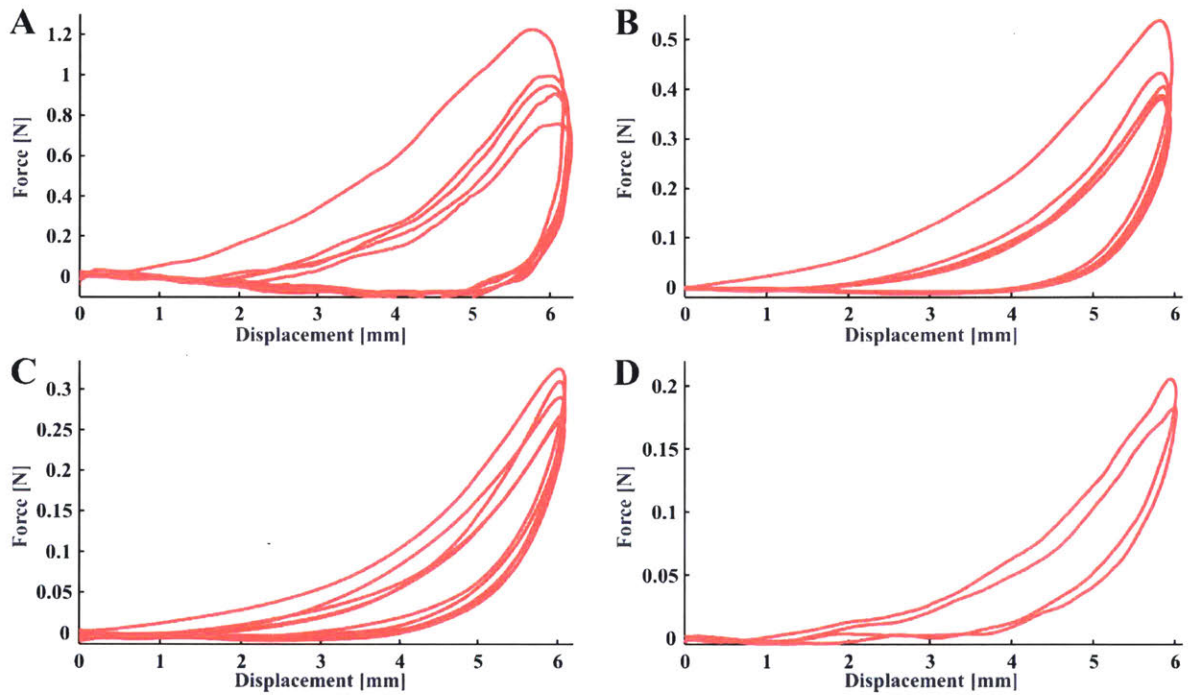


Figure 2-10: Representative tissue response measured *in vivo* at 10 Hz (A), 1 Hz (B), 0.1 Hz (C) and 0.01 Hz (D). Periodic perturbations arising from respiratory movements and blood pressure pulsations (Figure 3B) were filtered to yield the shown smoothed force-displacement profiles.

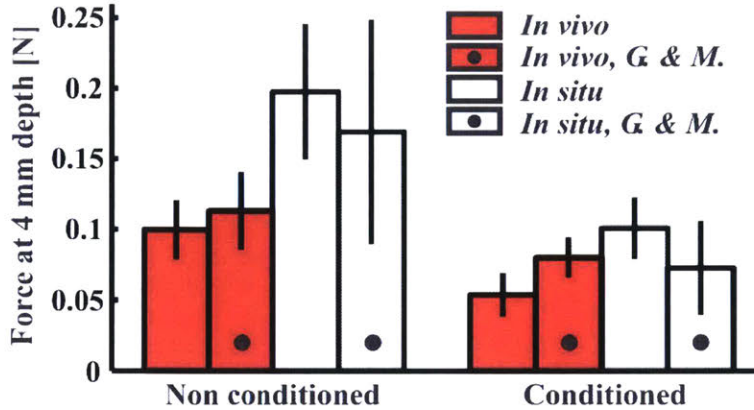


Figure 2-11: Comparison of results obtained under current protocol and under protocol developed by Gefen and Margulies [20]. Average peak forces at 4 mm depth (with standard deviations) are shown for the non conditioned and conditioned responses measured *in vivo* and *in situ*.

protocol by Gefen and Margulies referred to the combined 5th and 6th single loading ramps applied to the tissue as part of a series of 6 single ramp relaxation tests separated by 45 second recovery phases, while data selected for comparison from the present study corresponded to the 5th (and last) loading ramp imposed on the tissue as part of a single sequence of five continuously applied load-unload segments. Also to be noted is that the investigation led by Gefen and Margulies was conducted on younger porcine animals (*i.e.* one month of age), whose brain properties *in vitro* have been shown comparable to those of adult pigs [15].

2.4.8 Properties *in vivo* compared to properties *in situ*

Average responses (with standard deviations) are reported – in load-unload and relaxation – *in vivo* and *in situ* in Figure 2-12. The tissue response was measured to be stiffer *in situ* than *in vivo*, regardless of strains and strain rates. Differences in material properties between the *in vivo* and *the in situ* states were further assessed quantitatively in terms of the peak forces measured upon first (“unconditioned”) and second

(“conditioned”) loading as shown in Figure 2-12F. Differences were especially marked at low-to-quasistatic deformation rates, for which the tissue response was found to be stiffer *in situ* than *in vivo* by a factor of 1.5-2. These differences became more attenuated at higher rates of deformation, as statistical differences grew smaller (Figure 2-12F).

2.4.9 Properties *in situ* compared to properties *in vitro*

The tissue response *in vitro* was found to be more “compliant” than that measured *in situ*, with peak forces being on average 20% lower *in vitro* (Figure 2-13). These differences might be ascribed to boundary condition effects and/or to intrinsic material property changes due to temperature variations and/or tissue alteration in relation to *post-mortem* testing time.

2.4.10 Nonlinear rate dependencies

The tissue response was measured to be highly rate dependent *in vivo*, *in situ* and *in vitro* (Figure 2-13). These differences were found to be statistically significant as measured by the peak forces reached at 6 mm penetration depth ($P < 0.05$ when comparing pairs of peak forces between consecutive rates *in vivo*, *in situ* and *in vitro*). Note that the sensitivity of the tissue response to deformation rate grew higher, in relative terms, as deformation rates increased. *In vivo*, as shown in Figure 2-13, peak forces at 10 Hz exceeded those measured at 1 Hz by a factor of 2.5, whereas peak forces at 0.1 Hz exceeded those reached at 0.01 Hz only by a factor of 1.5.

2.4.11 Conditioning effects

Conditioning effects – as measured by the ratio of the peak force upon reloading (conditioned response) to that reached upon first loading (unconditioned) – were found substantial *in vivo*, *in situ* and *in vitro* (Figure 2-13D). Note that these conditioning effects tended to be more attenuated at lower rates of deformation, with conditioning ratios

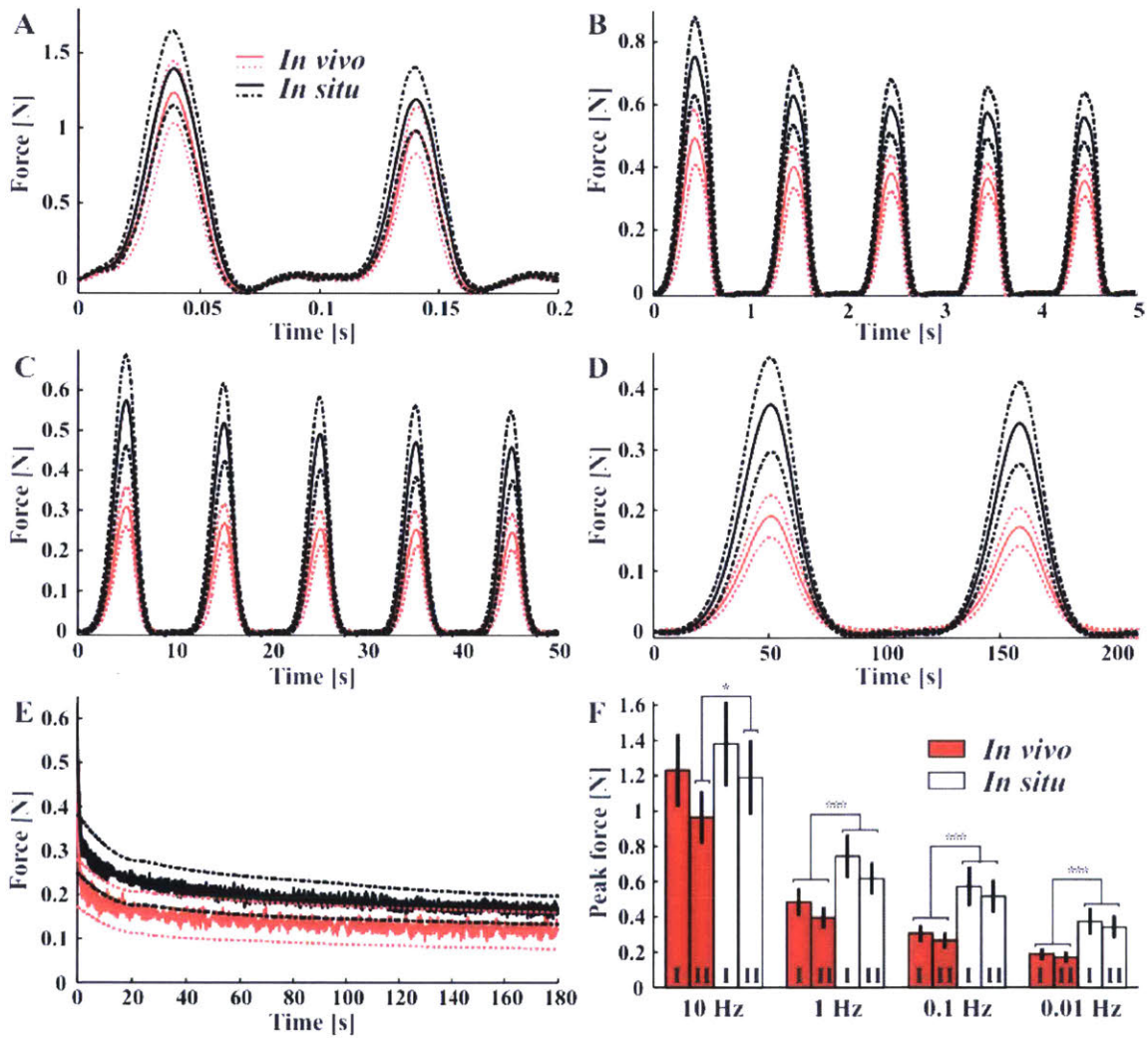


Figure 2-12: Tissue responses contrasted *in vivo* and *in situ* in cyclic load-unload at 10 Hz (A), 1 Hz (B), 0.1 Hz (C), 0.01 Hz (D), and in relaxation (E). Average responses (solid lines) and average responses plus or minus standard deviations (dashed lines) are shown in each case. For clarity purposes, only the first two load-unload cycles are shown in the 10 Hz case. (F) Response *in vivo* compared to response *in situ* in terms of peak forces reached at the end of the first loading ramp (I) and of the second loading ramp (II) for the four different rates of deformation. * and *** indicate significant ($P < 0.05$) and very significant ($P < 10^{-4}$) statistical differences respectively.

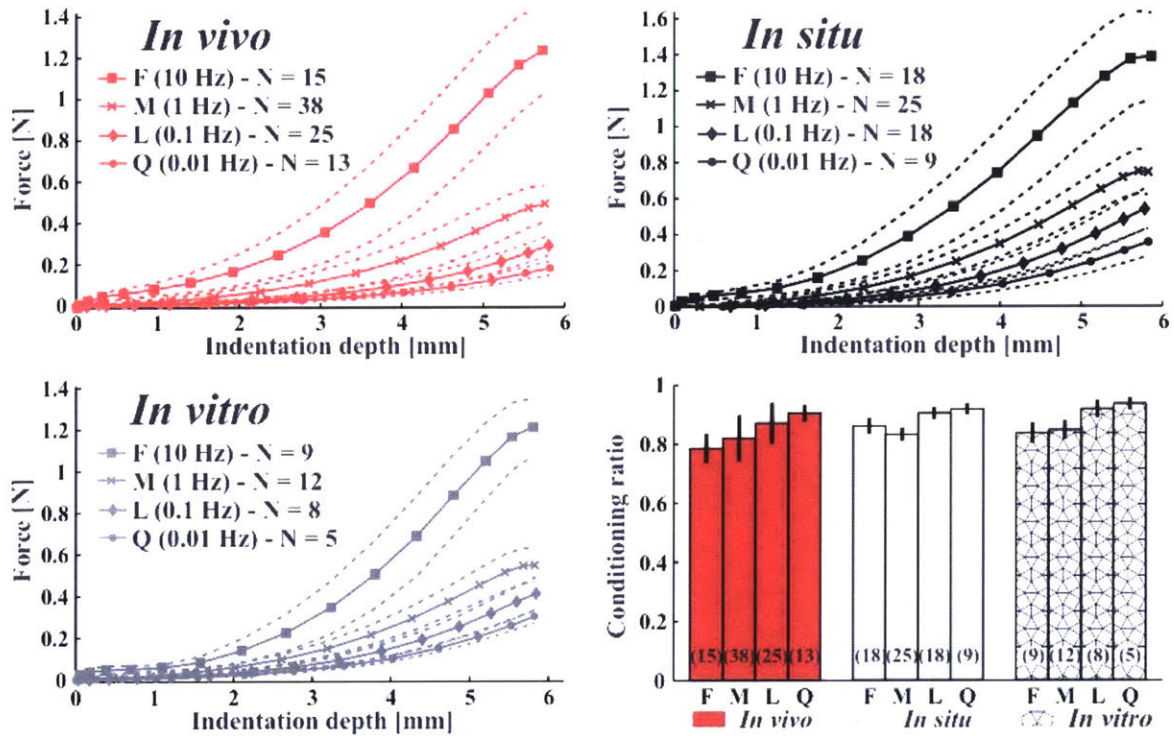


Figure 2-13: Average tissue response upon first cyclic loading *in vivo*, *in situ* and *in vitro*. Dashed lines correspond to average plus or minus standard deviation. Conditioning ratios (bottom right) are also shown for each deformation rate (F, M, L, Q) *in vivo*, *in situ* and *in vitro*. Conditioning ratio is defined as the ratio between the peak forces reached at the end of the second loading ramp (conditioned) and the peak forces reached at the end of the first loading ramp (unconditioned).

in vivo reaching 0.9 (± 0.03) on average at quasistatic rates (0.01 Hz), compared to 0.8 (± 0.05) at higher rates (10 Hz).

2.5 Discussion and conclusions

The present study reports the first body of observations on the large strain nonlinear viscoelastic properties of brain tissue *in vivo*. The set of measurements conducted addresses previously uncharacterized features of the living porcine cerebral tissue behavior at large strains and over a broad range of deformation rates (~ 0.01 to 10/s). These features could be directly contrasted with those characterizing the tissue response *in situ* and *in vitro*, thereby providing a unique quantitative basis for further refinements/adjustments of existing biomechanical models relying so far on experimental sets of *in vitro* and *in situ* measurements.

The preliminary experiments carried out on two hemorrhaged pigs allowed for rigorous test protocols to be developed minimizing measurement variability via implementation of more systematic contact determination procedures. The data sets subsequently collected on three non-hemorrhaged animals *in vivo* and *in situ* were found to be consistent and comparable with those reported by previous investigators at small strains and low rates of deformation [20]. The tissue *in vivo* was observed to recover fully after a two-minute recovery phase following each cyclic loading test. Some residual deformation was noted *in situ* after indentation. The dependence of the tissue response on indentation site was found to be weak, thereby confirming cerebral tissue mechanical homogeneity at the macroscopic level on the frontal and parietal lobes [20, 47].

The mechanical behavior of the tissue was observed to share highly similar patterns *in vivo*, *in situ* and *in vitro* – e.g. conditioning, time/rate dependencies, nonlinear strain dependencies. These patterns had already been described elsewhere on similar tissue *in vitro* in unconfined compression and in uniaxial tension [22, 79, 80]. Note that the rate effects were found to be more significant as deformation rates grew higher *in vivo*, in

situ and in vitro, with relative increase in tissue stiffness rising from $\sim 50\%$ at 0.01 Hz to 0.1 Hz to $\sim 150\%$ at 1 Hz to 10 Hz. This increase in tissue stiffness is corroborated by previous investigations where the tissue response was found to dramatically stiffen at higher rates of deformation [7, 35, 81].

Conditioning effects were found to be significant *in vivo*, *in situ* and *in vitro*. These effects could be recovered when allowing the tissue to re-equilibrate for two minutes. These observations confirm preliminary findings *in vitro* where pre-compressed tissue samples were shown to exhibit repeatable conditioning features following a two-hour recovery phase in saline solution [80]. These conditioning effects might be ascribed to interstitial water diffusion within the tissue as surmised earlier [80]. The latter inference is consistent with the fact that the amount of conditioning measured in the present study was found to be strain rate dependent, with more substantial conditioning effects observed at higher rates of deformation.

The tissue was measured to be significantly stiffer *in situ* than *in vivo*. This important observation only partially agrees with previous findings by Gefen and Margulies [20] who reported increased stiffness for the non-conditioned response only, although the latter increase was not found to be statistically significant. The fact that the tissue was measured to shrink/shift following euthanasia by 1.5 ± 0.1 mm ($N = 3$ animals) suggests that the tissue might undergo some significant “consolidation” *post mortem*, thereby accounting for the change observed in tissue compliance. Possible factors governing the consolidation process conjectured *post mortem* include: (1) the collapse of the tissue vasculature, (2) drainage of fluid-filled cavities (*e.g.* ventricles, sinuses), (3) alterations in the intrinsic mechanical properties of the structural components responsible for the neural cell resilience (*i.e.* actin filaments, neurofilaments and microtubules), and (4) tissue edema. Note that the measured tissue shift *post mortem*, although significant, remains small relative to the overall thickness of the cerebrum within the braincase (which was typically about 25 mm) so that possible stiffening artifacts arising from depth alteration effects are unlikely to account alone for the observed changes in indenter force

magnitude. Other investigators have reported similar changes in material properties between the *in vivo* and the *in situ* states on “cellular” and highly vascularized organs such as liver [94].

Among the limitations of the present study it should be noted that the data pool harvested was obtained from three animals only. Although very consistent, the measurements reported would need to be complemented by further testing. It must also be mentioned that the indentation technique employed was limited to single uniaxial force-displacement measurements. Complementary techniques relying on the use of peripheral secondary sensors around the locus of indentation may provide useful additional information on the tissue volumetric compliance as described elsewhere [26].

Finally, results gathered *in vitro* were also reported. The force-displacement response was found to be more compliant than the response measured *in situ*. This difference might be imputed to alterations in material properties due to temperature changes and/or intrinsic tissue degradation *post mortem*, or to boundary condition effects. Variations in tissue property related to *post mortem* degradation processes have been found negligible up to 15 hours *post mortem* by several investigators [38, 80] while some differences were noted by others beyond 6 hours *post mortem* [100]. Temperature variations between the *in situ* and the *in vitro* tests may have played a role in the reported changes in tissue response although temperature effects, if substantial, should have increased the tissue stiffness *in vitro* as reported when test temperature had been lowered [101]. It is therefore most plausible that material property alterations due to intrinsic tissue degradation and/or temperature changes alone could not account for the substantial differences noted in the measurements between the *in situ* and the *in vitro* states, and that boundary condition effects played a significant role. Reverse finite element modeling is therefore needed to gain better insights into the effects of boundary conditions on the resulting force-indentation response.

Taken altogether, the sets of experimental data hereby presented provide unique insights into the tissue dynamics both *in vivo* and *in situ*, and may critically guide the

development of biofidelic brain models. A reverse modeling study is currently being conducted to assess, contrast and adjust the dynamic material properties of brain tissue in the *in vivo*, *in situ* and *in vitro* states. Additional mechanical data might also be obtained at higher rates of deformation (i.e. beyond 10/s) in future *in vivo* / *in situ* / *in vitro* studies using the current dynamic indenter, which is able to operate in open-loop mode at speeds as high as 4.5 m/s. The high rate mechanical data that could be thus collected *in vivo*, *in situ* and *in vitro* through open-loop “impact” tests might potentially lead to an improved understanding of the tissue behavior under conditions approaching those suspected to prevail in blast or blunt impact traumatic brain injury scenarios.

Chapter 3

Large strain behavior of single cortical neurons

3.1 Overview

This study presents experimental results and computational analysis of the large strain dynamic behavior of single neurons *in vitro* with the objective of formulating a novel quantitative framework for the biomechanics of cortical neurons. Relying on the atomic force microscopy (AFM) technique, novel testing protocols are developed to enable the characterization of neural soma deformability over a range of indentation rates spanning three orders of magnitude – 10, 1, and 0.1 $\mu\text{m/s}$. Modified spherical AFM probes were utilized to compress the cell bodies of neonatal rat cortical neurons in load, unload, reload and relaxation conditions. The cell response showed marked hysteretic features, strong non-linearities, and substantial time/rate dependencies. The rheological data were complemented with geometrical measurements of cell body morphology, *i.e.* cross-diameter and height estimates. A constitutive model, validated by the present experiments, is proposed to quantify the mechanical behavior of cortical neurons. The models aimed to correlate empirical findings with measurable degrees of (hyper-) elastic resilience and viscosity at the cell level. The proposed formulation, predicated upon previous constitu-

tive model developments undertaken at the cortical tissue level, was implemented into a three-dimensional finite element framework. The simulated cell response was calibrated to the experimental measurements under the selected test conditions, providing a novel single cell model that could form the basis for further refinements.

3.2 Background

Traumatic brain injury (TBI) is a major cause of death and morbidity in the United States, affecting some 2 million civilians each year [78] and an estimated 20% of the 1.6 million veteran population returning from Iraq and Afghanistan [77, 101]. While the most common damage occurrences leading to mild or moderate forms of TBI (*e.g.* motor vehicle accidents or falls [73, 74, 102], sports concussions [75, 76, 103], and blast exposures [74, 104-106]) have been widely acknowledged and thoroughly reviewed, the etiology of the ensuing cognitive, behavioral or neuropsychological disorders/impairments (*e.g.* memory losses, language difficulties, concentration deficiencies, behavioral abnormalities, and/or depression) remains poorly understood. In particular, little is known about the multiple damage mechanisms suspected to unfold at the neural cell level in the seconds to hours (and probably days) following initial mechanical insult(s) to the brain, and likely to result in cell/tissue alteration. One line of approach towards elucidating some of the key damage mechanisms involved in TBI relies on addressing two distinct, yet interrelated, questions: 1) how mechanical transients applied to the organ boundary (head) translate into local stress-strain (force-displacement) distribution maps at the mesoscopic tissue level and microscopic cell level; 2) how the cell machinery responds to these mechanical stimuli. An improved quantitative knowledge of material properties at the individual central nervous system (CNS) cell level is necessary to understand the former on a quantitative basis and to better characterize the latter in a controlled environment. Such characterization inevitably calls for measurable external mechanical inputs (*e.g.* pressure waves, imposed deformation profiles) applied to the boundary of *in*

in vitro cell systems (*e.g.* 2D/3D cell culture constructs, organotypic tissue slices) can be systematically associated with reliable estimates of force and deformation magnitudes at the single cell level.

Probing mechanical properties of individual cells has been made possible in recent years through the advent of novel testing techniques (for a review, see *e.g.* [107-109]) including magnetic twisting cytometry [110-113], atomic force microscopy (AFM) [114-119], micropipette aspiration [120-125], optical tweezer stretching [126-129], and microplate rheometry [130-132]. The last three techniques, which have been successfully employed to characterize the deformability of certain cell types in suspension (*e.g.* red blood cells [122, 128], white blood cells [120, 123], Müller glial cells [129], chondrocytes [125], myofibroblasts [121], and pancreatic cancer cells [132]), may not be easily applied to CNS neuronal cultures because neurons *in vitro* form intricate networks of adherent cells interconnected via multiple processes whose continuous growth and viable maintenance require the support of a substrate. Magnetic twisting cytometry is a powerful measurement technique providing local material properties at the membrane level but is not suited to examine global properties at the cell body level. AFM, originally developed to image surfaces of inorganic materials with atomic resolution [133], has proven to be a highly versatile testing tool in mechanobiology, enabling the measurement of material properties at the cell/subcell level over a large range of forces (from pico- to nanonewton levels), speeds (from quasistatic to dynamic load levels), and length scales (from nano- to micrometers) via a variety of tip geometries [134]. The diversity in available AFM tip geometries allows for a range of experiments to be performed under various loading conditions: sharp tips may probe local properties at the cytoskeletal level while large spheres may provide global “homogenized” properties at the whole cell level. Although widely used to characterize the mechanical response of numerous cell types including fibroblasts [114], leukocytes [119], cardiac myocytes [118] and blood cells [116, 117], AFM has been infrequently utilized to examine the response of neural cells. To our knowledge, only Lu et al [129] have reported dynamic mechanical measurements on single CNS neurons – with

measurements conducted in the linear infinitesimal strain regime only. Elastic storage and viscous loss moduli were extracted from the force-displacement output of oscillating 3 μm spherical AFM probes actuated to small indentation depths at the cell surface. These measurements, aimed at characterizing some of the local viscoelastic properties of neural cells, could not provide significant insights into the global mechanical response of single neural cell bodies, nor were they directed at investigating the mechanical nonlinearities observed at finite deformation typical of anticipated cell response.

AFM mechanical measurements conducted at the (whole) cell level on other cell types have been interpreted quantitatively with the aid of various continuum models. The modeling approaches most commonly used borrow their formulation from the contact theory developed by Hertz for linear elastic materials [114, 129, 135-137], many of which typically incorporate time-dependencies inherent in the cell response [114, 129]. The Hertz contact theory, however, relies on highly reductive assumptions including linearity, homogeneity, infinitesimal deformation, and infinite substrate dimensions – all of which are unlikely to hold for biological cell systems submitted to mechanical transients. In order to address some of these limitations, investigators have proposed alternative continuum approaches integrating part of the complexities observed in the mechanical response of biological cells. These approaches include piecewise linear elastic variations [138], linear hyper-elastic/viscoelastic composite material formulations [116, 139, 140], and biphasic linear elastic constitutive relations [141, 142]. More complex variations borrow elements from continuum and piecewise continuum models [143]. While successful at capturing specific quantitative features of the cell response under selected test conditions, these formulations do not account for the combined strain and strain-rate nonlinear dependencies inherent in the cell behavior, as substantiated by a growing body of experimental observations [60, 118, 131].

The study described here provides, to our knowledge, the first reported set of experimental measurements characterizing the large-strain, nonlinear dynamic response of single cortical neurons at the soma level. The AFM “compression” tests performed on in-

dividual cell bodies via microsphere-modified cantilevers consisted of load–unload cyclic sequences over three orders of displacement rate magnitude. The mechanical data collected were analyzed further with the support of a continuum model allowing for large strain kinematics simulations of the cell behavior. The proposed model lays the foundation for further developments and refinements as more experimental results become available on a variety of related cell types and *in vitro* testing conditions.

3.3 Materials and methods

3.3.1 Cell Culture

Primary neuronal cultures were prepared from cerebral cortices of postnatal day 1 Sprague-Dawley rats (Charles River Laboratories, Wilmington, MA). Tissue was provided by the laboratory of Professor Sebastian Seung, following a protocol approved by the Committee on Animal Care at the Massachusetts Institute of Technology. The dissociation procedure was adapted from a protocol detailed elsewhere [144]. Briefly, isolated cortices were minced, rinsed 3 times in modified Hank’s buffered salt solution (HBSS) containing 25 mM HEPES, and digested for 12 minutes at 37°C with enzyme solution containing 1 mM L-cysteine, 0.5 mM EDTA, 1.5 mM CaCl₂, 200 units Papain (Sigma, P3125), and 1 μg/mL DNase (Sigma) in modified HBSS. Tissue pieces were rinsed twice in culture medium (Neurobasal medium supplemented with B27 and Glutamax (Invitrogen, 21103049, 17504044, 35050061)) and gently triturated in 1 mL ice-cold culture medium through 1 mL pipette tips. The resulting suspension was passed through a 70 μm cell strainer (BD Falcon, 352350) and subsequently centrifuged at 20 g for 7 minutes. The cell pellet was re-suspended in culture medium prior to plating at ~10⁴ cells/mL density on 35 mm poly-D-lysine (Sigma, P7886) coated coverslips (Carolina Biological Supply, Burlington, NC). Cultures were maintained at 37°C in a 5% CO₂ humidified atmosphere. 1 h after plating, cultures were rinsed to remove debris and non-adherent cells. About 3 days after plating, half of the medium was replaced. AFM measurements were ini-

tiated after 5 days in culture, *i.e.* when plated neurons had reached maturation with well-extended processes.

Neural cell viability was assessed via standard Live/Dead cytotoxicity assay (Invitrogen, L-3224). The cytoplasm of live cells and the nucleus of dead cells were stained with 2 μ M calcein AM and 2 μ M ethidium homodimer-1 respectively. Cell cultures were found viable after 5-day incubation (Figure 3-1A).

Immunocytochemistry assays were also performed to ascertain neural cell types. Anti- β -III tubulin (Abcam, ab24629) and anti-Glial fibrillary acidic protein (GFAP) (Abcam, ab4648) were used to identify neurons and astrocytes respectively. The cultures obtained for this study were confirmed to be predominantly composed of neurons, showing staining for β -III tubulin (Figure 3-1C) and not GFAP (Figure 3-1D). During AFM experiments, neurons were identified by their characteristic morphology using a light microscope.

3.3.2 Atomic Force Microscopy

Dynamic load – unload tests

Somata of single neurons were indented via an atomic force microscope (MFP 3D, Asylum Research, Santa Barbara, CA) mounted on an inverted optical microscope (Axio Observer.D1, Carl Zeiss MicroImaging Inc, Thornwood, NY). The mechanical probes selected for the tests were polystyrene spheres (45 μ m diameter, Polybead[®] Microspheres; Polysciences Inc, Warrington, PA) mounted on tipless, triangular shaped silicon nitride cantilevers (Veeco Probes NP-OW, 0.06 N/m; Nanoworld PNP-TR-TL, 0.08 N/m). The microspheres were chosen deliberately larger than the cell soma in order to approximate loading conditions close to those prevailing in “uniaxial compression” experiments. The microspheres were attached to the end of the silicon nitride probes using UV curable Loctite 3211 glue and allowed to cure for 1 h under UV light. The size and positioning of the bead were verified for one representative sample via scanning electron microscopy (Figure 3-2A). All tests, which lasted less than two hours, were conducted in culture medium at 37°C in a fluid cell chamber (BioHeater[™], Asylum Research, Santa Bar-

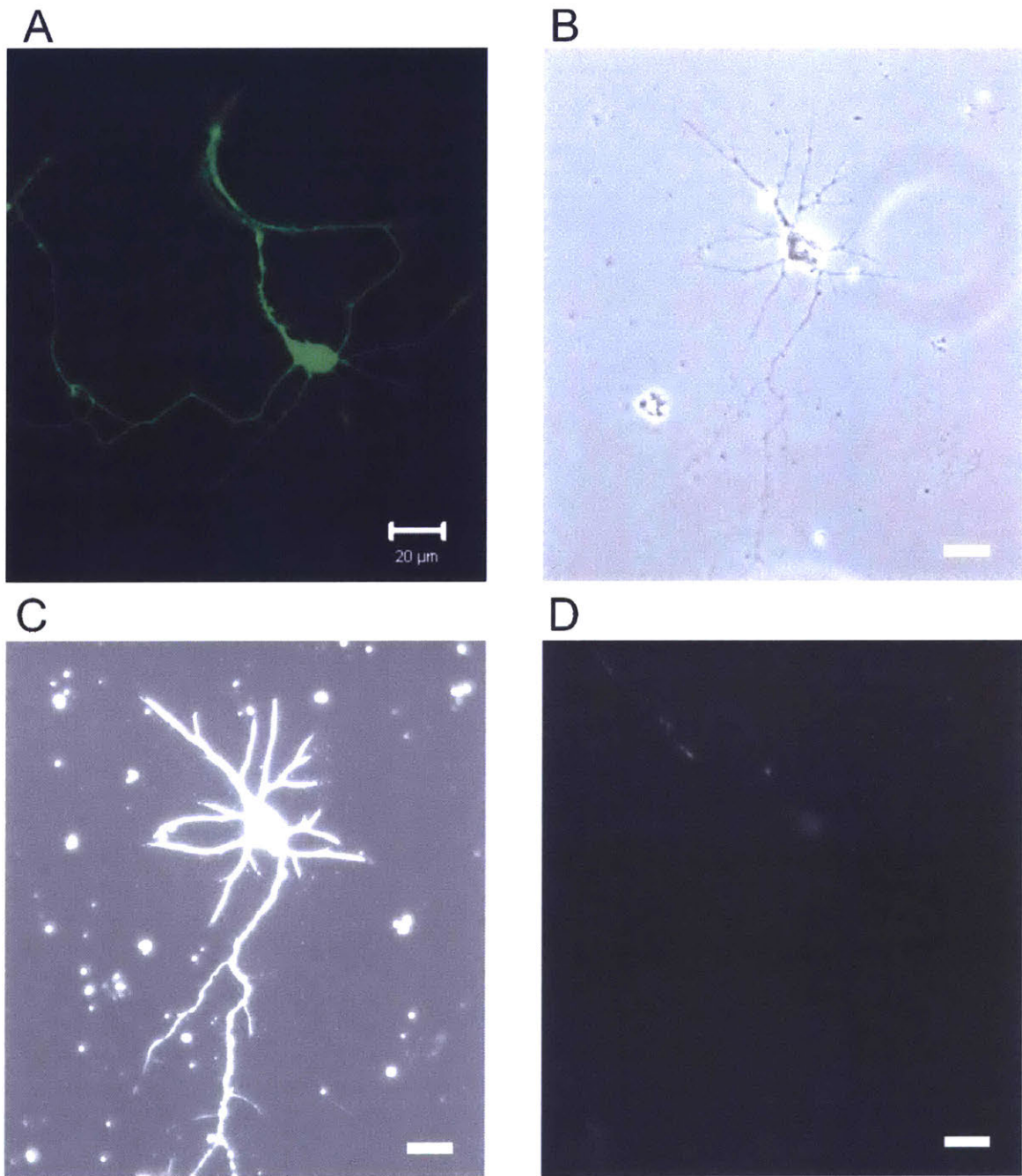


Figure 3-1: (A) Viability assay: Neuron stained with calcein-AM to verify cell viability after 5 days in culture (time of typical AFM experiment). (B) Bright field image of neuron. (C, D) Immunostaining verifying cell type: (C) Beta-III tubulin staining indicating mature neuron; (D) GFAP staining, showing glial marker not present in culture. Scale bars equal 20 μm .

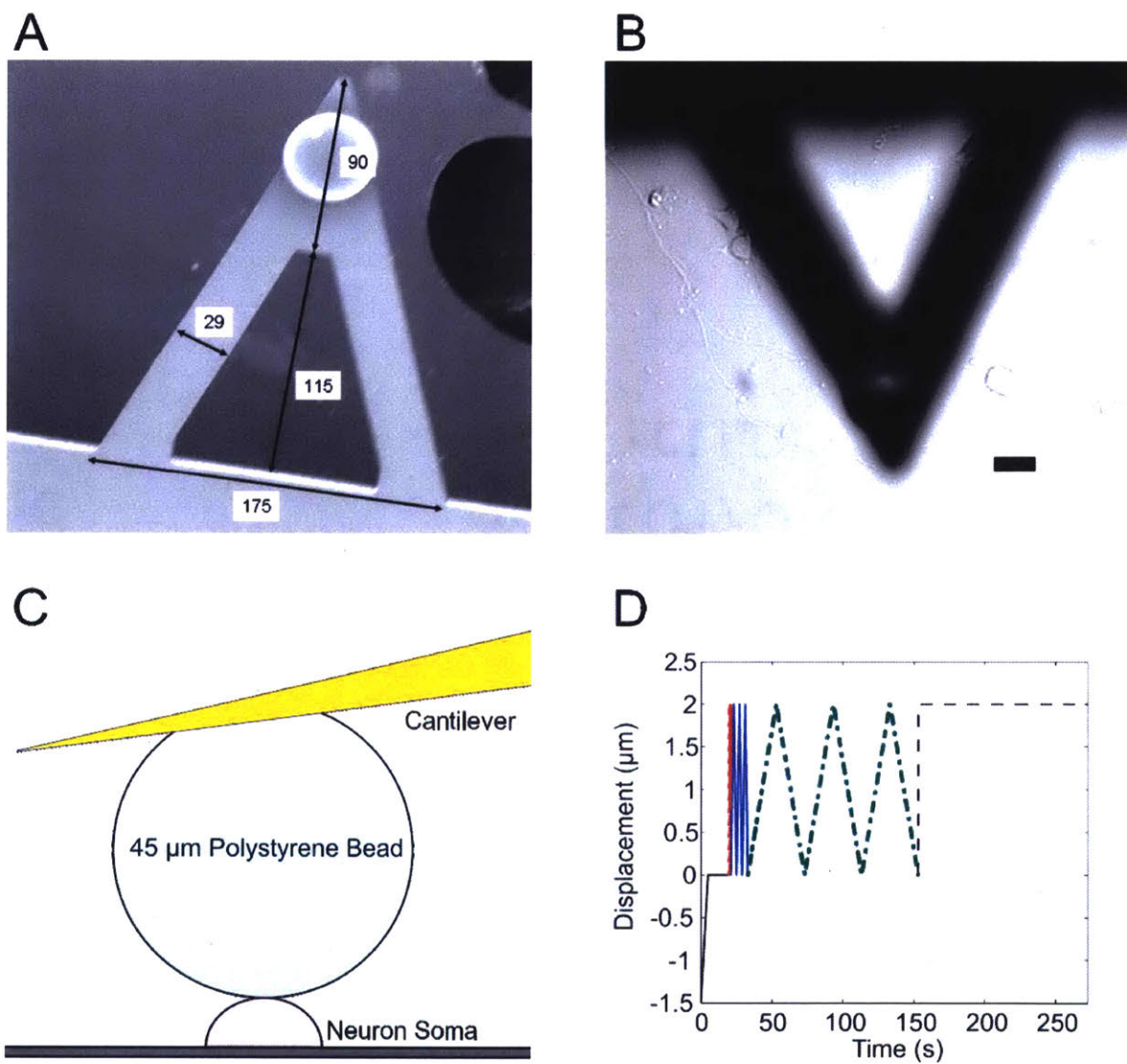


Figure 3-2: (A) SEM image of tipless cantilever with attached $45\ \mu\text{m}$ polystyrene sphere (dimensions in μm). (B) Bright field image of AFM tip with bead adjacent to neuron to be indented; $20\ \mu\text{m}$ scale bar. (C) Schematic of AFM experimental setup – Polystyrene bead compressing the cell body of a neuron plated on glass. (D) AFM testing procedure: sample approach, pre-load (black solid), sequences of load-unload segments at $10\ \mu\text{m/s}$ (red dot), $1\ \mu\text{m/s}$ (blue solid), $0.1\ \mu\text{m/s}$ (green dash-dot), followed by stress-relaxation (black dash).

bara, CA). Prior to testing, the spherical probe sitting above the sample was lowered into the medium and allowed to reach thermal equilibrium for about 30 min. Calibration of the spring constant was achieved for each probe using the thermal method [145]. Cell viability was checked by visual inspection through the bright-field optical microscope. Neurons were found well-adhered and healthy throughout the test procedure.

All tests were conducted under bright-field optical microscopy (Figure 3-2B). The cantilever tip was positioned on top of the cell body via manual actuation of the micrometric screws controlling the horizontal X-Y positioning of the AFM optical stage. The center of the cell body was aligned with the vertical Z-axis of the indenting probe through the 20X magnification objective of the microscope (Figure 3-2C). The indentation test sequence, implemented as a custom routine in IGOR Pro software (WaveMetrics, Inc, Portland, OR), consisted of an approach phase at $0.3 \mu\text{m/s}$ to a 0.3 nN contact force target followed by a 15 s dwell phase at contact with the cell body, and a subsequent series of load-unload segments at 10, 1, and $0.1 \mu\text{m/s}$ to $2 \mu\text{m}$ depth followed by a 120 s relaxation segment (Figure 3-2D). The loading rates were selected to span the broadest range of deformation speeds compatible with the MFP 3D capabilities and the physical limitations pertaining to the test configuration (*e.g.* inertial effects, hydrodynamic perturbations).

Contact point and cell size estimate

To account for some variations in the neural cell body size observed within and across cultures, height and “cross-diameter” estimates were collected for each cell body indented and subsequently incorporated in the 3D finite element simulations. The average cross-sectional diameter, derived from the optical microscope photographs taken at the time of indentation (see *e.g.* Figure 3-2B), was computed as the geometric mean between the largest and smallest edge-to-edge measured distances: $\sqrt{d_{\min} \cdot d_{\max}}$. Height estimates were obtained after completion of the indentation test, following a procedure adapted from previous cell height determination methods [137, 140]. Briefly, the cell body and

2-3 adjacent glass sites were successively indented at 10 $\mu\text{m/s}$ extension/retraction rate to a target force of 4.5 nN. The difference in piezo positions at contact between cantilever and the cell body or glass substrate were retrieved from the indentation curves to derive an estimate for the cell height (Figure 3-3). The glass-cantilever contact point was determined as the intersection between the pre- and post-contact linear fit to the measured force-displacement indentation responses whereas the cell-cantilever contact point was recovered following a hierarchical Bayesian approach detailed in section 6.1 of [146]. Briefly, the contact point and the pre- and post-contact regression coefficients were inferred – following Gibbs sampling techniques – from statistical distributions motivated by physical arguments. The post-contact force-displacement response in the small penetration depth regime was assumed to obey a polynomial law as predicted by the Hertz model for the response of an elastic substrate to indentation by a rigid sphere (*i.e.* $F \propto \delta^{3/2}$, where F is the indenter force and δ is the indentation depth). The height determination procedure was implemented in a MATLAB routine.

3.3.3 Modeling: Finite Element Simulations

The mechanical data gathered on single neural somata were interpreted with the aid of a finite element framework simulating the experimental testing conditions. The continuum formulation selected for the homogenized “material properties” of the cell response is predicated upon the modeling framework developed in our recent study of the dynamic (macroscopic) behavior of porcine cortical tissue *in vitro* [80]. This formulation exhibits rheological features (e.g. rate effects, nonlinearities, conditioning, and hysteresis) similar to those observed at the single cell level. Briefly, the selected model comprises a hyperelastic network (A) accounting for the instantaneous response of the material and a viscoelastic resistance (BCDE) encompassing the strain rate/time effects prevalent at short (B) and long (CDE) time scales. A schematic of the rheological model is provided in Figure 3-4.

Following Lee’s decomposition [57], the total deformation gradient, \mathbf{F} , applied to the

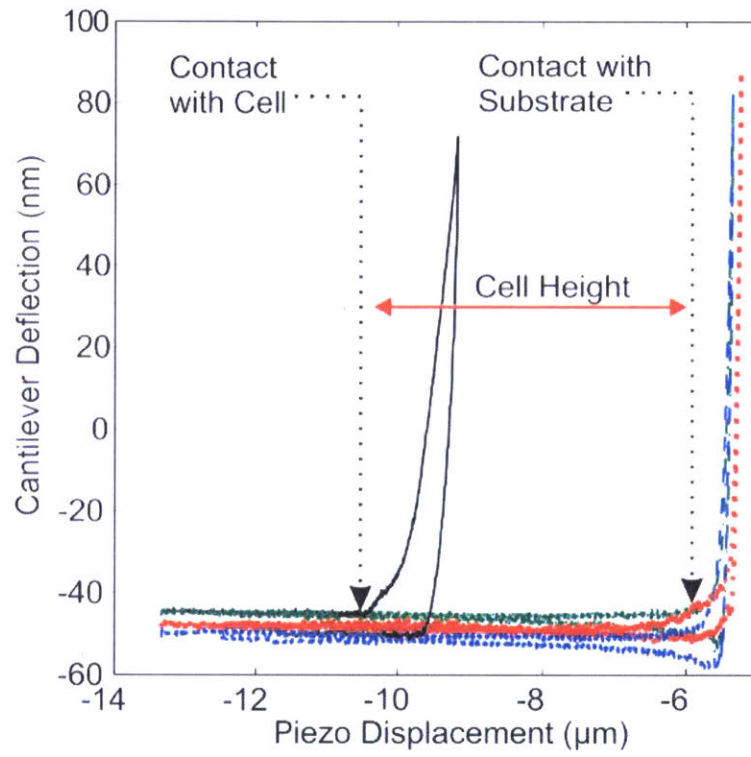


Figure 3-3: Cell height determination procedure: cell (black solid) and glass substrate (red, blue, green dash) indentation curves were used to retrieve relative piezo positions associated with contact events between cell/glass and cantilever, thereby providing an estimate for the cell height.

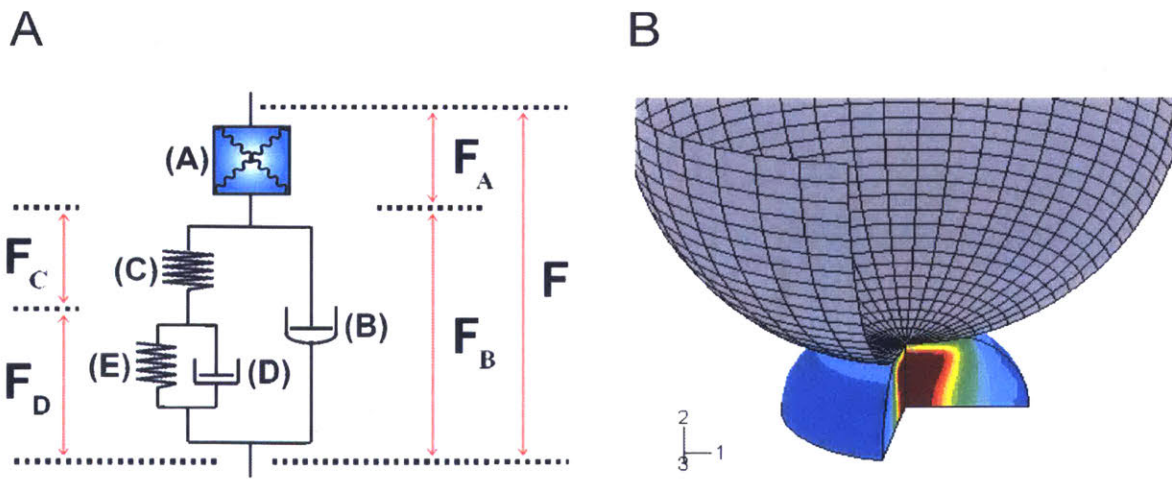


Figure 3-4: (A) Schematic of the large strain kinematics rheological model used to capture the homogenized material response of the neuron in ABAQUS. Material parameters obtained by fitting the force-indentation response to the average experimental response were found to be: $K = 10$ kPa, $\mu_0 = 16$ Pa, $\lambda_L = 1.05$, $n = 1$, $\sigma_0 = 0.005$ Pa, $G_0 = 75$ Pa, $G_\infty = 40$ Pa, $\eta = 3$ kPa.s.(B) Contour plot of von Mises stress levels in a representative finite element simulation of cell response to AFM compression.

tissue may be decomposed as:

$$\mathbf{F} = \mathbf{F}_A \cdot \mathbf{F}_B$$

where \mathbf{F}_A and \mathbf{F}_B represent, respectively, the elastic (instantaneous) and viscoelastic components of the cell deformation. The viscoelastic response of the cell is captured by the combination of a nonlinear short-term viscous element (B) and a linear viscoelastic back stress network (CDE). With regard to the backstress network, the viscoelastic deformation gradient \mathbf{F}_B is further decomposed as:

$$\mathbf{F}_B = \mathbf{F}_C \cdot \mathbf{F}_D$$

where the linear viscous element (D) models the long-term relaxation of the backstress contribution. Both \mathbf{F}_C and \mathbf{F}_D are taken to be isochoric.

The Cauchy stress \mathbf{T}_A developed within the material is decomposed into its hydrostatic and deviatoric components:

$$\mathbf{T}_A = \mathbf{T}_h + \mathbf{T}_d$$

where the hydrostatic component \mathbf{T}_h and the deviatoric \mathbf{T}_d component are physically associated with the deformation mechanisms prevailing in bulk and in shear.

The hydrostatic component \mathbf{T}_h is obtained in terms of the volumetric Jacobian, $J = \det(\mathbf{F}) = \det(\mathbf{F}_A)$, according to the constitutive relationship

$$\mathbf{T}_h = K \cdot \ln(J) \cdot \mathbf{1}$$

where K is the small-strain bulk modulus and $\mathbf{1}$ is the identity tensor. The deviatoric component \mathbf{T}_d is obtained in terms of the isochoric component of the elastic left Cauchy-Green tensor, $\overline{\mathbf{B}}_A = J^{-2/3} \mathbf{F}_A \cdot \mathbf{F}_A^T$, following a formulation derived from the freely-jointed

8-chain model for macromolecular elastic networks [59]:

$$\mathbf{T}_d = \frac{\mu_0}{J} \cdot \frac{\lambda_L}{\lambda} \cdot \mathcal{L}^{-1} \left(\frac{\lambda}{\lambda_L} \right) \cdot (\overline{\mathbf{B}}_A - \lambda^2 \mathbf{1}),$$

where

$$J \equiv \det(\mathbf{F}) = \det(\mathbf{F}_A)$$

$$\lambda^2 = \frac{1}{3} \text{tr}(\overline{\mathbf{B}}_A)$$

$$\mathcal{L}(\beta) = \coth(\beta) - \frac{1}{\beta}$$

and μ_0 and λ_L are model parameters which scale with the initial shear modulus and the limiting extensibility (locking stretch) of the network. \mathcal{L} denotes the Langevin function.

The evolution of the viscoelastic component of the deformation gradient, \mathbf{F}_B , is constitutively prescribed through the nonlinear reptation-based viscous element (B), adapted from [154]. The deformation gradient time derivative, $\dot{\mathbf{F}}_B = \mathbf{F}_A^{-1} \cdot \tilde{\mathbf{D}}_B \cdot \mathbf{F}$, is obtained by aligning the stretching tensor $\tilde{\mathbf{D}}_B$ with the direction of the (deviatoric) driving stress $\mathbf{T}_B = \mathbf{T}_d - \mathbf{T}_c$, where \mathbf{T}_c is the backstress from element (C), through the constitutive relationship:

$$\begin{aligned} \tilde{\mathbf{D}}_B &= \dot{\gamma}_B \cdot \mathbf{N}_B = \dot{\gamma}_B \cdot \frac{\mathbf{T}'_B}{\sqrt{\text{tr}(\mathbf{T}'_B \mathbf{T}'_B)}} = \dot{\gamma}_0 \cdot f_R \cdot \left(\frac{\sqrt{\mathbf{T}'_B : \mathbf{T}'_B}}{\sqrt{2}\sigma_0} \right)^n \cdot \frac{\mathbf{T}'_B}{\sqrt{\text{tr}(\mathbf{T}'_B \mathbf{T}'_B)}}, \\ f_R &= \frac{\alpha^2}{\left(\alpha + \sqrt{\text{tr}(\mathbf{F}_B \cdot \mathbf{F}_B^T)} / 3 - 1 \right)^2} \end{aligned}$$

where $\dot{\gamma}_0$ is a dimensional scaling constant ($\dot{\gamma}_0 = 10^{-4} \text{ s}^{-1}$). The reptation factor, f_R , accounts for the increasing resistance to viscous flow observed in macromolecular networks for increasing levels of accumulated viscous deformation. The factor α is a small constant introduced to eliminate the singularity at $\mathbf{F}_B = \mathbf{1}$ [64], and is set to

$\alpha = 0.005$, as in the previous tissue study [64]. The rate sensitivity exponent, n , and the strength parameter, σ_0 , are material properties.

The (deviatoric) backstress \mathbf{T}_C is obtained from the standard linear solid network (CDE) as further detailed in [80]. Briefly, the stress in the elastic elements, (C) and (E), is taken to scale linearly with the deviator of the respective Hencky strains through shear moduli G_0 , and G_∞ . The stretching tensor, $\tilde{\mathbf{D}}_D = \mathbf{F}_C \cdot \dot{\mathbf{F}}_D \cdot \mathbf{F}_B^{-1}$, in the viscous element (D) is taken to scale linearly with the driving stress in element (D) through a viscosity η .

Conceptually, element (C) is associated with short-term dissipation mechanisms, while the linear element (E) captures the long-term partial relaxation of the backstress. The eight material parameters are to be interpreted as follows: K measures the small strain bulk modulus, (μ_0, λ_L) mediate the instantaneous (elastic) response of the cell in shear, (n, σ_0) and (G_0, G_∞, η) address the time-dependencies unfolding at short and long time scales respectively. Further details on the constitutive equations and a discussion on their mechanistic interpretation are provided in [80].

The constitutive model was implemented as a user-defined material subroutine in the finite element software ABAQUS (Simulia, Providence, RI). An axisymmetric representation was selected for the test configuration as shown in Figure 3-4B. The cell body was idealized as a half oblate spheroid while the indenting probe was modeled as a (rigid) sphere. Frictionless contact was enforced between the two. The underlying glass substrate was considered rigid, in slipless contact with the cell. The physical dimensions of the soma were taken to match the measured estimates – cross-diameter and height – obtained for each cell. The entire loading history (approach – dwell – dynamic load–unload – relaxation) was simulated in ABAQUS and the material model parameters for each (homogenized) cell were determined by fitting the experimental responses, where the quality of the fit was estimated based on the error measure:

$$Error = \frac{\sqrt{\langle F_{simul} - F_{exp} \rangle^2}}{F_{exp}^{max}}$$

F_{simul} and F_{exp} refer to the discrete time vectors for the simulated and measured indenter forces respectively, and F_{exp}^{max} corresponds to the maximum reaction force as measured experimentally at the highest ($10 \mu\text{m}\cdot\text{s}^{-1}$) displacement rate.

3.4 Results

The mechanical response measured for single cortical neurons showed marked nonlinearities in the strain and strain rate domains and substantial hysteresis, as shown for one representative cell (diameter of $14.2 \mu\text{m}$, height of $7.6 \mu\text{m}$) in Figures 3-5 and 3-6. While these key response features – time/rate dependencies, nonlinearities, hysteresis – were consistently observed across the neuronal cell population ($N = 87$), some substantial variations were noted in force magnitude from one cell to the other. The average indentation response and standard deviation are reported in Figure 3-8, with the corresponding finite element model fit to the average response. The eight-parameter model captures the main characteristics of the cell behavior at large strains, including stress-strain non-linearities, rate effects and long-term time dependencies. Values for the fitting parameters are reported in Figure 3-4. Since the AFM data provided a single force-displacement history response, the material bulk and shear contributions to the macroscopic cell response could not be isolated. Following common assumptions of near incompressibility in cell biomechanics, a large value for the bulk modulus was selected, corresponding to a small strain Poisson’s ratio $\nu = 0.499$.

Given the observed wide range of variations in cell geometry, where both cross-diameter and height measurements showed some significant scatter ($D = 16.8 \pm 2.1 \mu\text{m}$; $H = 7.9 \pm 2.0 \mu\text{m}$; $N = 79$), we considered the hypothesis that the deviations in force-indentation response could be mainly ascribed to geometric effects. To investigate the validity of this hypothesis, we performed an approximate geometric normalization for the force indentation responses. A subset of cells ($N = 33$) for which height and cross-diameter estimates could be reliably obtained was selected to generate normalized plots of

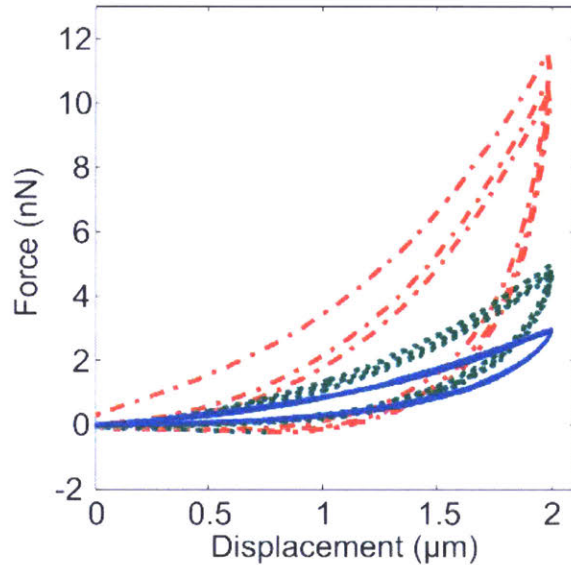


Figure 3-5: AFM data for a representative neuron of diameter $14.2 \mu\text{m}$ and height $7.6 \mu\text{m}$. Force versus displacement response at the 3 consecutive loading rates of $10 \mu\text{m/s}$ (red dash-dot), $1 \mu\text{m/s}$ (green dot), and $0.1 \mu\text{m/s}$ (blue solid).

the cell response, *i.e.* “nominal stress” versus “nominal strain” diagrams where “nominal stress” and “nominal strain” refer to force and indentation depth normalized by average cross-diameter area and height, respectively. The normalization procedure did not appear to substantially reduce the scatter in the data, indicating that the observed deviations in force-indentation responses are not simply an effect of cell geometry variations, but also reflect a degree of variability in the constitutive material response.

This degree of variability is reflected in the data provided in Figure 3-7, where the best fit model parameters for the subset of cells of known geometrical features ($N = 33$) are given in terms of their average values and ranges of variation. Sets of model parameters were obtained by fitting the individual cell responses with finite element models accounting for the actual cell geometry (height and diameter) as shown for one cell in Figure 3-6. The mean squared errors between the simulated and measured responses, which ranged between 7.4×10^{-5} and 1.37×10^{-4} , were found comparable to those obtained

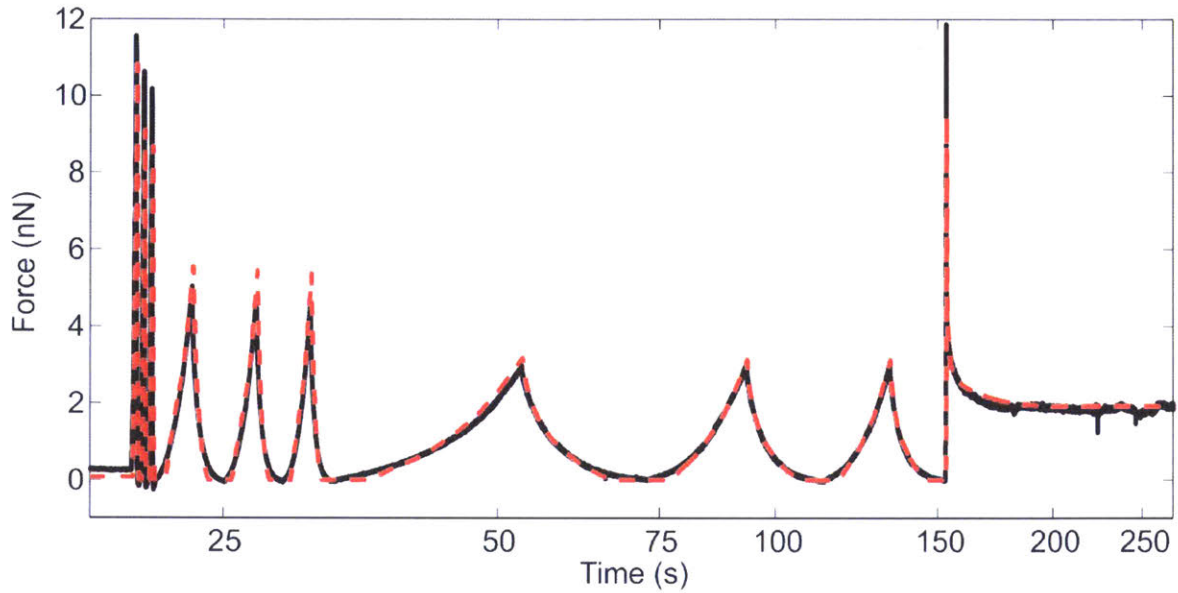


Figure 3-6: Force versus time responses measured for one representative neuron of diameter $14.2 \mu\text{m}$ and height $7.6 \mu\text{m}$ (black) and simulated in Abaqus with actual cell geometry (red dash). Material parameters were found to be: $K = 10 \text{ kPa}$, $\mu_0 = 13 \text{ Pa}$, $\lambda_L = 1.06$, $n = 1$, $\sigma_0 = 0.005 \text{ Pa}$, $G_0 = 85 \text{ Pa}$, $G_\infty = 80 \text{ Pa}$, $\eta = 3 \text{ kPa}\cdot\text{s}$. Error measure for the model fit was: 1.09×10^{-4} .

	G_0 (Pa)	n	σ_0 (Pa)	λ_L	μ_0 (Pa)	η (Pa.s)	G_∞ (Pa)
Mean	78.48	0.9927	0.005455	1.051	15.99	2879	52.64
Data Range	30-200	0.0.92-1	0.004-0.009	1.015-1.17	1-75	400-4000	7-300

Figure 3-7: Distribution in parameters (mean and data range) obtained by fitting model response to experimental data for 33 cells, accounting for actual cell configuration by varying the model geometric parameters to match the measured height and cell radius.

between the simulated and average responses reported earlier in Figure 3-6 (1.09×10^{-4}) and Figure 3-8 (1.1×10^{-4}).

3.5 Discussion

This study uncovers novel features pertaining to the large strain dynamic response of single primary neurons of the neonatal rat cortex and presents a general framework for a constitutive model in quantitative support of these observations. It is, to our knowledge, the first reported body of experimental measurements on the nonlinear, hysteretic, viscous behavior of single neural cell somata at finite deformation. The cell response was characterized over three orders of deformation rate magnitude (10, 1 and $0.1 \mu\text{m}\cdot\text{s}^{-1}$) to $2 \mu\text{m}$ depth (corresponding to a pseudo-compression nominal strain of 15 to 40 %) in load, unload and relaxation. It is found to exhibit substantial hysteresis, significant strain and strain-rate dependent nonlinearities, and marked long-term time dependencies. These findings at the single cell level mirror those reported by several investigators at the cortical tissue level [22, 34, 80] and might pave the way for a unified understanding of the mechanical dynamics unfolding from the tissue level down to the cell level in response to mechanical insults. The present testing protocols may also be adapted/refined to characterize the dynamic properties of other neural cell types and/or cell subregions (*e.g.* axon hillocks, synaptic boutons, dendritic processes), thereby providing potentially unique insights into mechanically mediated biological responses of single neural cells under complex regimes of deformation. Among the limitations of the current experimental study, we note that the volumetric compliance of the cell and its response in other modes of deformation (tensile, shear) were not investigated. In addition, some significant variations in the mechanical data collected (*e.g.* peak forces and cell compliances at large strains) were observed within the neuronal cell population considered ($N = 87$). These differences may be attributed to numerous factors including: potential inaccuracies in the cell-cantilever contact point determination, disparities in cell body geometrical fea-

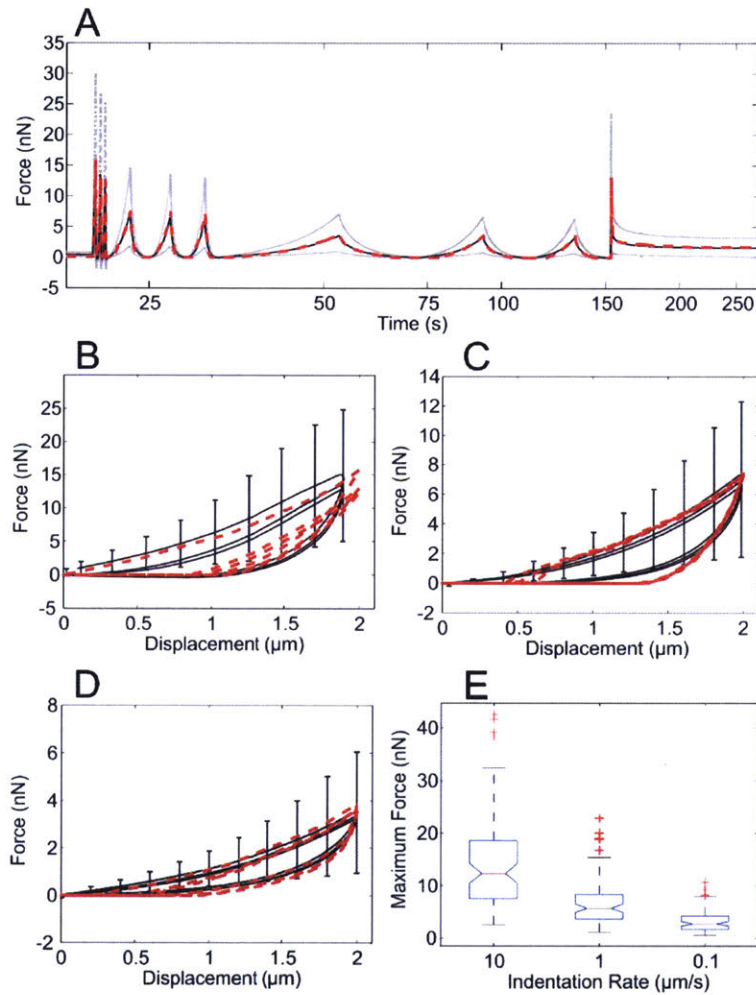


Figure 3-8: (A) Average force versus time response for 87 cells (black line) with plus and minus standard deviations (grey line); model fit (red dashes) to average response. The pictured model fit corresponds to an error measure of 1.1×10^{-4} . (B, C, and D) Average force versus displacement response at 10, 1 and $0.1 \mu\text{m/s}$ respectively. Error bars represent standard deviations and red dashes correspond to model fit. (E) Distribution in maximum force level at the end of the first loading ramp for each displacement rate. Outliers are displayed with a red + sign. Rate effects were found statistically significant ($P < 0.0001$, one way ANOVA).

tures, variations in cell/substrate contact surface area and adhesion conditions, intrinsic biological differences (cell types, development stages) in the cell population considered, and variation in initial point of contact relative to the nucleus (which has been shown stiffer than its cytoplasmic counterparts [147, 148]).

The constitutive model proposed for the homogenized cell response, following previous continuum developments undertaken at the tissue level [80], was able to capture all major complexities of the cell response in load, unload, reload and relaxation, via a relatively low number of material parameters. Although phenomenological, the model yielded quantitative assessments of different aspects of the cell response to deformation – *e.g.* elastic resilience at low to large strains, rate sensitivities in the quasi-static to dynamic regimes. As refined indicators of cell dynamics, these parameters may also elicit subtler discriminations between cell types within and across brain regions, and allow for the establishment of susceptibility-to-damage maps at the mesoscopic level. These latter considerations may be of particular significance as the potential existence of differential patterns in cell propensity for damage has been substantiated in recent years by observations of consistent mechanical heterogeneities within brain subregions [149]. The current constitutive formulation remains, however, reductive in its simplistic view of the cell as a single, isotropic continuum. The proposed modeling effort must therefore be considered as a preliminary set of constitutive framework developments – potentially enabling the establishment of local stress–strain maps at the cell level – on which structurally based multiscale model refinements may be built.

Chapter 4

Concluding remarks

The present study gathers a significant pool of experimental measurements obtained at the tissue level *in vitro*, *in situ* and *in vivo* – in compression and in indentation – on macroscopic specimens from the superior cortex of porcine brains, and at the cell level *in vitro* – in "compression" – on single neurons from neonatal rat cortices. The dynamic behavior of the tissue was characterized in compression *in vitro* over four orders of strain rate magnitude (*i.e.* $0.01\text{-}10\text{ s}^{-1}$) at large strains (*i.e.* up to 50% nominal deformation) and its volumetric compliance was also assessed at low rates of deformation ($0.01\text{-}0.1\text{ s}^{-1}$). The tissue response to indentation was measured *in vivo* over four orders of displacement rate magnitude (*i.e.* $0.12\text{-}120\text{ mm/s}$) up to 6 mm depth and it was directly compared to that observed *in situ* and *in vitro*. At the single neuronal cell level specific AFM test protocols were developed and implemented to quantify the nonlinear response features of individual somata to compressive loading up to $2\text{ }\mu\text{m}$ depth over three orders of deformation rate magnitude (*i.e.* $0.1\text{-}10\text{ }\mu\text{m/s}$).

A large strain kinematics nonlinear constitutive model was proposed to capture the main response features of the tissue and cell responses. The model was found to successfully account for most of the complexities observed at both length scales.

Among the limitations of this work it should be noted that:

- the dynamic measurements performed at the tissue and cell levels were restricted

to low and medium rates of deformation;

- no tests were conducted in shear;
- conditioning effects were not addressed via the current model formulation;
- the constitutive model has not yet been either refined or validated in indentation *in vivo*, *in situ* and *in vitro*;
- the data sets collected at the tissue and cell levels were obtained from two different animal models (*i.e.* porcine and murine models respectively).

Addressing the latter limitations may pave the way for a unified understanding of the tissue rheology at the macroscopic and microscopic levels.

Appendix A

Brain tissue response: notes on numerical implementation of constitutive model

This section briefly discusses the practical details regarding the numerical implementation of the proposed model within the user material (UMAT) subroutine of the commercial software ABAQUS. The main kinematic/constitutive equations are provided hereafter along with their explicit mathematical formulation, if relevant.

Kinematic formulation

Lee's decomposition

$$\mathbf{F} = \mathbf{F}_A \cdot \mathbf{F}_B$$

$$\mathbf{F}_B = \mathbf{F}_C \cdot \mathbf{F}_D$$

Isochoric assumption

$$\det(\mathbf{F}_B) = \det(\mathbf{F}_D) \equiv 1$$

Rate-kinematics for branches (ABC) and (CDE)

$$\mathbf{L} = \nabla_x \dot{\mathbf{v}} = \dot{\mathbf{F}} \cdot \mathbf{F}^{-1} = \dot{\mathbf{F}}_A \cdot \mathbf{F}_A^{-1} + \mathbf{F}_A \cdot \mathbf{L}_B \cdot \mathbf{F}_A^{-1} = \mathbf{L}_A + \tilde{\mathbf{L}}_B$$

$$\mathbf{L}_B = \dot{\mathbf{F}}_B \cdot \mathbf{F}_B^{-1} = \dot{\mathbf{F}}_C \cdot \mathbf{F}_C^{-1} + \mathbf{F}_C \cdot \mathbf{L}_D \cdot \mathbf{F}_C^{-1} = \mathbf{L}_C + \tilde{\mathbf{L}}_D$$

$$\tilde{\mathbf{L}}_D = \mathbf{F}_C \cdot \mathbf{L}_D \cdot \mathbf{F}_C^{-1} = \mathbf{F}_C \cdot \dot{\mathbf{F}}_D \cdot \mathbf{F}_D^{-1} \cdot \mathbf{F}_C^{-1}$$

Null-spin assumption

$$\tilde{\mathbf{L}}_B = \tilde{\mathbf{D}}_B + \tilde{\mathbf{W}}_B \equiv \tilde{\mathbf{D}}_B$$

$$\tilde{\mathbf{L}}_D = \tilde{\mathbf{D}}_D + \tilde{\mathbf{W}}_D \equiv \tilde{\mathbf{D}}_D$$

Bulk-mediated response

$$\mathbf{T}_h = K \cdot \ln(J_2) \cdot \mathbf{1} = K \cdot \ln\left(\frac{J - f_1}{1 - f_1}\right) \cdot \mathbf{1}$$

To overcome the numerical limitations encountered as J approaches f_1 , the hydrostatic stress is taken to scale linearly with J_2 beyond a certain bulk limit K_{lin} :

$$\mathbf{T}_h = K \cdot \ln(J_2) \cdot \mathbf{1} \quad \text{if } \frac{d\mathbf{T}_h}{dJ_2} \preceq K_{lin}$$

$$\mathbf{T}_h = K \cdot \ln(J_{lin}) \cdot \mathbf{1} + K_{lin} \cdot (J_2 - J_{lin}) \cdot \mathbf{1} \quad \text{otherwise.}$$

J_{lin} is defined as: $\frac{d\mathbf{T}_h}{dJ_2}(J_{lin}) = K_{lin}$. K_{lin} was set to 0.2 GPa.

Shear-mediated response

$$\mathbf{T}_d = \frac{\mu_0}{J} \cdot \frac{\lambda_L}{\lambda} \cdot \mathcal{L}^{-1} \left(\frac{\lambda}{\lambda_L} \right) \cdot (\bar{\mathbf{B}}_A - \lambda^2 \mathbf{1}),$$

$$J = \det(\mathbf{F}) \equiv \det(\mathbf{F}_A)$$

$$\bar{\mathbf{B}}_A = J^{-2/3} \mathbf{F}_A \cdot \mathbf{F}_A^T$$

$$\lambda^2 = \frac{1}{3} \text{tr}(\bar{\mathbf{B}}_A)$$

$$\mathcal{L}(\beta) = \coth(\beta) - \frac{1}{\beta}$$

The inverse Langevin function, $\beta = \mathcal{L}^{-1} \left(\frac{\lambda}{\lambda_L} \right)$, is numerically approximated as:

$$\beta = 1.31446 \cdot \tan(1.58986 \cdot x) + 0.91209 \cdot x \quad \text{if } x = \frac{\lambda_L}{\lambda} < 0.84136$$

$$\beta = \frac{1}{1-x} \quad \text{if } 0.84136 \preceq x < x_{lin}$$

$$\beta = \beta_{lin} + \frac{d\beta}{dx}(x_{lin}) \cdot (x - x_{lin}) \quad \text{if } x \succeq x_{lin}$$

The linear limit x_{lin} is defined as that for which the slope of the simulated stress-strain curve matches that of the experimental curve upon unloading (*i.e.* the instantaneous or elastic slope limit at large strain). In this study it was determined to be: $\mu_0 \frac{d\beta}{dx}(x_{lin}) = 1$ MPa.

Short and long term viscoelastic response

$$\tilde{\mathbf{D}}_B = \dot{\gamma}_B \cdot \mathbf{N}_B = \dot{\gamma}_B \cdot \frac{\mathbf{T}'_B}{\sqrt{\text{tr}(\mathbf{T}'_B)}} = \dot{\gamma}_0 \cdot f_R \cdot \left(\frac{\sqrt{\mathbf{T}'_B : \mathbf{T}'_B}}{\sqrt{2}\sigma_0} \right)^n \cdot \frac{\mathbf{T}'_B}{\sqrt{\text{tr}(\mathbf{T}'_B)}};$$

$$f_R = \frac{\alpha^2}{\left(\alpha + \sqrt{\text{tr}(\mathbf{F}_B \cdot \mathbf{F}_B^T)} / 3 - 1 \right)^2}$$

$$\tilde{\mathbf{D}}_D = \frac{1}{\sqrt{2}\eta} \cdot \mathbf{S}_D$$

$$\mathbf{S}_D = \mathbf{S}_C - \mathbf{F}_C \cdot \mathbf{S}_E \cdot \mathbf{F}_C^T$$

$$\mathbf{T}_C = \frac{1}{J} \cdot \mathbf{F}_A \cdot \mathbf{S}_C \cdot \mathbf{F}_A^T$$

$$\mathbf{S}_C = 2G_0 \mathbf{E}_C = 2G_0 \ln(\mathbf{V}_C) = 2G_0 \ln \left[\left(\mathbf{F}_C \cdot \mathbf{F}_C^T \right)^{1/2} \right]$$

$$\mathbf{S}_E = 2G_\infty \mathbf{E}_D = 2G_\infty \ln(\mathbf{V}_D) = 2G_\infty \ln \left[\left(\mathbf{F}_D \cdot \mathbf{F}_D^T \right)^{1/2} \right]$$

The left stretch tensor \mathbf{V} is the unique symmetric positive definite matrix obtained via the polar decomposition: $\mathbf{F} = \mathbf{V} \cdot \mathbf{R}$, where \mathbf{R} is the rotation matrix associated with the reorienting of the material vectors convected from the original to the current configuration.

Time integration sequence

The flow deformation gradients, \mathbf{F}_B and \mathbf{F}_D , are updated at the beginning of each time increment using an explicit time-integration scheme according to:

$$\mathbf{F} \cdot (t + \Delta t) = \frac{\mathbf{F} \cdot (t) + \Delta t \cdot \dot{\mathbf{F}} \cdot (t)}{\left[\det(\mathbf{F} \cdot (t) + \Delta t \cdot \dot{\mathbf{F}} \cdot (t)) \right]^{1/3}}$$

Initialization

The following state variables are initialized as:

$$\mathbf{F} = \mathbf{F}_A = \mathbf{F}_B = \mathbf{F}_C = \mathbf{F}_D = \mathbf{1}$$

$$\dot{\mathbf{F}}_B = \dot{\mathbf{F}}_D = \mathbf{0}$$

$$\dot{\gamma}_B = 0$$

Material jacobian

ABAQUS, in its implicit (UMAT) version, uses a Newton-Raphson scheme to determine the solution at each time increment, and requires the material jacobian to be provided within the user-defined subroutine. At large deformation, the material jacobian used by ABAQUS is defined as:

$$j = \frac{1}{J} \cdot \frac{d(J \cdot \mathbf{T})}{d(\Delta \boldsymbol{\epsilon})}$$

where $J = \det(\mathbf{F})$ is the volumetric jacobian of the deformation, \mathbf{T} is the Cauchy stress and $\Delta \boldsymbol{\epsilon}$ is the linearized incremental strain tensor. The strain measure $\Delta \boldsymbol{\epsilon}$ is given by:

$$\Delta \boldsymbol{\epsilon} = \frac{1}{2} \cdot (\mathbf{F}_t + \mathbf{F}_t^T) - \mathbf{1},$$

where \mathbf{F}_t is the relative deformation gradient computed between two successive time increments:

$$\mathbf{F}(t + \Delta t) = \mathbf{F}_t \cdot \mathbf{F}(t).$$

Note that in evaluating the tensorial derivative $\frac{d}{d(\Delta \boldsymbol{\epsilon})}$, the viscous component of the deformation gradient remains independent of the incremental strain since the evolution of the viscous deformation gradients is governed solely by the explicit time-integration sequence given above.

Appendix B

Brain tissue response: determination of material parameters

The eight material parameters to be determined for the current model are: K for the overall bulk response; (μ_0, λ_L) for the elastic shear response of network (A), (G_0, G_∞, η) for the linear viscoelastic backstress network (CDE); $(\sigma_0$ and $n)$ for the reptation-based short-term viscous response.

B.1 Preliminary parameter estimate

The following considerations were used to narrow down the search range for appropriate parameter values:

1. estimates for μ_0 and λ_L may be obtained by considering the slope of the uniaxial stress-strain curve at the onset of deformation and the instantaneous (elastic) slope upon unloading at maximum strain; μ_0 correlates with the initial shear response and λ_L correlates with the limiting stretch for the tissue extensibility. An initial guess for μ_0 falling in the [5 Pa – 100 Pa] range was found to be appropriate. In order to match the steep unloading response observed in the experimental data, initial guesses for λ_L were selected to be in the [1.02 – 1.2] range;

2. the (small-strain) bulk modulus K may be estimated by examination of the lateral stretch data. The measured stress-strain response, in conjunction with lateral stretch data can be used to obtain pressure-volumetric jacobian plots of the measured tissue response, from which an appropriate range for the bulk modulus may be obtained. In practice, an initial guess for K lying in the [200 Pa – 20000 Pa] range was found to be amply sufficient;
3. G_∞ and η govern the long-term viscoelastic response of the tissue; their ratio $\frac{\eta}{G_\infty}$, scaling with the long-term relaxation time of the tissue, was estimated to be about 100 seconds upon inspection of the long term relaxation responses. η was thus set to $100 \cdot G_\infty$ for the parameter search. Also based on the long-term equilibrium response, an initial guess for G_∞ was determined to fall in the [100 Pa – 1000 Pa] range. G_0 , which must be held sufficiently high to sustain a prompt reversal of the viscous flow at high rates but also sufficiently low to prevent any excessive stiffening at large strains and low rates, was estimated to fall in the [1 kPa – 20 kPa] range;
4. σ_0 and n modulate the onset of deformation in the nonlinear viscous element and the non-linear strain-rate sensitivity of the tissue respectively. In the experimental data collected for this study the tissue exhibited substantial rate sensitivity, so that initial guesses for the exponential coefficient n were set in the [1-5] range. As viscous flow was experimentally observed at low stress levels, initial guesses for the strength parameter σ_0 were kept below 1 kPa, with initial estimates in the [10 Pa – 1000 Pa] range.

B.2 Automated Parameter Search Algorithm

Based on these preliminary considerations, a systematic automated search was conducted using the Nelder-Mead simplex algorithm [67, 68] implemented in a MATLAB subroutine. The seven-variable $(\mu_0, \lambda_L, K, G_\infty, G_0, \sigma_0, n)$ error function minimized via the

search algorithm is defined in terms of a weighted mean-squared difference between the experimental and modeled stress and lateral stretch histories:

$$error = \frac{1}{|s_{exp}^{max}|} \cdot \|w_s \cdot (s_{exp} - s_{model})\| + \gamma \cdot \|w_\lambda \cdot (\lambda_{exp} - \lambda_{model})\|$$

where $\|\cdot\|$ is the Euclidian norm; (s_{exp}, λ_{exp}) and $(s_{model}, \lambda_{model})$ are the discrete-time nominal stress and lateral stretch vectors obtained experimentally and numerically respectively; $|s_{exp}^{max}|$ is a normalization factor equal to the peak nominal stress value at 1 s^{-1} strain rate; γ is a bias factor discussed hereafter; w_s and w_λ are weighting vectors designed to increase the significance of the tissue response as strains/stresses grow larger:

$$w_s [i] = \frac{1}{\sum_j w_s [j]} \cdot \left(1 + \left| \frac{s_{exp}[i]}{s_{exp}^{max}} \right| \right)$$

$$w_\lambda [i] = \frac{1}{\sum_j w_\lambda [j]} \cdot (1 + 10^5 \cdot |\lambda_{exp}[i] - \lambda_{exp}[0]|)$$

The discrete lateral stretch vector λ_{exp} was sampled from the portion of the response for which reliable volumetric measurements were available, *i.e.* over the five load-unload cycles at 0.1 s^{-1} and the first load-unload cycle at 0.01 s^{-1} . The weighting factor γ modulating the lateral deformation portion of the error function was set to 2 to compensate for the diminished pool of available lateral stretch data.

Upon starting the simplex minimization scheme, the user provides an initial guess for the seven material parameters along with lower and upper bounds for each of them. Note that this direct search method does not necessarily converge to a minimizing point. The algorithm was therefore run repeatedly starting from various initial guesses selected within the ranges determined via the preliminary parameter estimate. The search results are shown for one representative set of seed points in Figure B-1. The automated search provided a remarkably consistent set of material parameters. The latter parameter estimates were slightly readjusted manually to capture subtle features of the response

(*e.g.* nonlinear behavior in the low strain range, volumetric compliance at large strains) that the global error measure employed for the optimization search procedure could not specifically account for. The mean-squared error obtained via the supplementary manual fit was of the same order as that found via the automated search – *i.e.* $\sim 3.5 \cdot 10^{-3}$. The final selected set of material parameters is reported in Figure 1-6.

B.3 Parameter estimates for “outlying” cases

Using the parameter estimates obtained for the average tissue response as the baseline, additional fits were performed manually to assess the sensitivity of the material parameters to deviations from average tissue response. Two “extreme” cases were selected – labeled as “stiff” and “compliant” – for which the axial stresses and lateral stretches measured upon loading in the large strain regime deviated from average by about plus and minus one standard deviation respectively. The results are reported in Figure B-2. The most prominent differences in material response could be accounted for by altering the bulk parameter and long-term viscous coefficients while retaining the remaining parameters virtually unchanged.

Parameter	Range	Seed 1	Seed 2	Seed 3
μ_0 [Pa]	[5 – 100]	17 (20)	12 (50)	25 (80)
λ_L	[1.02 – 1.2]	1.09 (1.04)	1.09 (1.1)	1.11 (1.15)
K [Pa]	[$2 \cdot 10^2$ – $2 \cdot 10^4$]	1095 (10^3)	1100 ($5 \cdot 10^3$)	1079 ($1.5 \cdot 10^4$)
n	[1 – 5]	3.66 (2)	3.8 (2.5)	2.7 (3.5)
σ_0 [Pa]	[10 – 1000]	47 (50)	49 (100)	21 (800)
G_0 [Pa]	[10^3 – $2 \cdot 10^4$]	4204 ($2 \cdot 10^3$)	5000 (10^4)	3835 ($1.5 \cdot 10^4$)
G_∞ [Pa]	[100 – 1000]	491 (200)	634 (500)	528 (800)
Error	-	$2.8 \cdot 10^{-3}$ ($3.3 \cdot 10^{-2}$)	$2.8 \cdot 10^{-3}$ ($1.8 \cdot 10^{-2}$)	$2.9 \cdot 10^{-3}$ ($3.4 \cdot 10^{-2}$)

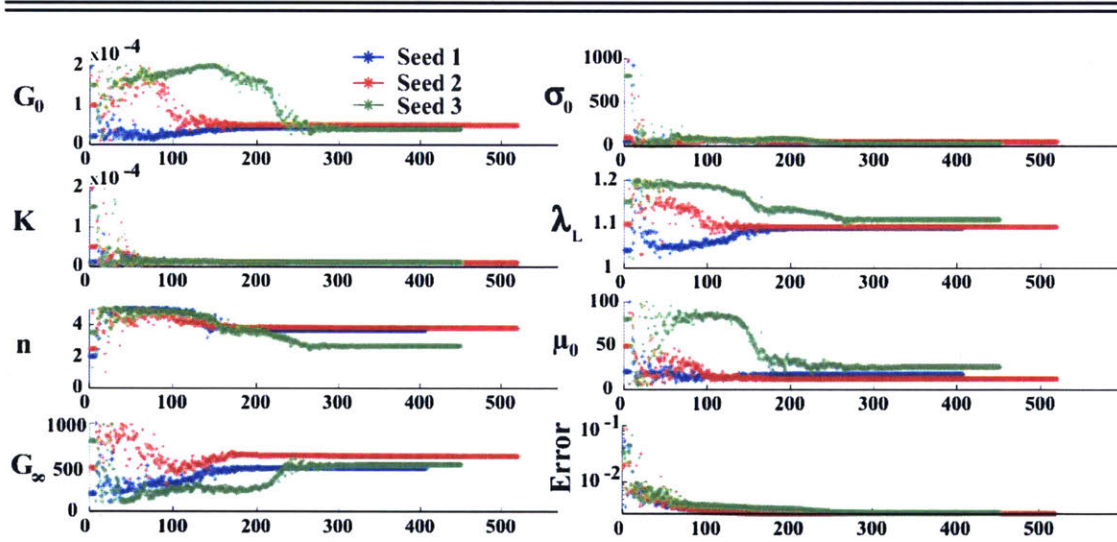


Figure B-1: Summary of parameter search results obtained from three independent parameter seeds (starting guesses) using the simplex optimization method. The experimental data used for the automated fitting procedure were the representative sets of axial and lateral measurements provided in Figures 1-3 and 1-5D respectively. For each seed (top table), the converged parameter values are reported along with the corresponding starting seed in parenthesis. The range indicated for each material parameter corresponds to the investigation domain over which the automated algorithm was allowed to search for minima. The material parameter and error function evolutions for the search procedure are shown in the bottom graphs (iteration numbers reported on the x-axis).

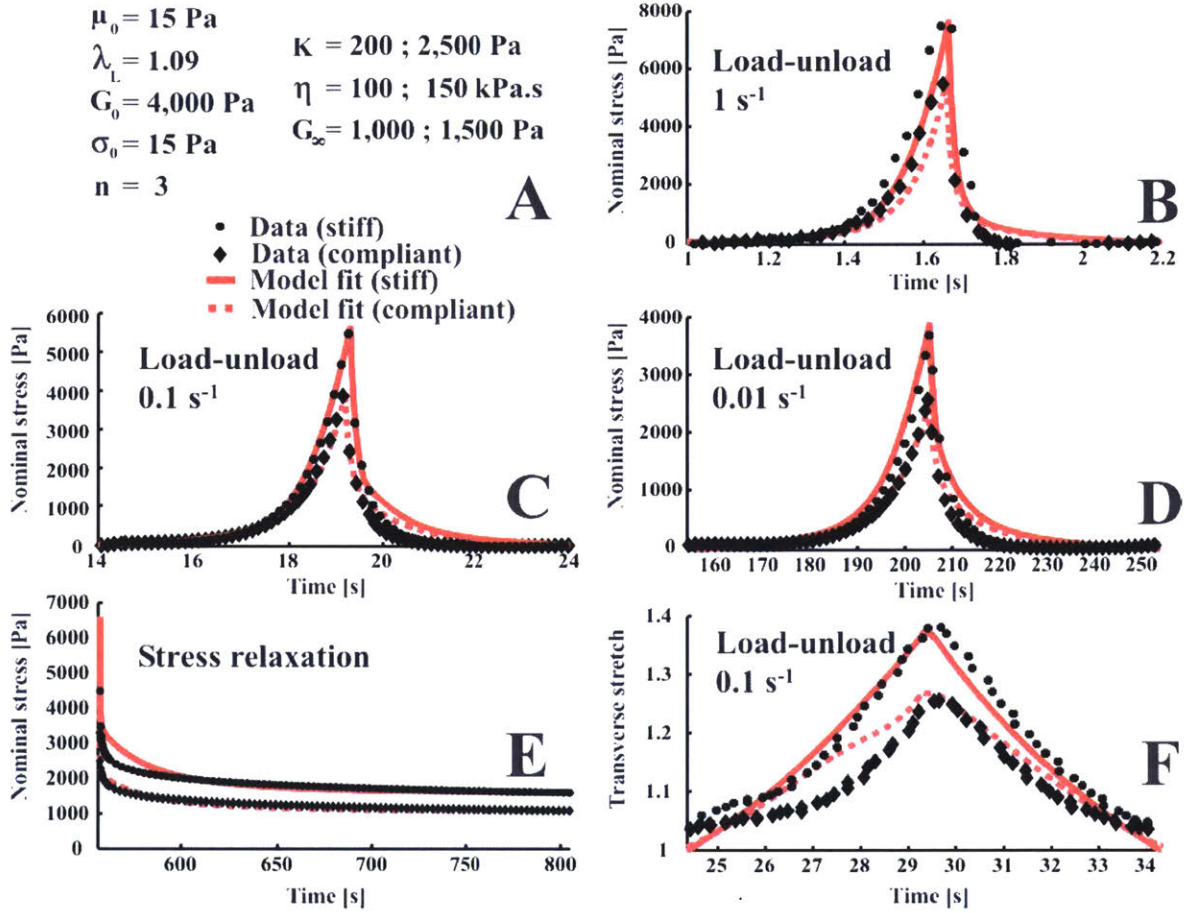


Figure B-2: Model fit to responses measured in unconfined uniaxial compression from two “outlying” samples whose axial stresses and lateral stretches developed upon loading at large strains deviated from average by about plus and minus one standard deviation (labeled as “stiff” and “compliant” respectively). (A) Optimized material parameters. Only K , G_∞ , and η differed between the two outliers (stiff/compliant). The low and high values provided for each of these latter parameters correspond to those associated with the compliant and stiff responses respectively. (B), (C), (D) and (E) Axial tissue responses (measured and simulated) for both outlying cases. (F) Associated lateral deformations (measured and simulated). For clarity purposes, only the second load-unload segments are provided for each strain rate (at a decreased sampling rate). The weighted mean-squared errors between the responses simulated and measured over the entire loading history (see appendix for error definition) were found to be $3.3 \cdot 10^{-3}$ (stiff) and $4.8 \cdot 10^{-3}$ (compliant).

Appendix C

Summary of results obtained on hemorrhaged animals

The preliminary phase of the indentation tests detailed in Chapter 2 comprised measurements performed on two donor hemorrhaged animals. These latter tests were conducted prior to implementing the "tapping" contact protocol, by establishing contact between tissue and indenter tip through visual inspection. The main results obtained via this somewhat imprecise visual inspection approach are reported hereafter.

C.1 Effect of *dura mater* on tissue response

The response of the *dura*-free tissue was measured to be significantly more compliant than that of the intact tissue (Figure C-1).

C.2 Properties *in vivo* compared to properties *in situ*

The tissue response was found to be significantly stiffer *in situ* than *in vivo* (Figure C-2).

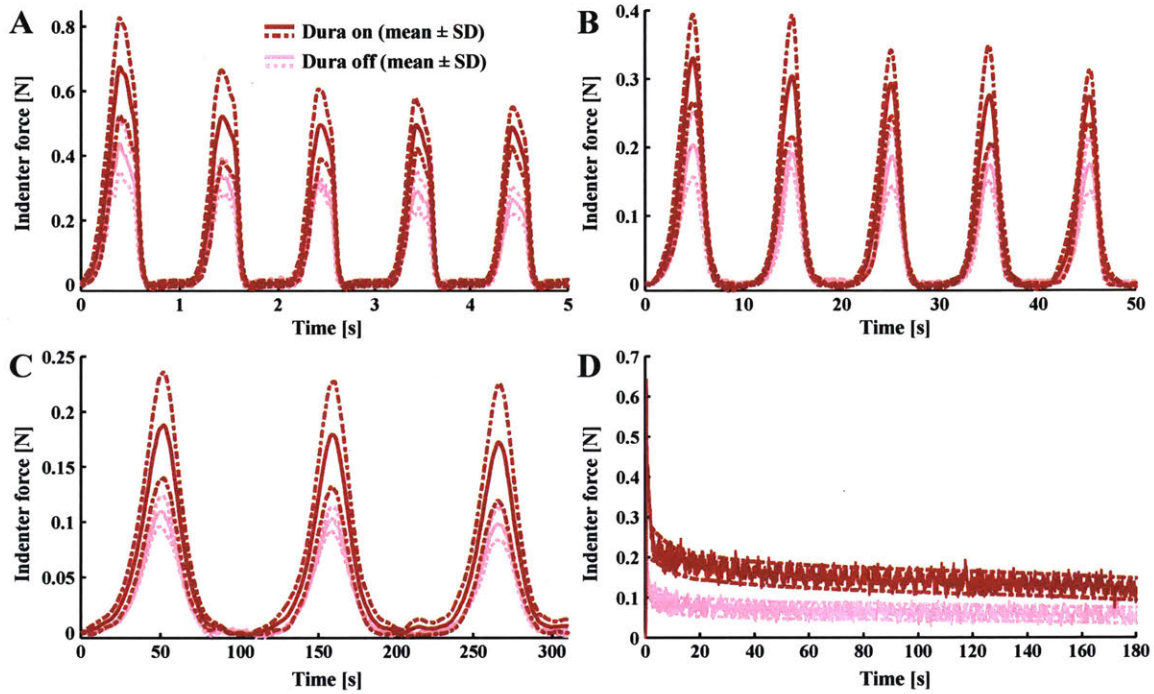


Figure C-1: Average indenter force response measured on intact tissue ("Dura on") and on *dura*-free tissue ("Dura off"). Dashed lines correspond to average plus or minus standard deviation. Results are shown for tests conducted in cyclic load-unload at 1 Hz [(A), N(Dura on) = 6, N(Dura off) = 3], 0.1 Hz [(B), N(Dura on) = 4, N(Dura off) = 3], 0.01 Hz [(C), N(Dura on) = 2, N(Dura off) = 2], and in relaxation [(D), N(Dura on) = 3, N(Dura off) = 3].

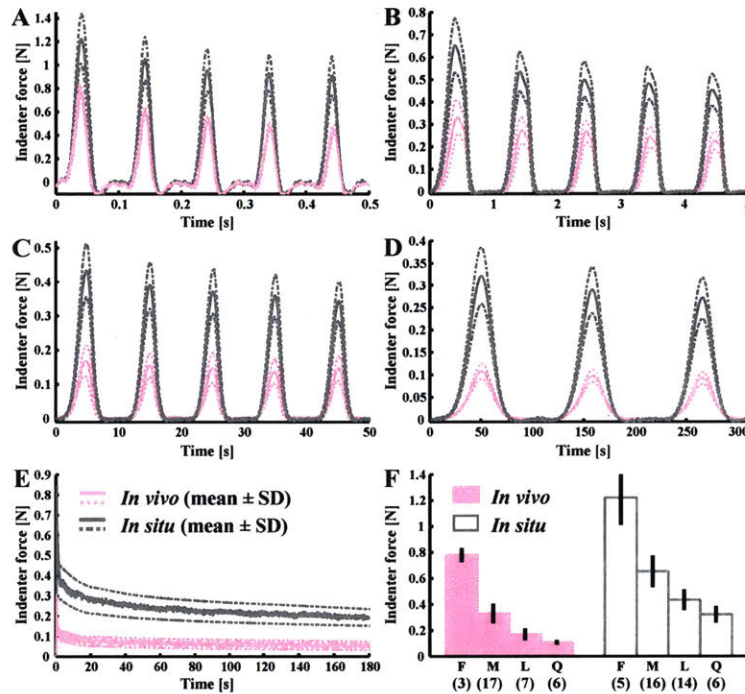


Figure C-2: Tissue responses contrasted *in vivo* and *in situ* in cyclic load-unload at 10 Hz (A), 1 Hz (B), 0.1 Hz (C), 0.01 Hz (D), and in relaxation (E). Average responses (solid lines) and average responses plus or minus standard deviations (dashed lines) are shown in each case. (F) Response *in vivo* compared to response *in situ* in terms of peak forces reached at the end of the first loading ramp at 10 Hz ("F"), 1 Hz ("M"), 0.1 Hz ("L"), 0.01 Hz ("Q"). Numbers reported in parentheses correspond to numbers of independent measurements (*i.e.* N) obtained for each case.

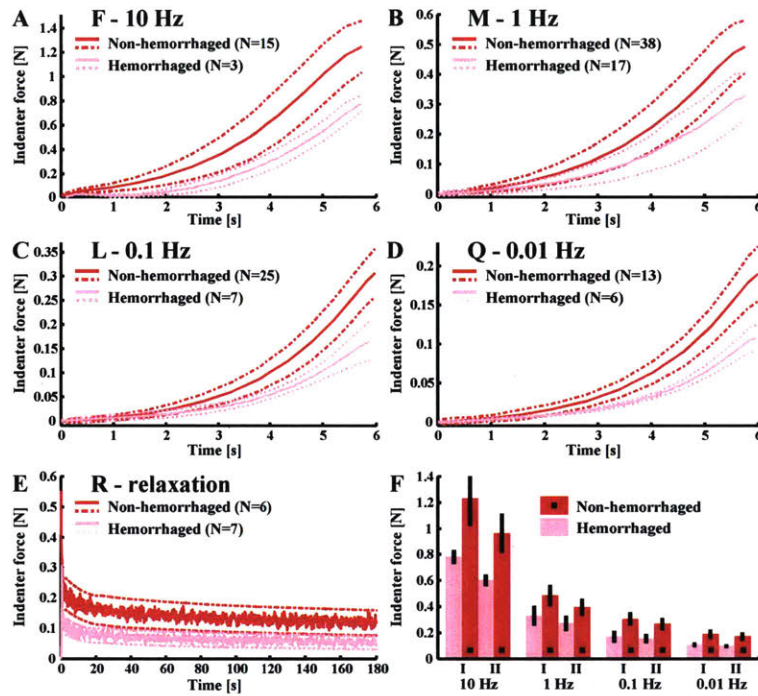


Figure C-3: Average tissue response upon first cyclic loading (A, B, C, D) and in relaxation (E) for the hemorrhaged and non-hemorrhaged cases *in vivo*. Dashed lines correspond to average plus or minus standard deviation. Peak forces reached at the end of the first loading ramp (I) and of the second loading ramp (II) are also shown for each deformation rate in panel F.

C.3 Properties *in vivo*, *in situ* and *in vitro* compared between the hemorrhaged and non hemorrhaged cases

The tissue response from the two hemorrhaged animals was observed to be more compliant than that from the three non hemorrhaged animals *in vivo*, *in situ* and *in vitro*. It remains unclear whether these differences were due to changes in tissue contact protocols or to intrinsic material property variations.

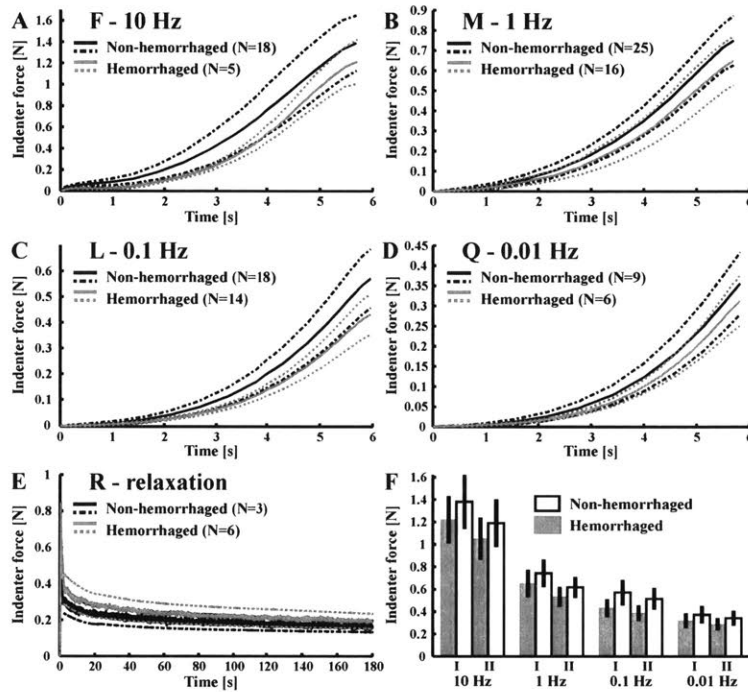


Figure C-4: Average tissue response upon first cyclic loading (A, B, C, D) and in relaxation (E) for the hemorrhaged and non-hemorrhaged cases *in situ*. Dashed lines correspond to average plus or minus standard deviation. Peak forces reached at the end of the first loading ramp (I) and of the second loading ramp (II) are also shown for each deformation rate in panel F.

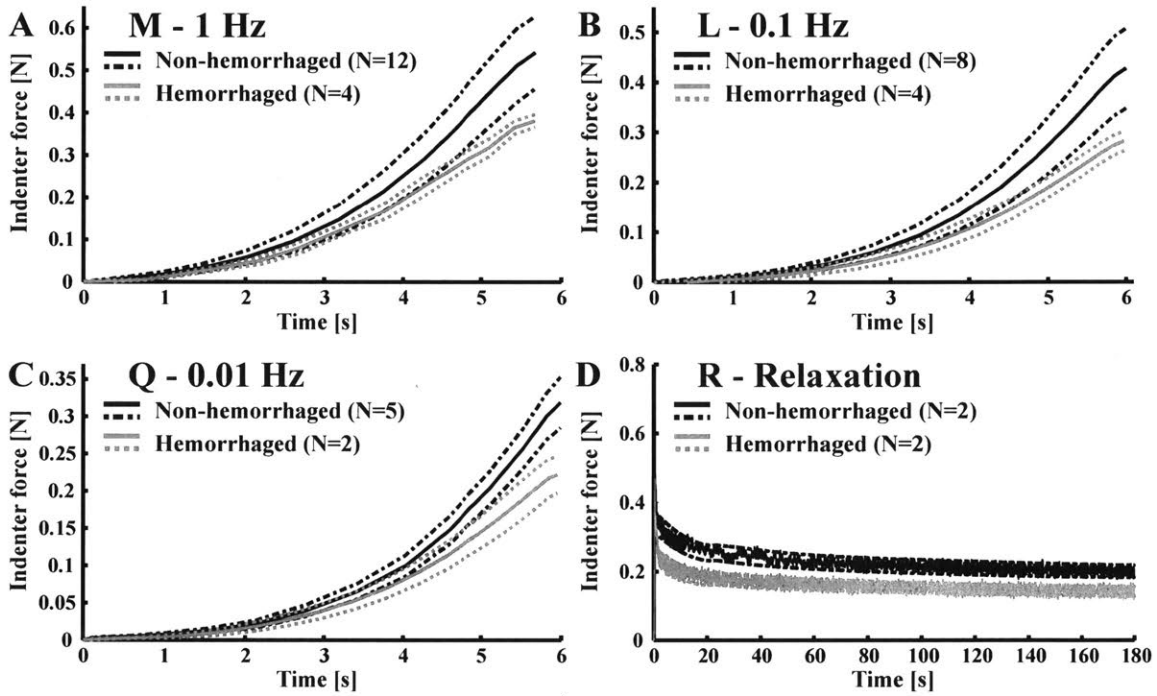


Figure C-5: Average tissue response upon first cyclic loading (A, B, C) and in relaxation (D) for the hemorrhaged and non-hemorrhaged cases *in vitro*. Dashed lines correspond to average plus or minus standard deviation.

Appendix D

Preliminary assessment of tissue volumetric compliance in indentation *in vitro*

Tests were conducted in indentation *in vitro* following a protocol identical to that described *in vitro* in Section 2.3.3. Secondary sensors tracking surface motion of the tissue around the indenter [26] were positioned at a distance of 10 mm from the indenter axis (Figure D-1). The results reported hereafter were obtained from three 6-month old porcine subjects (Yorkshire, female). They shall be viewed as preliminary results since no rigorous contact method was implemented for these tests.

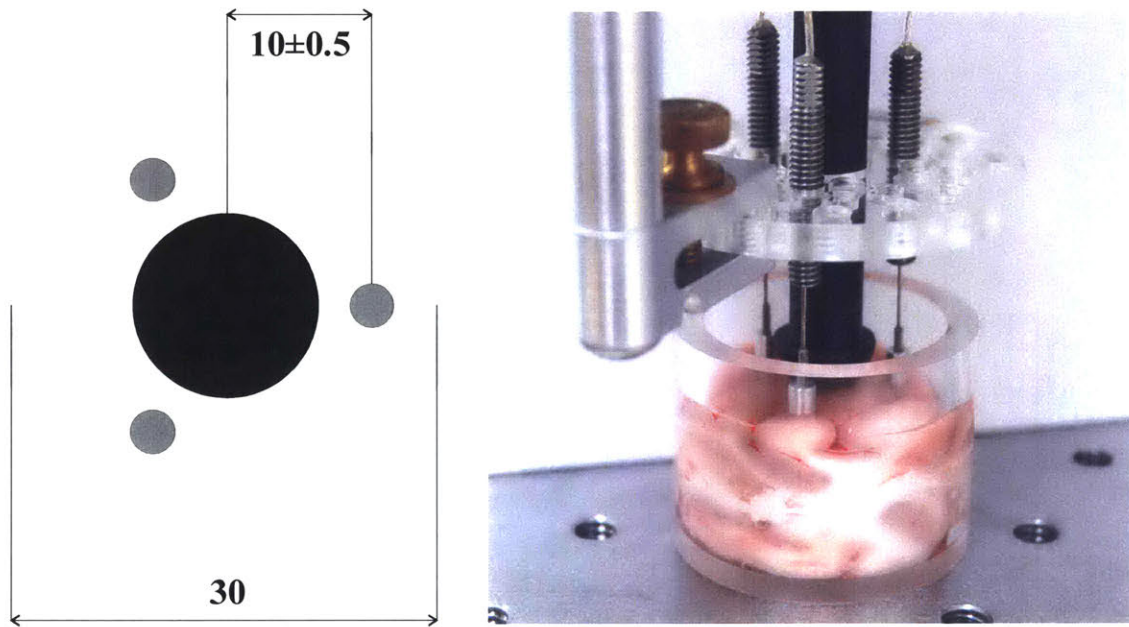


Figure D-1: Experimental setup (right panel) corresponding to indentation tests conducted *in vitro* with three secondary sensors. Schematic of test configuration (left panel) with relative positions of secondary sensors (small grey circles) and indenter (larger black circle). Dimensions are in mm.

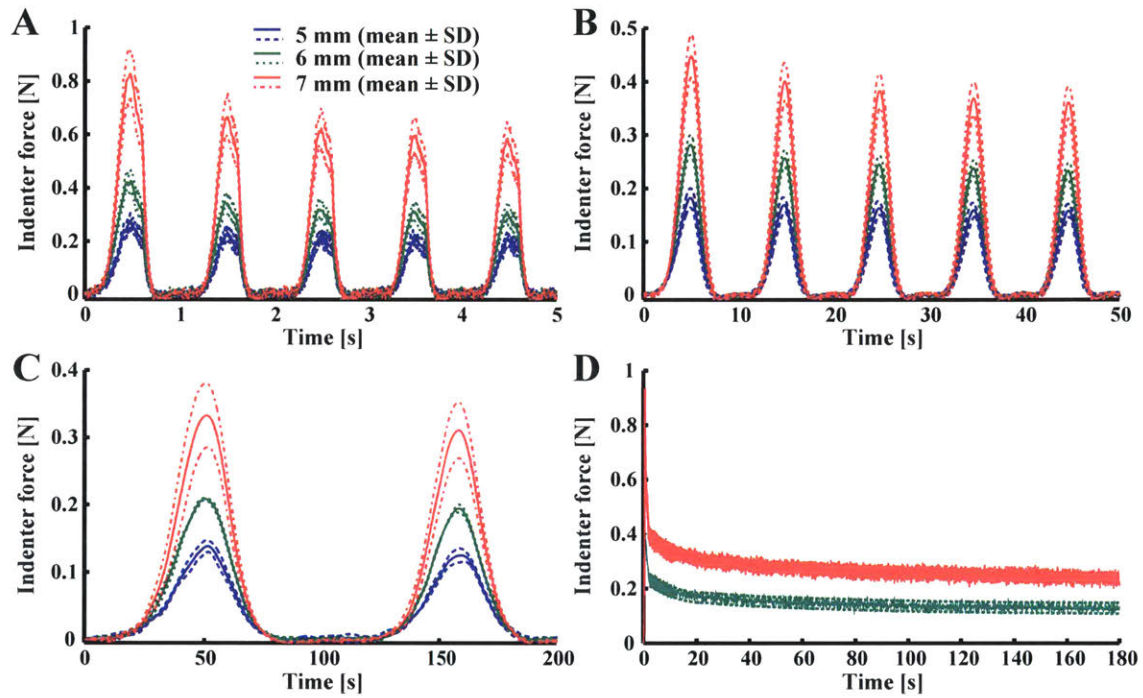


Figure D-2: Average indenter force response in load-unload (A, B, C) and in relaxation (D) at maximum penetration depths of 5 mm, 6 mm and 7 mm. Dashed lines correspond to average plus or minus standard deviation. The number of independent measurements for each load-unload case at sinusoidal frequencies of 1 Hz (A), 0.1 Hz (B) and 0.01 Hz (C) is provided in Figure D-3D. The numbers of independent measurements performed in relaxation were 3 (at 6 mm depth) and 1 (at 7 mm depth).

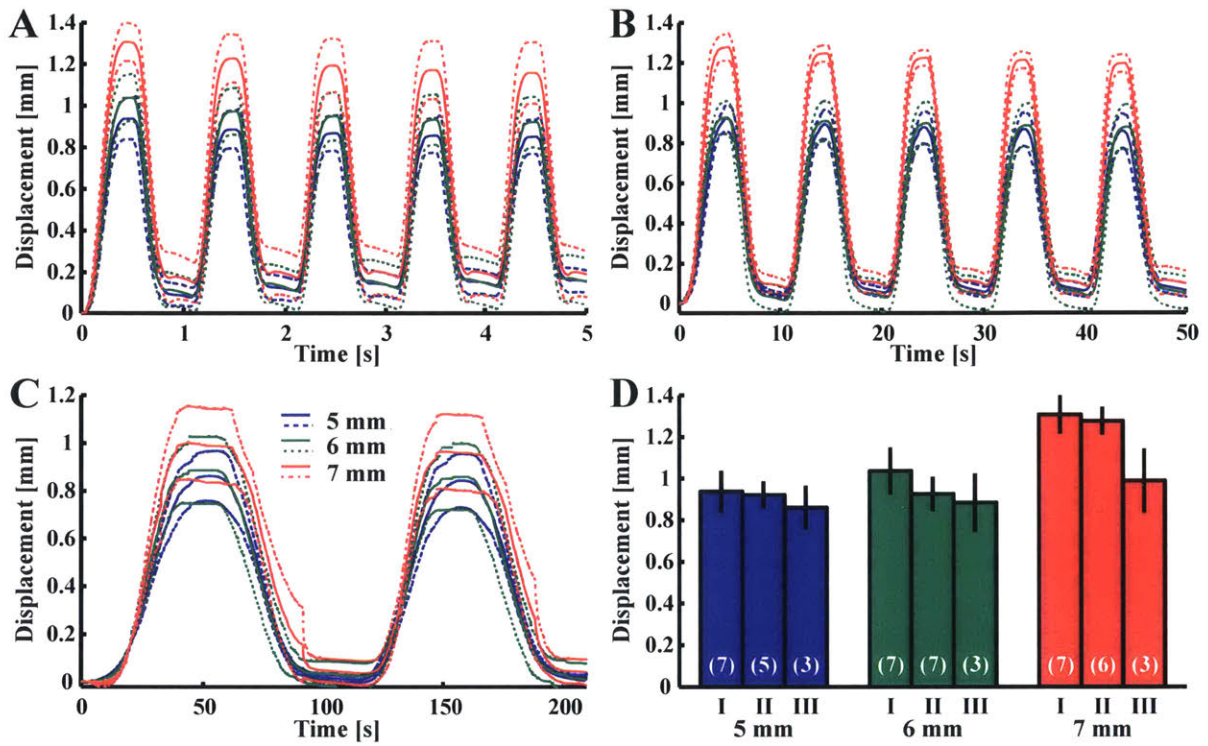


Figure D-3: Average secondary sensor displacement (upward vertical direction) for cyclic load-unload indentation tests to 5, 6 and 7 mm depths at 1 Hz (A), 0.1 Hz (B) and 0.01 Hz (C). Secondary sensor displacements measured at the end of the first loading ramp at 1 Hz (I), 0.1 Hz (II) and 0.01 Hz (III) are shown in panel D. Numbers in parentheses correspond to numbers of independent measurements obtained in each case. Each measurement corresponds to the average displacement response obtained from the three sensors.

Bibliography

- [1] Estes, M.S. and J.H. McElhaney, Response of Brain Tissue of Compressive Loading. *Mechanical Engineering: the journal of the American Society of Mechanical Engineers*, 1970. 92(11): p. 58-61.
- [2] Pamidi, M.R. and S.H. Advani, Nonlinear constitutive relations for human brain tissue. *Journal of Biomechanical Engineering - Transactions of the Asme*, 1978. 100(1): p. 44-48.
- [3] Mendis, K.K., R.L. Stalnaker, and S.H. Advani, A constitutive relationship for large deformation finite element modeling of brain tissue. *Journal of Biomechanical Engineering - Transactions of the Asme*, 1995. 117(3): p. 279-285.
- [4] Miller, K., Constitutive model of brain tissue suitable for finite element analysis of surgical procedures. *Journal of Biomechanics*, 1999. 32(5): p. 531-537.
- [5] Takhounts, E.G., J.R. Crandall, and K. Darvish, On the Importance of Nonlinearity of Brain Tissue Under Large Deformations. *Stapp Car Crash Journal*, 2003. 47: p. 79-92.
- [6] Cheng, S. and L.E. Bilston, Unconfined compression of white matter. *Journal of Biomechanics*, 2007. 40(1): p. 117-124.
- [7] Pervin, F. and W.W. Chen, Dynamic mechanical response of bovine gray matter and white matter brain tissues under compression. *Journal of Biomechanics*, 2009. 42(6): p. 731-735.

- [8] Zhang, L.Y., K.H. Yang, and A.I. King, Comparison of brain responses between frontal and lateral impacts by finite element modeling. *Journal of Neurotrauma*, 2001. 18(1): p. 21-30.
- [9] Zhang, L., et al., Computational Study of the Contribution of the Vasculature on the Dynamic Response of the Brain. *Stapp Car Crash Journal*, 2002. 46: p. 145-163.
- [10] El Sayed, T., et al., Biomechanics of traumatic brain injury. *Computer Methods in Applied Mechanics and Engineering*, 2008. 197(51-52): p. 4692-4701.
- [11] Brands, D.W.A., P.H.M. Bovendeerd, and J.S.H.M. Wismans, On the Potential Importance of Non-Linear Viscoelastic Material Modelling for Numerical Prediction of Brain Tissue Response: Test and Application. *Stapp Car Crash Journal*, 2002. 46: p. 103-121.
- [12] Zhang, L.Y., K.H. Yang, and A.I. King, A proposed injury threshold for mild traumatic brain injury. *Journal of Biomechanical Engineering - Transactions of the Asme*, 2004. 126(2): p. 226-236.
- [13] Gefen, A., et al., Age-dependent changes in material properties of the brain and braincase of the rat. *Journal of Neurotrauma*, 2003. 20(11): p. 1163-1177.
- [14] Arbogast, K.B. and S.S. Margulies, Material characterization of the brainstem from oscillatory shear tests. *Journal of Biomechanics*, 1998. 31(9): p. 801-807.
- [15] Prange, M.T. and S.S. Margulies, Regional, directional, and age-dependent properties of the brain undergoing large deformation. *Journal of Biomechanical Engineering - Transactions of the Asme*, 2002. 124(2): p. 244-252.
- [16] Velardi, F., F. Fraternali, and M. Angelillo, Anisotropic constitutive equations and experimental tensile behavior of brain tissue. *Biomechanics and Modeling in Mechanobiology*, 2006. 5(1): p. 53-61.

- [17] Metz, H., J. McElhaney, and A.K. Ommaya, A Comparison of the Elasticity of Live, Dead, and Fixed Brain Tissue. *Journal of Biomechanics*, 1970. 3(4): p. 453-458.
- [18] Walsh, E.K., W.W. Furniss, and A. Schettini, On measurement of brain elastic response in vivo. *American Journal of Physiology - Regulatory, Integrative and Comparative Physiology*, 1977. 232(1): p. 27-30.
- [19] Miller, K., et al., Mechanical properties of brain tissue in-vivo: experiment and computer simulation. *Journal of Biomechanics*, 2000. 33(11): p. 1369-1376.
- [20] Gefen, A. and S.S. Margulies, Are in vivo and in situ brain tissues mechanically similar? *Journal of Biomechanics*, 2004. 37(9): p. 1339-1352.
- [21] Atay, S.M., et al., Measurement of the dynamic shear modulus of mouse brain tissue in vivo by magnetic resonance elastography. *Journal of Biomechanical Engineering - Transactions of the Asme*, 2008. 130(2): p. 021013.
- [22] Franceschini, G., et al., Brain tissue deforms similarly to filled elastomers and follows consolidation theory. *Journal of the Mechanics and Physics of Solids*, 2006. 54(12): p. 2592-2620.
- [23] Hrapko, M., et al., The mechanical behaviour of brain tissue: Large strain response and constitutive modelling. *Biorheology*, 2006. 43(5): p. 623-636.
- [24] El Sayed, T., et al., A variational constitutive model for soft biological tissues. *Journal of Biomechanics*, 2008. 41(7): p. 1458-1466.
- [25] Moore, D.F., et al., Computational biology - Modeling of primary blast effects on the central nervous system. *Neuroimage*, 2009. 47: p. T10-T20.
- [26] Balakrishnan, A. and S. Socrate, Material property differentiation in indentation testing using secondary sensors. *Experimental Mechanics*, 2008. 48(4): p. 549-558.

- [27] Fallenstein, G.T., V.D. Hulce, and J.W. Melvin, Dynamic mechanical properties of human brain tissue. *Journal of Biomechanics*, 1969. 2(3): p. 217-226.
- [28] Shuck, L.Z. and S.H. Advani, Rheological Response of Human Brain Tissue in Shear. *Journal of Basic Engineering*, 1972. 94(4): p. 905-911.
- [29] Bilston, L.E., Z.Z. Liu, and N. Phan-Thien, Linear viscoelastic properties of bovine brain tissue in shear. *Biorheology*, 1997. 34(6): p. 377-385.
- [30] Nicolle, S., et al., Shear linear behavior of brain tissue over a large frequency range. *Biorheology*, 2005. 42(3): p. 209-223.
- [31] Thibault, K.L. and S.S. Margulies, Age-dependent material properties of the porcine cerebrum: effect on pediatric inertial head injury criteria. *Journal of Biomechanics*, 1998. 31(12): p. 1119-1126.
- [32] Peters, G.W.M., J.H. Meulman, and A. Sauren, The applicability of the time/temperature superposition principle to brain tissue. *Biorheology*, 1997. 34(2): p. 127-138.
- [33] Nicolle, S., M. Lounis, and R. Willinger, Shear Properties of Brain Tissue over a Frequency Range Relevant for Automotive Impact Situations: New Experimental Results. *Stapp Car Crash Journal*, 2004. 48: p. 239-258.
- [34] Miller, K. and K. Chinzei, Constitutive modelling of brain tissue: experiment and theory. *Journal of biomechanics*, 1997. 30(11-12): p. 1115-1121.
- [35] Tamura, A., et al., Mechanical Characterization of Brain Tissue in High-Rate Compression. *Journal of Biomechanical Science and Engineering*, 2007. 2(3): p. 115-126.
- [36] Miller, K. and K. Chinzei, Mechanical properties of brain tissue in tension. *Journal of Biomechanics*, 2002. 35(4): p. 483-490.

- [37] Darvish, K.K. and J.R. Crandall, Nonlinear viscoelastic effects in oscillatory shear deformation of brain tissue. *Medical Engineering & Physics*, 2001. 23(9): p. 633-645.
- [38] McElhaney, J.H., et al. Dynamic characteristics of the tissues of the head. in *Perspectives in Biomedical Engineering*. 1973. London: The MacMillan Press LTD.
- [39] Guillaume, A., et al., Effects of perfusion on the mechanical behavior of the brain exposed to hypergravity. *Journal of Biomechanics*, 1997. 30(4): p. 383-389.
- [40] Ruan, J.S., T. Khalil, and A.I. King, Dynamic Response of the Human Head to Impact by Three-Dimensional Finite Element Analysis. *Journal of Biomechanical Engineering - Transactions of the Asme*, 1994. 116(1): p. 44-50.
- [41] Bilston, L.E., Z.Z. Liu, and N. Phan-Thien, Large strain behaviour of brain tissue in shear: Some experimental data and differential constitutive model. *Biorheology*, 2001. 38(4): p. 335-345.
- [42] Dickerson, J.W.T. and J. Dobbing, Prenatal and postnatal growth and development of the central nervous system of the pig. *Proceedings of the Royal Society of London Series B-Biological Sciences*, 1967. 166(1005): p. 384-395.
- [43] Pampiglione, G., Some aspects of development of cerebral function in mammals. *Proceedings of the Royal Society of Medicine-London*, 1971. 64(4): p. 429-435.
- [44] Flynn, T.J., Developmental changes of myelin-related lipids in brain of miniature swine. *Neurochemical Research*, 1984. 9(7): p. 935-945.
- [45] Duhaime, A.C., et al., Maturation-dependent response of the piglet brain to scaled cortical impact. *Journal of Neurosurgery*, 2000. 93(3): p. 455-462.
- [46] Fang, M.R., et al., Myelination of the pig's brain: A correlated MRI and histological study. *Neurosignals*, 2005. 14(3): p. 102-108.

- [47] Coats, B. and S.S. Margulies, Material properties of porcine parietal cortex. *Journal of Biomechanics*, 2006. 39(13): p. 2521-2525.
- [48] Balakrishnan, A., Development of novel dynamic indentation techniques for soft tissue applications. PhD thesis, Massachusetts Institute of Technology, Cambridge, MA; 2007.
- [49] Biot, M.A., General theory of three-dimensional consolidation. *Journal of Applied Physics*, 1941. 12(2): p. 155-164.
- [50] Nicholson, C., Diffusion and related transport mechanisms in brain tissue. *Reports on Progress in Physics*, 2001. 64(7): p. 815-884.
- [51] Basser, P.J., Interstitial Pressure, Volume, and Flow during Infusion into Brain Tissue. *Microvascular Research*, 1992. 44(2): p. 143-165.
- [52] Galford, J.E. and J.H. McElhaney, A Viscoelastic Study of Scalp, Brain, and Dura. *Journal of Biomechanics*, 1970. 3(2): p. 211-221.
- [53] Donnelly, B.R. and J. Medige, Shear properties of human brain tissue. *Journal of Biomechanical Engineering - Transactions of the Asme*, 1997. 119(4): p. 423-432.
- [54] Kleiven, S. and W.N. Hardy, Correlation of an FE Model of the Human Head with Local Brain Motion - Consequences for Injury Prediction. *Stapp Car Crash Journal*, 2002. 46: p. 123-144.
- [55] Brands, D.W.A., G.W.M. Peters, and P.H.M. Bovendeerd, Design and numerical implementation of a 3-D non-linear viscoelastic constitutive model for brain tissue during impact. *Journal of Biomechanics*, 2004. 37(1): p. 127-134.
- [56] Kohandel, M., et al., The constitutive properties of the brain parenchyma Part 1. Strain energy approach. *Medical Engineering & Physics*, 2006. 28(5): p. 449-454.

- [57] Lee, E.H., Elastic-plastic deformation at finite strains. *Journal of Applied Mechanics*, 1969. 36(1): p. 1-6.
- [58] Lodish, H., et al., *Molecular Cell Biology*. Sixth Edition ed, ed. K. Ahr. 2007, New York: W. H. Freeman and Company.
- [59] Arruda, E.M. and M.C. Boyce, A three-dimensional constitutive model for the large stretch behavior of rubber elastic materials. *Journal of the Mechanics and Physics of Solids*, 1993. 41(2): p. 389-412.
- [60] Gardel, M.L., et al., Prestressed F-actin networks cross-linked by hinged filamins replicate mechanical properties of cells. *Proceedings of the National Academy of Sciences of the United States of America*, 2006. 103(6): p. 1762-1767.
- [61] Bernick, K., et al. Mechanical Response of Rat Cortical Neurons: AFM Indentations and Preliminary Modeling. In: *Proceedings of the ASME Summer Bioengineering Conference*, 2009. Lake Tahoe, CA.
- [62] Holzapfel, G., A, *Nonlinear solid mechanics: a continuum approach for engineering*. 2000, West Sussex, England: John Wiley & Sons Ltd.
- [63] Boyce, M.C., G.G. Weber, and D.M. Parks, On the kinematics of finite strain plasticity. *Journal of the Mechanics and Physics of Solids*, 1989. 37(5): p. 647-665.
- [64] Bergstrom, J.S. and M.C. Boyce, Constitutive modeling of the time-dependent and cyclic loading of elastomers and application to soft biological tissues. *Mechanics of Materials*, 2001. 33(9): p. 523-530.
- [65] Anand, L., On H. Hencky's Approximate Strain-Energy Function for Moderate Deformations. *Journal of Applied Mechanics - Transactions of the Asme*, 1979. 46(1): p. 78-82.
- [66] Criscione, J.C., Direct tensor expression for natural strain and fast, accurate approximation. *Computers & Structures*, 2002. 80(25): p. 1895-1905.

- [67] Lagarias, J.C., et al., Convergence properties of the Nelder-Mead simplex method in low dimensions. *Siam Journal on Optimization*, 1998. 9(1): p. 112-147.
- [68] Jordan, P., et al., Constitutive modeling of porcine liver in indentation using 3D ultrasound imaging. *Journal of the Mechanical Behavior of Biomedical Materials*, 2009. 2(2): p. 192-201.
- [69] Chui, C., et al., Transversely isotropic properties of porcine liver tissue: experiments and constitutive modelling. *Medical & Biological Engineering & Computing*, 2007. 45(1): p. 99-106.
- [70] Shreiber, D.I., H.L. Hao, and R.A.I. Elias, Probing the influence of myelin and glia on the tensile properties of the spinal cord. *Biomechanics and Modeling in Mechanobiology*, 2009. 8(4): p. 311-321.
- [71] Mulliken, A.D. and M.C. Boyce, Mechanics of the rate-dependent elastic-plastic deformation of glassy polymers from low to high strain rates. *International Journal of Solids and Structures*, 2006. 43(5): p. 1331-1356.
- [72] Saraf, H., et al., Mechanical properties of soft human tissues under dynamic loading. *Journal of Biomechanics*, 2007. 40(9): p. 1960-1967.
- [73] Corrigan, J.D., A.W. Selassie, and J.A.L. Orman, The epidemiology of traumatic brain injury. *J Head Trauma Rehabil*, 2010. 25(2): p. 72-80.
- [74] Belanger, H.G., et al., Cognitive sequelae of blast-related versus other mechanisms of brain trauma. *Journal of the International Neuropsychological Society*, 2009. 15(1): p. 1-8.
- [75] Crowe, L.M., et al., Head injuries related to sports and recreation activities in school-age children and adolescents: Data from a referral centre in Victoria, Australia. *Emergency Medicine Australasia*, 2010. 22(1): p. 56-61.

- [76] McCrory, P., et al., Value of neuropsychological testing after head injuries in football. *British Journal of Sports Medicine*, 2005. 39: p. I58-I63.
- [77] Hoge, C.W., H.M. Goldberg, and C.A. Castro, Care of War Veterans with Mild Traumatic Brain Injury - Flawed Perspectives. *New England Journal of Medicine*, 2009. 360(16): p. 1588-1591.
- [78] Kraus, J.F. and D.L. McArthur, Epidemiologic aspects of brain injury. *Neurologic Clinics*, 1996. 14(2): p. 435-450.
- [79] Hrapko, M., et al., Characterisation of the mechanical behaviour of brain tissue in compression and shear. *Biorheology*, 2008. 45(6): p. 663-676.
- [80] Prevost, T.P., et al., Biomechanics of brain tissue. *Acta Biomaterialia*, 2010: to appear.
- [81] Tamura, A., et al., Mechanical Characterization of Brain Tissue in High-Rate Extension. *Journal of Biomechanical Science and Engineering*, 2008. 3(2): p. 263-274.
- [82] Muthupillai, R., et al., Magnetic resonance imaging of transverse acoustic strain waves. *Science*, 1995. 269(5232): p. 1854-1857.
- [83] McCracken, P.J., et al., Mechanical transient-based magnetic resonance elastography. *Magnetic Resonance in Medicine*, 2005. 53(3): p. 628-639.
- [84] Hamhaber, U., et al., Three-dimensional analysis of shear wave propagation observed by in vivo magnetic resonance elastography of the brain. *Acta Biomaterialia*, 2007. 3(1): p. 127-137.
- [85] Xu, L., et al., Magnetic resonance elastography of brain tumors: Preliminary results. *Acta Radiologica*, 2007. 48(3): p. 327-330.
- [86] Green, M.A., L.E. Bilston, and R. Sinkus, In vivo brain viscoelastic properties measured by magnetic resonance elastography. *Nmr in Biomedicine*, 2008. 21(7): p. 755-764.

- [87] Schiavone, P., et al., In vivo measurement of human brain elasticity using a light aspiration device. *Med Image Anal*, 2009. 13(4): p. 673-8.
- [88] Schettini, A. and E.K. Walsh, Brain tissue elastic behavior and experimental brain compression. *American Journal of Physiology - Regulatory, Integrative and Comparative Physiology*, 1988. 255(5): p. 799-805.
- [89] Miga, M.I., et al., In vivo modeling of interstitial pressure in the brain under surgical load using finite elements. *Journal of Biomechanical Engineering - Transactions of the Asme*, 2000. 122(4): p. 354-363.
- [90] Lai-Fook, S.J., et al., Elastic constants of inflated lobes of dog lungs. *Journal of Applied Physiology*, 1976. 40(4): p. 508-513.
- [91] Vannah, W.M. and D.S. Childress, Indentor tests and finite element modeling of bulk muscular tissue in vivo. *Journal of Rehabilitation Research and Development*, 1996. 33(3): p. 239-252.
- [92] Gefen, A., et al., Integration of plantar soft tissue stiffness measurements in routine MRI of the diabetic foot. *Clinical Biomechanics*, 2001. 16(10): p. 921-925.
- [93] Li, L.P. and W. Herzog, Arthroscopic evaluation of cartilage degeneration using indentation testing - Influence of indenter geometry. *Clinical Biomechanics*, 2006. 21(4): p. 420-426.
- [94] Kerdok, A.E., M.P. Ottensmeyer, and R.D. Howe, Effects of perfusion on the viscoelastic characteristics of liver. *Journal of Biomechanics*, 2006. 39(12): p. 2221-2231.
- [95] van Dommelen, J.A.W., et al., Mechanical properties of brain tissue by indentation: Interregional variation. *Journal of the Mechanical Behavior of Biomedical Materials*, 2010. 3(2): p. 158-166.

- [96] Manley, G.T., et al., Controlled cortical impact in swine: Pathophysiology and biomechanics. *Journal of Neurotrauma*, 2006. 23(2): p. 128-139.
- [97] McGarvey, K.A., J.M. Lee, and D.R. Boughner, Mechanical suitability of glycerol-preserved human dura mater for construction of prosthetic cardiac valves. *Biomaterials*, 1984. 5(2): p. 109-117.
- [98] Runza, M., et al., Lumbar dura mater biomechanics: Experimental characterization and scanning electron microscopy observations. *Anesthesia and Analgesia*, 1999. 88(6): p. 1317-1321.
- [99] Maikos, J.T., R.A.I. Elias, and D.I. Shreiber, Mechanical properties of dura mater from the rat brain and spinal cord. *Journal of Neurotrauma*, 2008. 25(1): p. 38-51.
- [100] Garo, A., et al., Towards a reliable characterisation of the mechanical behaviour of brain tissue: The effects of post-mortem time and sample preparation. *Biorheology*, 2007. 44(1): p. 51-58.
- [101] Tanielian, T. and L.H. Jaycox, *Invisible Wounds of War: Psychological and Cognitive Injuries, Their Consequences, and Services to Assist Recovery*, ed. T. Tanielian and L.H. Jaycox. 2008, Santa Monica, CA: RAND Corporation.
- [102] Vanderploeg, R.D., et al., Long-term morbidities following self-reported mild traumatic brain injury. *Journal of Clinical and Experimental Neuropsychology*, 2007. 29(6): p. 585-598.
- [103] Meehan, W.P. and R.G. Bachur, Sport-Related Concussion. *Pediatrics*, 2009. 123(1): p. 114-123.
- [104] Yilmaz, S. and M. Pekdemir, An unusual primary blast injury - Traumatic brain injury due to primary blast injury. *American Journal of Emergency Medicine*, 2007. 25(1): p. 97-98.

- [105] Taber, K.H., D.L. Warden, and R.A. Hurley, Blast-Related Traumatic Brain Injury: What Is Known? *J Neuropsychiatry Clin Neurosci*, 2006. 18(2): p. 141-145.
- [106] Lew, H.L., et al., Soldiers with occult traumatic brain injury. *American Journal of Physical Medicine & Rehabilitation*, 2005. 84(6): p. 393-398.
- [107] Bao, G. and S. Suresh, Cell and molecular mechanics of biological materials. *Nature Materials*, 2003. 2(11): p. 715-725.
- [108] Van Vliet, K., G. Bao, and S. Suresh, The biomechanics toolbox: experimental approaches for living cells and biomolecules. *Acta Materialia*, 2003. 51(19): p. 5881-5905.
- [109] Suresh, S., Biomechanics and biophysics of cancer cells. *Acta Materialia*, 2007. 55(12): p. 3989-4014.
- [110] Wang, N., J.P. Butler, and D.E. Ingber, Mechanotransduction across the cell surface and through the cytoskeleton. *Science*, 1993. 260(5111): p. 1124-1127.
- [111] Trepatt, X., et al., Viscoelasticity of human alveolar epithelial cells subjected to stretch. *American Journal of Physiology-Lung Cellular and Molecular Physiology*, 2004. 287: p. L1025-L1034.
- [112] Tagawa, H., et al., Cytoskeletal mechanics in pressure-overload cardiac hypertrophy. *Circulation Research*, 1997. 80(2): p. 281-289.
- [113] Massiera, G., et al., Mechanics of single cells: Rheology, time dependence, and fluctuations. *Biophysical Journal*, 2007. 93: p. 3703-3713.
- [114] Mahaffy, R.E., et al., Quantitative analysis of the viscoelastic properties of thin regions of fibroblasts using atomic force microscopy. *Biophysical Journal*, 2004. 86(3): p. 1777-1793.

- [115] Darling, E.M., S. Zauscher, and F. Guilak, Viscoelastic properties of zonal articular chondrocytes measured by atomic force microscopy. *Osteoarthritis and Cartilage*, 2006. 14(6): p. 571-579.
- [116] Lulevich, V., et al., Cell Mechanics Using Atomic Force Microscopy-Based Single-Cell Compression. *Langmuir*, 2006. 22(19): p. 8151-8155.
- [117] Radmacher, M., et al., Measuring the viscoelastic properties of human platelets with the atomic force microscope. *Biophysical Journal*, 1996. 70(1): p. 556-567.
- [118] Mathur, A.B., et al., Endothelial, cardiac muscle and skeletal muscle exhibit different viscous and elastic properties as determined by atomic force microscopy. *Journal of Biomechanics*, 2001. 34(12): p. 1545-1553.
- [119] Lam, W., M. Rosenbluth, and D. Fletcher, Chemotherapy exposure increases leukemia cell stiffness. *Blood*, 2007. 109(8): p. 3505.
- [120] Evans, E. and B. Kukan, Passive material behavior of granulocytes based on large deformation and recovery after deformation tests. *Blood*, 1984. 64(5): p. 1028-1035.
- [121] Merryman, W.D., et al., Correlation between heart valve interstitial cell stiffness and transvalvular pressure: implications for collagen biosynthesis. *American Journal of Physiology-Heart and Circulatory Physiology*, 2006. 290(1): p. H224-H231.
- [122] Rand, R.P. and A.C. Burton, Mechanical properties of red cell membrane. I. Membrane stiffness + intracellular pressure. *Biophysical Journal*, 1964. 4(2): p. 115-135.
- [123] Schmidschonbein, G.W., et al., Passive mechanical properties of human leukocytes. *Biophysical Journal*, 1981. 36(1): p. 243-256.
- [124] Sato, M., et al., Application of the micropipete technique to the measurement of cultured porcine aortic endothelial cell viscoelastic properties. *Journal of Biomechanical Engineering - Transactions of the Asme*, 1990. 112(3): p. 263-268.

- [125] Trickey, W.R., T.P. Vail, and F. Guilak, The role of the cytoskeleton in the viscoelastic properties of human articular chondrocytes. *Journal of Orthopaedic Research*, 2004. 22(1): p. 131-139.
- [126] Henon, S., et al., A new determination of the shear modulus of the human erythrocyte membrane using optical tweezers. *Biophysical Journal*, 1999. 76(2): p. 1145-1151.
- [127] Mills, J.P., et al., Effect of plasmodial RESA protein on deformability of human red blood cells harboring *Plasmodium falciparum*. *Proceedings of the National Academy of Sciences of the United States of America*, 2007. 104(22): p. 9213-9217.
- [128] Guck, J., et al., The optical stretcher: A novel laser tool to micromanipulate cells. *Biophysical Journal*, 2001. 81(2): p. 767-784.
- [129] Lu, Y.B., et al., Viscoelastic properties of individual glial cells and neurons in the CNS. *Proceedings of the National Academy of Sciences of the United States of America*, 2006. 103(47): p. 17759-17764.
- [130] Desprat, N., et al., Creep function of a single living cell. *Biophysical Journal*, 2005. 88: p. 2224-2233.
- [131] Fernandez, P., P.A. Pullarkat, and A. Ott, A master relation defines the nonlinear viscoelasticity of single fibroblasts. *Biophysical Journal*, 2006. 90(10): p. 3796-3805.
- [132] Suresh, S., et al., Connections between single-cell biomechanics and human disease states: gastrointestinal cancer and malaria. *Acta Biomaterialia*, 2005. 1(1): p. 15-30.
- [133] Binnig, G., C.F. Quate, and C. Gerber, Atomic force microscope. *Phys Rev Lett*, 1986. 56(9): p. 930-933.

- [134] Franz, C.M. and P.H. Puech, Atomic Force Microscopy: A Versatile Tool for Studying Cell Morphology, Adhesion and Mechanics. *Cellular and Molecular Bioengineering*, 2008. 1(4): p. 289-300.
- [135] Li, Q.S., et al., AFM indentation study of breast cancer cells. *Biochemical and Biophysical Research Communications*, 2008. 374(4): p. 609-613.
- [136] Spagnoli, C., et al., Drift-free atomic force microscopy measurements of cell height and mechanical properties. *Review of Scientific Instruments*, 2007. 78(3).
- [137] Radmacher, M., Studying the mechanics of cellular processes by atomic force microscopy. *Cell Mechanics*, 2007. 83: p. 347-372.
- [138] Costa, K.D., A.J. Sim, and F.C.P. Yin, Non-Hertzian approach to analyzing mechanical properties of endothelial cells probed by atomic force microscopy. *Journal of Biomechanical Engineering - Transactions of the Asme*, 2006. 128(2): p. 176-184.
- [139] Karcher, H., et al., A three-dimensional viscoelastic model for cell deformation with experimental verification. *Biophysical Journal*, 2003. 85(5): p. 3336-3349.
- [140] Unnikrishnan, G.U., V.U. Unnikirishnan, and J.N. Reddy, Constitutive material modeling of cell: a micromechanics approach. *Journal of Biomechanical Engineering - Transactions of the Asme*, 2007. 129(3): p. 315-323.
- [141] Shin, D. and K. Athanasiou, Cytoindentation for obtaining cell biomechanical properties. *Journal of Orthopaedic Research*, 1999. 17(6): p. 880-890.
- [142] Guilak, F. and V.C. Mow, The mechanical environment of the chondrocyte: a biphasic finite element model of cell-matrix interactions in articular cartilage. *Journal of Biomechanics*, 2000. 33(12): p. 1663-1673.
- [143] McGarry, J.G. and P.J. Prendergast, A three-dimensional finite element model of an adherent eukaryotic cell. *Eur Cell Mater*, 2004. 7: p. 27-33; discussion 33-4.

- [144] Brewer, G. and J. Torricelli, Isolation and culture of adult neurons and neurospheres. *Nat Protoc*, 2007. 2(6): p. 1490-1498.
- [145] Matei, G.A., et al., Precision and accuracy of thermal calibration of atomic force microscopy cantilevers. *Review of Scientific Instruments*, 2006. 77.
- [146] Rudoy, D., et al., Bayesian changepoint analysis with application to atomic force microscopy and soft material indentation. *Journal of the Royal Statistical Society Series C*, 2010: to appear.
- [147] Guilak, F., J.R. Tedrow, and R. Burgkart, Viscoelastic Properties of the Cell Nucleus. *Biochemical and Biophysical Research Communications*, 2000. 269(3): p. 781-786.
- [148] Maniotis, A., C. Chen, and D. Ingber, Demonstration of mechanical connections between integrins, cytoskeletal filaments, and nucleoplasm that stabilize nuclear structure. *Proceedings of the National academy of Sciences of the United States of America*, 1997. 94(3): p. 849.
- [149] Elkin, B., et al., Mechanical Heterogeneity of the Rat Hippocampus Measured by Atomic Force Microscope Indentation. *Journal of Neurotrauma*, 2007. 24(5): p. 812-822.